Metal mobility during hydrothermal breakdown of Fe-Ti oxides: insights from Sb-Au mineralizing event (Variscan Armorican Massif, France)

Anthony Pochon, Georges Beaudoin, Yannick Branquet, Philippe Boulvais, Eric Gloaguen, Denis Gapais

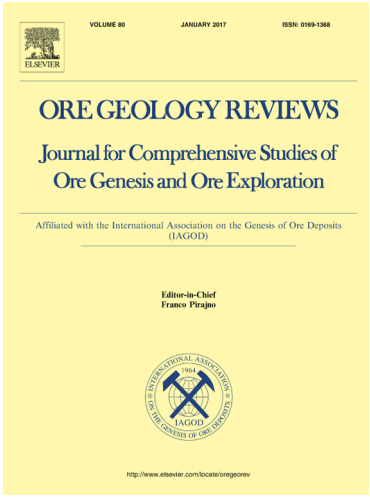

Metal mobility during hydrothermal breakdown of Fe-Ti oxides: insights from Sb-Au mineralizing event (Variscan Armorican Massif, France)

Anthony Pochon, Georges Beaudoin, Yannick Branquet, Philippe Boulvais, Eric Gloaguen, Denis Gapais

PII: S0169-1368(17)30527-9
DOI: https://doi.org/10.1016/j.oregeorev.2017.10.021
Reference: OREGEO 2380

To appear in: *Ore Geology Reviews*

Received Date: 7 July 2017
Revised Date: 19 October 2017
Accepted Date: 23 October 2017

Please cite this article as: A. Pochon, G. Beaudoin, Y. Branquet, P. Boulvais, E. Gloaguen, D. Gapais, Metal mobility during hydrothermal breakdown of Fe-Ti oxides: insights from Sb-Au mineralizing event (Variscan Armorican Massif, France), *Ore Geology Reviews* (2017), doi: https://doi.org/10.1016/j.oregeorev.2017.10.021

Metal mobility during hydrothermal breakdown of Fe-Ti oxides: insights from Sb-Au mineralizing event (Variscan Armorican Massif, France)

Anthony Pochon[1*], Georges Beaudoin[2], Yannick Branquet[1, 3], Philippe Boulvais[1], Eric Gloaguen[3, 4], Denis Gapais[1]

[1] Géosciences Rennes, UMR 6118, Université de Rennes 1, OSUR, Campus de Beaulieu, 35042 Rennes Cedex, France

[2] Département de géologie et de génie géologique, Université Laval, Québec (QC) G1V 0A6, Canada

[3] Institut des Sciences de la Terre d'Orléans, UMR 7327, Université d'Orléans, Campus Géosciences, 1A rue de la Férollerie, 45071 Orléans Cedex 2, France

[4] Bureau de Recherche Géologique et Minière (BRGM), UMR 7327, 3 avenue Claude-Guillemin, BP 36009, 45060 Orléans Cedex 02, France

* Corresponding author: pochon.anthony@gmail.com; +33(6)28200871

Abstract

Hydrothermal alteration related to Sb-Au mineralization is widespread in the Variscan Armorican Massif, but mineral replacement reactions are not well characterized, in particular the hydrothermal breakdown of ilmenite-titanohematite. Based on petrography, electron probe micro-analyzer and laser ablation-inductively coupled plasma-mass spectrometer analyses, we document mineralogical change at rock- and mineral-scale and the redistribution of Sb and others trace elements during the recrystallization of ilmenite-titanohematite to hydrothermal rutile. Hydrothermal alteration is mainly potassic with associated carbonation. The replacement mechanism is interpreted to be an interface-coupled dissolution-reprecipitation process. Results show that Mn, Zn, Co, Ni, Sn, Mo and U are released during hydrothermal alteration, whereas Sb and W are incorporated in newly-formed hydrothermal rutile from the hydrothermal fluid. Furthermore, the concentration of Sb evolves through time suggesting a change in fluid composition likely related to an enrichment of fluid in Sb during rutile crystallization. Considering that Fe-Ti oxides breakdown during hydrothermal alteration is common within epithermal and mesothermal/orogenic Au-Sb mineralizing systems, results report in this study yield important constraints about metal mobility and exchanges in hydrothermal gold systems.

Keywords: ilmenite-titanohematite hydrothermal breakdown; Sb mineralization; EPMA; LA-ICP-MS; redistribution of trace elements; hydrothermal alteration; rutile

1. Introduction

Understanding trace element behavior and redistribution processes is a fundamental step with respect to large-scale transport of heat and chemical elements in the crust. Consequently, it is a critical process in the formation of various types of mineral deposits. Fluid-assisted mineral replacement reactions can release chemical elements into the fluid, or incorporate some elements in the fluid into the newly-formed phase, such that it is possible to trace some specific mineral reactions from which metals are released from crustal rocks (Zack and John, 2007; Putnis and Fernandez-Diaz, 2010; Pitcairn et al., 2014, 2015; Cave et al., 2015). For example, rutile is used as an indicator of deposit types (Meinhold, 2010). One reason for this is that rutile is common in many rock types, especially those that have undergone metasomatic alteration (Williams and Cesbron, 1977). Rutile incorporates significant amount of trace elements into its lattice, such as high field strength elements (HFSE), Al, V, Cr, Fe, Sn, U, Sb and W (Smith and Perseil, 1997; Rice et al., 1998; Zack et al., 2002, 2004; Bromiley and Hilairet, 2005; Scott, 2005; Carruzzo et al., 2006; Scott and Radford, 2007; Tomkins et al., 2007; Triebold et al., 2007; Meinhold 2010). Enrichments in Sb, W and V are commonly considered characteristic of rutile associated with orogenic gold deposits (Urban et al., 1992; Clark and Williams-Jones, 2004; Scott and Radford, 2007), whereas the incorporation of Cu and Mo in rutile is assumed to be characteristic of porphyry deposits (Scott, 2005; Rabbia et al., 2009). On the other hand, the breakdown of detrital rutile to titanite during prograde metamorphism (Otago Province, New Zealand) has been shown to release significant amounts of W (Cave et al., 2015), later incorporated in scheelite disseminated in Otago Schist and in orogenic gold veins (Cave et al., 2016). More generally, breakdown of Fe-Ti oxides is common during diagenetic, metamorphic and hydrothermal reactions (Morad and Aldahan, 1986; Luvizotto et al., 2009; Rabbia et al., 2009), a process that can redistribute metals at a regional scale.

The Variscan Armorican Massif (France) is a metallogenic province characterized by several types of mineral deposits (Chauris and Marcoux, 1994), including orogenic gold and antimony deposits. Fe-Ti oxide breakdown associated with Sb mineralization has been recognized at the Le Semnon Sb-Au deposit (Chauris et al., 1985; Gloaguen et al., 2016). In this paper, we present the textural, mineralogical and geochemical characteristics of the Fe-Ti oxide breakdown reaction, and discuss its implications in terms of metal mobility and potential metal source.

2. Geological framework

A significant part of French Sb-deposits are located in the Armorican Massif, in western France (Fig. 1), which belongs to the Ibero-Armorican Arc of the western European Variscan belt. The Armorican Massif is divided in several domains separated by two dextral crustal-scale shear zones, the North (NASZ) and South (SASZ) Armorican Shear Zones that were active during the Carboniferous (Gumiaux et al., 2004). The main Sb districts are located in the Central Armorican Domain (CAD) and in the South Armorican Domain (SAD). Antimony deposits (e.g., Le Semnon deposit in the CAD) are commonly associated with gold mineralization and spatially coexist with gold-sulfosalts deposits (e.g., Saint-Aubin-des-Châteaux deposit, Gloaguen et al., 2007). The CAD consists of Late Neoproterozoic to Late Paleozoic sedimentary rocks affected by low-grade regional metamorphism and moderate deformation. Deformation consists of upright folds with sub-vertical axial planes and E–W sub-horizontal axes produced by a N120-125-striking dextral wrenching of the CAD (Gapais and Le Corre, 1980; Gumiaux et al., 2004). Folding is associated with a sub-vertical cleavage (S1 on Fig. 1b) bearing a sub-horizontal stretching lineation. Several magmatic events occurred during the Variscan orogeny in the Armorican Massif, notably the emplacement of syntectonic granites (around 316-300 Ma) along the SASZ (Tartèse and Boulvais, 2010; Tartèse et al., 2011a, 2011b) or in association with crustal detachments (Gapais et al., 1993; Ballouard et al., 2015). In the eastern part of the CAD, the main magmatic event is characterized by a swarm of gabbro dykes and sills, locally called dolerite

(Lahaye et al., 1995; Aïfa et al., 1999; Le Gall, 1999). This gabbroic event has been dated by the U-Pb method with LA-ICP-MS on magmatic apatite at 363 ± 6 Ma (Pochon et al., 2016b).

The stibnite-gold quartz veins are generally considered to belong to a late Variscan hydrothermal event (Bouchot et al., 2005) that postdate Devonian hydrothermal fluid flow (Tartèse et al., 2015), although there is no geochronological data to support this hypothesis. Chauris and Marcoux (1994) suggest that the Sb-Au mineralization is sourced from various felsic magmatic events spanning the Cambrian-Carboniferous period, and deposited within Late Variscan shear zones. However, a strong spatial correlation between Sb (± Au) occurrences and relatively high density and magnetic zones has been demonstrated (Pochon et al., 2016a). These high density and magnetic zones are suggested to correspond to mafic/ultramafic bodies at depth, and are likely the parent magmatic intrusions of the numerous gabbroic dyke swarms outcropping in the area (Pochon et al., 2016a). These interpreted deep mafic/ultramafic bodies may represent an important source of metals for these mineralizing systems.

The Le Semnon Sb-Au district (Fig. 1) consists of a NW-SE striking, near vertical, gabbro dyke swarm intruded in the lower to middle Ordovician slates at ca. 363 Ma (Pochon et al., 2016b). These slates have been affected by regional deformation during the Variscan orogeny. The walls of the gabbro dykes are affected by a weak E-W trending, sub-vertical cleavage (Fig. 1b). Mineralization is spatially associated with gabbro dykes and consists of Sb- and Au-bearing quartz-carbonate flat veins (Fig. 1b). These mineralised veins crosscut the contact between the gabbro and the slate, and the regional cleavage. Some veins are folded and are affected by a weak regional cleavage. Mineralization consists of three main stages (Chauris et al., 1985): (1) an early Fe-As-(Au) stage consisting of arsenopyrite, pyrite and pyrrhotite, commonly replaced by pyrite and marcasite, (2) an intermediate Fe-Sb stage characterized by berthierite, and (3) a final Sb stage with massive stibnite and rare native antimony. Sphalerite and native gold occur with the Sb-mineralization, but their paragenetic position is unclear. Indeed, the sphalerite is in rare association with stibnite, whereas native gold is interpreted to be remobilized during the final stage (Chauris et al., 1985). The mineralization gangue is composed of quartz and carbonate (70 and 30 %, respectively). Arsenopyrite is rare inside the veins, but abundant disseminated in hydrothermally altered gabbro and slate wall rocks. Hydrothermal alteration is characterized by potassic metasomatism, highlighted by hydrothermal illite and sericitized plagioclase, accompanied by carbonation and a weak silicification. Within the altered gabbro dykes, the magmatic ilmenite is totally replaced by rutile, used in this paper in the general sense of "TiO_2-polymorph", and by an alteration product called leucoxene by Chauris et al. (1985).

3. Sampling

Five gabbro samples have been selected for characterizing the trace element geochemistry of Fe-Ti oxides: three unaltered gabbro samples were collected from the same dyke swarm (BAN1, TOU1, and MF1; Fig. 1) and two hydrothermally altered gabbro samples from the dyke hosting the Le Semnon deposit (SEM9 and SEM11). These five samples from four dykes are representative of the textural and compositional variety recognized in the area.

To investigate the geochemical variations and to quantify the metasomatic change of whole rock, we collected two additional samples of the hydrothermally altered gabbro from the Le Semnon mine to address primary magmatic heterogeneity. Both samples represent the core (SEM2) and the rim (SEM12) of the least and the more altered gabbro dyke, respectively. The sedimentary host rocks were not studied because of the difficulty establishing the protolith composition of the detrital host rocks.

The least altered gabbro dyke samples (BAN1, TOU1, and MF1) have a porphyritic and doleritic texture in which the principal mineral assemblage (Fig. 2a and b) consist of elongate plagioclase laths, clinopyroxene (mainly augite) and Fe-Ti oxides reaching up to 12 % in mineral proportion. The grain size of the Fe-Ti oxides ranges between 50 and 500 µm. Late stage crystallization is represented by rare interstitial quartz. The accessory minerals consist of apatite, rare primary biotite and titanite, pyrite, chalcopyrite, pyrrhotite, chlorite, green amphibole and epidote.

In contrast, the primary magmatic texture is not preserved in hydrothermally altered gabbro. The alteration variably affects gabbro along, and across, dykes. Plagioclase and clinopyroxene are totally altered into sericite, chlorite, carbonate and quartz and the initial shape of the phenocrysts is hardly recognizable (Fig. 2c) or destroyed (Fig. 2d). Carbonate (ankerite and calcite) is heterogeneously distributed forming clusters inside altered gabbro, in place associated with illite, sulfides and/or quartz (Fig. 2d). K-micas are relatively common in the altered gabbro groundmass, with typical grain size of 5-10 µm, but less commonly up to 200-250 µm. Altered gabbro contains disseminated arsenopyrite, pyrite, and less commonly stibnite and berthierite.

4. Analytical methods

4.1. Whole rock composition

Samples were crushed and powdered in an agate mortar. Major and trace elements analyses were performed using by inductively coupled plasma optical emission spectrometry (ICP-OES) and mass spectrometry (ICP-MS) by the SARM (CRPG-CNRS, Nancy) and following standard analytical procedures (Carignan et al., 2001).

4.2. Mineral chemistry

Fe-Ti oxides and pyrite from hydrothermally altered gabbro were examined in polished thin-sections using reflected-light optical and scanning electron microscopes. Minerals were analyzed using Cameca SX-100 electron probe micro-analyzers at IFREMER (Brest, France) and at Université Laval (Québec, Canada). The major and minor elements analyzed are Fe, Mg, Mn, Ti, V, Cr, Ca, Al, Ni, Si for Fe-Ti oxides and Fe, S, As, Sb, Au, Zn, Cu, Ni, Co for pyrite and arsenopyrite. Analyses were performed using a 3 µm diameter beam, a 15 kV accelerating voltage, a beam current of 20 nA and a counting time of 20s on peak. Analytical conditions and calibration are detailed in Appendix A.1.

4.3. Trace elements in minerals

Trace and selected major element concentrations were determined by laser ablation-inductively coupled plasma-mass spectrometer (LA-ICP-MS) at LabMaTer in the Université du Québec à Chicoutimi (UQAC, Canada). Selected elements and isotopes for Fe-Ti oxides and pyrite analyses are listed in Appendices. Sulfur (^{34}S) was monitored to avoid signal interference of sulfides inclusions inside Fe-Ti oxides. Silicon, Ca and Ti were monitored to avoid signal interference from silicate and Fe-Ti oxides inclusions.

The LA-ICP-MS system used at UQAC consists of a RESOlution (ASI) 193nm excimer laser equipped with a S155 ablation cell (Laurin Technic) and coupled to a quadrupole Agilent 7900 ICP-MS. Ablation is carried out using a He carrier gas, mixed with Ar and N_2 before entering the ICP-MS. Alignment of the instrument and mass calibration was performed before each analytical session on the GSE-1g reference glass. Single analysis consists of 30 s of gas blank followed by 60 s of ablation. The beam size was dependent on the grain size of the analyzed mineral and ranged between 25 and 55 µm. A repetition rate of 17 Hz, and a laser beam energy of 3 J/cm² (Fe-Ti oxides) and 2 J/cm² (pyrite) were used during analyses. Analytical conditions and calibration are detailed in Appendix A.2.

Iron (^{57}Fe) was used as the internal standard for Fe-oxides and pyrite, whereas ^{47}Ti was used for rutile because of the low concentration of Fe in rutile. Following the approaches of Dare et al., (2014) calibration for Fe-Ti oxide minerals was performed on GSE-1g. To monitor the quality of analyses, we used the certified reference materials GSD-1g (synthetic basalt glass), and Gprob6 (matrix artificial basalt glass) and an in-house monitor BC28 which consists of a natural Ti-rich magnetite from the Bushveld complex (Barnes et al., 2004; Dare et al., 2012). Analyses of GSD-1g and Gprob6 show good accuracy and precision, with a relative differences (RD) and relative standard deviations (RSD) for all elements < 10 % (Appendix A.3). The accuracy and precision for the in-house monitor BC28 are < 15 % for RD and RSD for most elements. This in-house monitor is a natural magnetite, hence some elements are heterogeneously distributed within crystal lattice, such as Cu that is underestimated by 65 %. The accuracy and precision of rutile

analyses are less good because of the low content of Ti (450 ppm) in the external standard GSE-1g. All elements of GSD-1g are underestimated by 20 % with a RSD < 10 % whereas the RD and RSD are < 15 % for Gprob6 (Appendix A.4). Isobaric interferences were checked following Dare et al. (2012, 2014). This revealed that ^{90}Zr is constantly and slightly underestimated compared to ^{91}Zr and the certified values for GSD-1g and Gprob6. Zirconium (^{91}Zr) values are close to those reported for GSD-1g and Gprob6, hence ^{91}Zr values were used when reporting Zr concentrations.

For pyrite, calibration of PGE and Au was performed using reference material po-727 (a synthetic FeS doped in PGE and Au, provided by Memorial University of Newfoundland). For the remaining elements, MASS-1 (a ZnFeCuS pressed pellet doped in trace elements, provided by the USGS) was used for calibration. The calibration was monitored using JBMSS-5 (synthetic FeS sulfide doped in trace elements, provided by Prof. James Brenan). Analyses are in good agreement within the analytical error with a RD and RSD < 10 % for GSE-1g except for Cd, Sn, Ir and Tl. For the in-house monitor JB-MSS5, the accuracy of analyses are relatively good with a RD < 15 % and a RSD < 10 %, except for Co and Re (Appendix A.5).

5. Results

5.1. Major element composition of Fe-Ti oxides

5.1.1. Least altered dyke

The magmatic Fe-Ti oxides mainly consist of ilmenite and titanohematite (Appendix A.6; Table 1; Fig. 3a-d) plotting along the true solid solution between the ilmenite and hematite end-members (Fig. 4). Although hematite exsolutions are observed in both ilmenite and titanohematite, selected areas for analyses have been carefully checked using scanning electron microscope in order to avoid exsolutions.

These two types of Fe-Ti oxides are frequently in a closely associated mineral assemblage of ilmenite and titanohematite (Fig. 3c-d). Ilmenite contains approximately 49 % TiO_2, whereas titanohematite contains close to 20 % TiO_2. Using the equations of Droop (1987), an estimate of Fe^{2+}/Fe^{3+} yields approximatively 42 % FeO and 6 % Fe_2O_3 for ilmenite, and 17 % FeO and 61 % Fe_2O_3 for titanohematite. Titanohematite contains mainly lamellar exsolutions (<2 µm) of ilmenite, hematite and possibly magnetite. Lamellae are often composite as they can contain at least ilmenite and hematite in exsolution (Fig. 3a). Other types of exsolution include “fish-bone” and mosaic textures. The “fish-bone” exsolution consists of nm-scale exsolution of ilmenite and hematite oriented parallel and perpendicularly to the c-axis of titanohematite crystals (Fig. 3b and c). The mosaic texture is characterized by a µm-scale disordered patchwork of phase exsolution of ilmenite and hematite with the presence of some micropores (Fig. 3b-d).

5.1.2. Hydrothermally altered dyke

One of the main textural characteristics of altered dykes is the replacement of primary ilmenite-titanohematite by rutile. According to its grain size, rutile can be divided in two types: coarse grained (CG) rutile and fine grained (FG) rutile (Figs. 3e, f and h), and both types appear to be contemporaneous. Coarse grained rutile is characterized by 99 % TiO_2 (Table 1; Fig. 4). It crystallizes with an irregular habit within the preserved shape of the parent crystal (Fig. 3g). Its grain size is variable and ranges between 10 and 80 µm. It is frequently cracked and the preserved shape contains interconnected micron-scale pores between CG rutile (Fig. 3e-f). Some Sb-sulfosalts are found filling micro-pores and micro-fractures (Fig. 3e). Fine grained rutile consists of intergrowths of rutile with others silicates and it is always associated with CG rutile. Because of its very small grain size (< 2µm) and the porosity between grains, TiO_2 is under-estimated in electron microprobe analyses (Table 1; Fig. 4). It consists of 76 % TiO_2 and 8 % $Fe_2O_{3\ total}$. Fine grained rutile is restricted to fractures and to the external rim of preserved shape of the parent mineral (Fig. 3e, f and h).

Selected X-ray chemical maps of the two types of rutile are displayed in Figure 5. They show that Ti and V are exclusively incorporated in both rutile and that these elements appear to be immobile during alteration and restricted inside the preserved shape of

the parent mineral (Fig. 5a and b). Micro-pores between CG and FG rutile crystals are filled by illite, ankerite, calcite and rare quartz (Fig. 5c-f).

Compositions of arsenopyrite and pyrite show that they contain Sb in minor and trace proportions, respectively (Appendix A.7 and A.8). Moreover, pyrite contains significant traces of arsenic and gold. Arsenopyrite and pyrite are texturally synchronous and/or slightly subsequent to breakdown of ilmenite-titanohematite assemblage, because they frequently encompass (Fig. 3g) or cut them (Fig. 3h). They may also replace primary ilmenite exsolutions (Fig. 3g).

5.2. Trace element composition of Fe-Ti oxides

Distribution of trace elements in ilmenite, titanohematite, CG and FG rutile are summarized in Table 2 (complete analyses in Appendix A.9), and plotted on multi-element variation diagrams (Fig. 6) and bivariate diagrams (Fig. 7). Ilmenite crystals are moderately homogeneous between individual grains (Fig. 6a). Moderately compatible elements (Mn, V, Cr, Co, Ni) and HFSE show small variations, whereas the sum of total HFSE is more variable (Fig. 7). Molybdenum, Sb, W, Pb and U, considered as incompatible elements into ilmenite (Klemme et al., 2006), exhibit strong variations up to 2 orders of magnitude (Fig. 6, 7a and b). Mean concentrations of trace elements show that ilmenite grains are characterized by high concentrations of Mn, V, Cr, Zn and Zr (140-14500 ppm), moderate concentrations of Co, Ni, Cu, Sc, Hf, Nb and Ta (5-90 ppm), and low concentrations of As, Sn, Mo, Sb, W, Pb and U (< 2 ppm). Compositionally, titanohematite is less homogeneous between individual crystals than ilmenite grains (Fig. 6b). For example, Cr shows significant variation with a range of values between 2 and 11000 ppm and a mean of 1100 ppm. This variation can be explained by numerous nm-scale exsolutions in various proportions in different grains. However, other elements (HFSE, V, Mn and Co) show small or no significant variations (Fig 6b and 7). In titanohematite, there is a significant decrease of Sc (7.3 ppm) and an increase of As (4.9 ppm) compared to ilmenite grains. Antimony is more enriched in titanohematite (Fig. 6b). Zinc has a high concentration (75-1660 ppm) likely related to its compatible behavior in Fe-Ti oxides (Klemme et al., 2006).

Coarse grained rutile displays a homogeneous trace element composition with the exception of Mn, Co, Ni, As, Sb and W, which show variations in composition between individual grains. Compared to ilmenite and titanohematite, Mn, Co and Ni are depleted, and Sb and W are enriched (Fig. 6c). The Zn concentration (< 15 ppm) is much lower than in ilmenite and titanohematite (Fig. 7a), whereas the V concentration is similar (Fig. 7b). With respect to Sb, there is a sharp limit in concentration in CG rutile defining two distributions (Fig. 7c): some rutile has a relatively low concentration of Sb (< 10 ppm), whereas others have high concentrations of Sb (> 100 ppm). This suggests that CG rutile with low Sb concentration has a Sb concentration relatively close to its precursor mineral, and likely to preserve the signature of the precursor mineral, in contrast with CG rutile with high Sb concentration. The trace element composition of FG rutile is homogeneous with no significant variation (Fig. 6d). Its trace element composition is similar to that of coexisting CG rutile, except for the enrichment in Co and Ni.

6. Discussion

The trace element patterns reveal that the main changes in composition between ilmenite-hematite and rutile are the depletion in Zn, and the enrichment in Sb and W in rutile. High field strength elements (HFSE) appear to be immobile through the transformation. Partitioning behavior of several trace elements between ilmenite and melt (Klemme et al., 2006), between rutile and melt (Foley et al., 2000; Klemme et al., 2005) and between rutile and fluid (Brenan et al., 1994; Stalder et al., 1998) provide a framework to investigate the trace element composition of these minerals during the breakdown of Fe-Ti oxides under hydrothermal conditions. The partitioning of trace elements during the breakdown of ilmenite in the presence of fluids, and the Sb behavior between rutile and fluid, however, is less well constrained.

6.1. Metasomatic change of gabbro dyke

Hydrothermal alteration associated with Sb mineralization causes metasomatic change of the gabbro dyke composition consistent with the mineralogical transformations previously described. These geochemical variations are displayed in Table 3 and in the isocon diagram (Fig. 8; Grant, 1986, 2005). Based on lowest loss on ignition (LOI) values, the least altered sample (SEM2) was selected to represent the protolith gabbro composition. However, as hydrothermal alteration is pervasive throughout the area, a degree of alteration was unavoidable. We define our isocon, using the following elements that are considered immobile, Al2O3, TiO2, P2O5, Hf, Zr, Nb, Ta, Sc, Th, Y and some REE. Figure 8 shows that alteration is associated with significant mass gains in K and Ca, accompanied by Rb, Cs and As, and a significant mass loss in Na. This is consistent with the destruction of plagioclase and growth of illite during potassic alteration. Leaching of plagioclase will release Na into the fluids, whereas the formation of illite accounts for the enrichment of K, Rb and Ba. Plagioclase dissolution should release Ca, however carbonate precipitation causes an overall mass gain in Ca. The isocon diagram shows that As (mainly contained in arsenopyrite) correlates with potassic alteration and carbonation (Fig. 8). In contrast to As, Sb shows no significant mass change. Even if some dissemination of Sb-sulfides (stibnite and berthierite) with carbonates is observed in altered gabbro, this can be easily explained because arsenopyrite is more abundant in altered gabbro, whereas Sb-sulfides are mainly found inside veins. Furthermore, this may also indicate that our least altered sample (SEM2) was anomalous in Sb, and consequently that Sb was concentrated either during magmatic processes within the gabbroic dyke or was enriched during early pervasive alteration of the dyke. Silica shows no mobility despite quartz neo-crystallization. Iron also shows no mobility and may indicate that all Fe in the altered gabbroic rocks comes from the protolith, likely from the breakdown of ilmenite-titanohematite assemblage and clinopyroxene. Alteration is characterized by a small overall mass gain of 10 % (Fig. 8).

6.2. Growth of hydrothermal rutile

From petrographic observations, we infer that rutile grew during hydrothermal alteration of the dykes, concomitant with breakdown of ilmenite. Numerous natural and experimental studies show that the recrystallization of ilmenite to rutile typically occurs via pseudomorphic replacement (van Dyk et al., 2002; El-Hazek et al., 2007; Janssen et al., 2010; Janssen and Putnis, 2011). This mineral reaction process can be explained by two main models. First, the classical solid-state model involves a two-stage alteration mechanism (Grey and Reid, 1975; Mücke and Bhadra Chaudhuri, 1991; Ignatiev, 1999; Schroeder et al., 2002; Grey and Li, 2003): (i) a first stage of solid-state diffusion of iron and oxidation of Fe^{2+} to form a transitional phase, pseudorutile, and (ii) a second stage where iron is leached from pseudorutile, causing concentration of Ti and subsequent precipitation of rutile.

The other model proposed as an alternative to the classical solid-state transformation, consists of the direct transformation of ilmenite to rutile via an interface-coupled dissolution-precipitation process (Janssen et al., 2010). The general principle of this mechanism is that an aqueous fluid causes dissolution of the parent mineral, producing an interfacial supersaturated fluid relative to the more stable product phase(s). These phases may nucleate at the surface of the parent mineral in epitaxial relation and initiate an autocatalytic reaction that couples dissolution and precipitation (Putnis, 2002, 2009; Janssen et al., 2010; Ruiz-Agudo et al., 2014).

Our textural observations and chemical analyses are consistent with the breakdown of ilmenite-titanohematite being via interface-coupled dissolution-reprecipitation process. For example, direct recrystallization of ilmenite to rutile is strongly suggested by associated porosity, and by lack of intermediate products (pseudorutile).

The newly formed rutile (i.e. CG and FG rutile) contains a strong interconnected network of µm-scale porosity. These pores are filled with later ankerite, calcite, quartz or illite (Fig. 3c-f and 5). CG rutile also contains numerous cracks mainly filled by FG rutile. Some cracks appear to have formed prior to the pseudomorphic replacement reaction (Fig. 3d). Infiltration of the fluid toward the core of the precursor mineral to generate fresh reaction surfaces is critical to the interface-coupled dissolution-reprecipitation process (Putnis and Austrheim, 2010, Putnis et al. 2005). Cracks and pores would have provided effective pathways for fluid infiltration, and

provide further evidence that these mineral reactions occurred via interface-coupled dissolution-reprecipitation processes. The occurrence of FG rutile around the preserved shape of precursor mineral and inside fractures (Fig. 3e and f) may represent paleo-reaction fronts.

Volume reduction associated with the recrystallization of ilmenite to rutile has previously been calculated at 40 % (Mücke and Bhadra Chaudhuri, 1991). In our samples, as the ratio ilmenite / titanohematite is not precisely known, we have estimated the volume change using the area of rutile in the preserved external shape of the precursor mineral parent by image analysis (e.g., Fig. 3c-f). Using this method, the volume reduction in our sample is estimated at 45 %. The small difference in volume change between ours and Mücke and Bhadra Chaudhuri (1991) values, is likely related to fact that the Le Semnon precursor mineral is not pure ilmenite, but an assemblage of ilmenite and titanohematite. Such volume reduction, combined with slight mass increase in the whole rock implicate a density increase probably related to the precipitation of sulfides, a process able to increase the rock density.

6.3. Redistribution of trace elements

A mineral replacement process may facilitate incorporation of elements from an external source and/or release of some elements to others phases or fluids, and hence contribute to the redistribution of elements in the Earth's crust and to mineralization processes (Rabbia et al., 2009; Lucassen et al., 2010; Putnis and Fernandez-Diaz, 2010; Pitcairn et al., 2014, 2015; Cave et al., 2015). An assessment of what elements are retained, released, or incorporated during coupled dissolution-reprecipitation mechanism can provide information about the mobility of trace elements, especially metals, during hydrothermal alteration. Thus, the geochemistry of ilmenite, titanohematite and rutile can be used to constrain the mass balance of the reaction and to quantify the mobility of trace elements during hydrothermal breakdown of Fe-Ti oxides related to Sb-mineralizing hydrothermal event.

The mineral assemblage composed of ilmenite and titanohematite is considered the precursor mineral because these two minerals are rarely found alone (Fig. 3c-d), which does not exclude the fact that the breakdown of ilmenite (or titanohematite) alone can also lead to rutile precipitation. Because of lesser quality microprobe analyses of FG rutile compared to CG rutile, we only consider CG rutile as the product mineral of the reaction. Assuming direct transformation, the overall mineral reaction can be written as:

$$Fe^{2+}TiO_3 + \left(Fe_x^{2+}, Fe_{2-2x}^{3+}\right)Ti_xO_3 + \downarrow fluid \uparrow \rightharpoonup (1+x)TiO_2 + [(1+x)Fe^{2+} + (2-2x)Fe^{3+}]_{solution} + \downarrow fluid \uparrow$$

Because the fluid composition is unknown, this theoretical mineral reaction cannot be balanced, but it illustrates that the destabilization of the mineral assemblage of ilmenite and titanohematite leads to rutile precipitation and a release of iron in fluids. The mass balance of this reaction has been calculated following the approach of Gresens (1967). The density calculation follows Rabbia and Hernández (2012) and the required unit cell parameters are taken from Mücke and Bhadra Chaudhuri (1991) and Brown et al. (1993). The volume factor corresponds to the volume reduction between the precursor mineral and its product, estimated at ~ 45 % at the Le Semnon mine. Assuming that (1) Ti is completely incorporated in rutile and consequently it is immobile during the reaction and (2) trace elements from the precursor mineral are conservatively incorporated in rutile, the mass balance of the reaction indicates that, for a complete transformation, it requires 100 g of ilmenite and 2.9 g titanohematite to nucleate 50.1 g rutile which implies a release of 42.5 g FeO + 7.65 g Fe_2O_3 + 2.07 g MnO. As predicted by the mineral reaction, most elements, iron in particular, are released into the fluid phase during the reaction. Considering, the low TiO_2 concentration in titanohematite, it is likely that titanohematite contributes to a small proportion of titanium in the nucleation of rutile, and a large proportion of iron into the fluid. Taking into account the stoichiometry of the reaction, 102.9 g of precursor minerals is necessary to produce 50.1 g of product mineral, such that a concentration factor of ~ 2.1 is calculated. This factor can be used to investigate what element will be incorporated into the newly formed mineral or released into the fluid (Gresens, 1967; Lucassen et al., 2010; Cave et al., 2015).

Using this concentration factor, we calculated the trace element composition of hydrothermal rutile using the average measured trace elements concentrations of precursor minerals, ilmenite and titanohematite (Table 4). The mean of hydrothermal rutile trace element concentrations was normalized using calculated hydrothermal rutile trace element values (Fig.9). Values < 1 indicate an element concentration lower than predicted by the calculation, therefore suggesting that this element was released into the fluid and/or incorporated into another mineral phase. Values ≈ 1 and > 1 correspond to retention from precursor minerals, or addition from an external source (such as a reactive fluid phase), respectively. In Figure 8, a comparison between calculated and measured values for hydrothermal rutile shows that most elements (HFSE, V, Cr, Cu, As, Sc, and Pb) have values ~ 1 indicating that they are sequestered by rutile precipitation, likely attesting to their compatible behavior in rutile, in particular the HFSE (Foley et al., 2000; Zack et al., 2002; Klemme et al., 2005). The remaining elements identified as being released into fluid phase and/or partitioned into other mineral phases are Mn, Co, Ni, Sn, Mo, U and Zn. Antimony and W have values above 1, suggesting incorporation into rutile from an external fluid phase. This is consistent with the data displayed in Fig. 7a, which shows that Zn is depleted in rutile compared to ilmenite-hematite, and which indicates that the precursor mineral signature is not completely preserved. In contrast, the concentration of V is quite similar between rutile and ilmenite-hematite (Fig. 7b). This suggests that part of precursor signature is preserved in the reaction product, and that this element is immobile in the hydrothermal fluids. Antimony behaves differently from the other elements, forming CG rutile with the precursor trace element signature (i.e., low Sb concentration) and with a hydrothermal fingerprint (i.e., high Sb concentration, Fig. 7c). This may be explained by two hypotheses: (1) either the first rutile is Sb-poor and Sb becomes enriched in fluids during the replacement reaction; consequently, the last-formed rutile is Sb-rich or (2) the first rutile is Sb-rich followed by an input of sulfur in the system, which causes precipitation of sulfides (e.g., arsenopyrite, pyrite, berthierite and stibnite), leading to rutile with low Sb concentration later. Unfortunately, lack of textural criteria to constrain the time relationships between the two subtypes of rutile prevents assessment of the two hypotheses.

The release of trace elements into fluids during the breakdown of ilmenite-titanohematite may constitute a potential, local source of elements for newly-formed phases, such as Zn for the sphalerite in mineralized veins, Co and Ni for pyrite and arsenopyrite, and Mn for ankerite in hydrothermally altered gabbro. In contrast, Sb cannot come from this mineral replacement reaction, as Sb has been largely added by an external source (Fig. 9). The identification of the external source(s) for Sb is relatively complex as Sb is strongly mobile in fluids (Noll et al., 1996; Deschamps et al., 2015). Sb could have been leached from another mineral reaction in the gabbro or sedimentary country rocks, or a deep-seated source, possibly related to the parent magma intrusions of gabbroic dyke swarms.

Although quantitative mass balance was not performed on FG rutile, it is important to note that most elements are enriched compared to CG rutile, particularly metals such as Zn, As, Sb, and W (Fig. 6 and Table 3). In the previous section, FG rutile is interpreted as a “fossilized” replacement reaction front. The enrichment of metals (Sb in particular) is in agreement with this assumption. This suggests that sealed fractures in pseudomorphically replaced minerals might be useful in investigating element mobility during coupled dissolution-precipitation reactions. Thus, the concentration of Sb in both FG and CG rutile types suggests that percolating hydrothermal fluids were rich in Sb, during the replacement process.

7. Hydrothermal Sb alteration model

A model for the alteration process, and redistribution of elements in Fe-Ti oxides at the Le Semnon mine, is proposed for the early hydrothermal event prior to the main stage of Sb mineralization (Fig. 10a-c). First, petrography of unaltered and altered gabbro documents several mineral transformations as a result of pervasive hydrothermal alteration, particularly the breakdown of magmatic ilmenite-titanohematite into hydrothermal rutile. This breakdown was accompanied by a significant increase in K and Ca, and a significant decrease in Na in the whole rock gabbro, consistent with pervasive illite and carbonate precipitation in gabbro. Part of the

Ca was likely recycled from the destruction of plagioclase and clinopyroxene. The mineral replacement resulted from an interface-coupled dissolution-reprecipitation process. This autocatalytic reaction gradually generated porosity and micro fractures as a consequence of volume reduction which accelerated propagation of reaction fronts. This volume-change fracturing may have been coupled with tectonically-induced fracturing which would increase the progression of the reaction, but no evidence for tectonic fractures are recorded. These fluid pathways acted as the vector for redistribution of major and trace elements as illustrated in Fig. 10b. The mass balance indicates a release of Fe^{2+}, Fe^{3+}, Mn and Zn to the fluid phase, in a large part likely being sequestered by ankerite, Fe-sulfides and sphalerite precipitation. HFSE and Ti were retained by rutile precipitation, whereas Sb and W were carried by hydrothermal fluids and incorporated in the structure of rutile. Rutile recorded a sharp change in Sb concentration, likely corresponding to change in fluids composition and/or an input of sulfur in the hydrothermal system that resulted in sulfide precipitation, particularly arsenopyrite, pyrite, berthierite and stibnite (Fig. 10c).

8. Conclusion

The breakdown of magmatic ilmenite-titanohematite to hydrothermal rutile is associated with a redistribution of trace elements. This reaction is mainly characterized by a release of Fe, Mg, Mn and Zn into hydrothermal fluids, and the incorporation of Sb and W into hydrothermal rutile. The mineral replacement reaction is not a potential source for the Sb mineralization, but likely contributes to the precipitation of sphalerite and ankerite. The hydrothermal fingerprint of rutile indicates a change of fluid composition during mineral replacement. Because rutile is a common accessory mineral in hydrothermal alteration and Sb is commonly associated with orogenic and subduction-related gold and base metal deposits, it appears fundamental to improve the knowledge of the behavior of Sb during fluid/rock interactions in order to characterize alteration, especially the partitioning between ilmenite-titanohematite assemblage, rutile, sulfides and hydrothermal fluids. New experimental data are necessary in order to better constrain the partitioning of Sb between these minerals, particularly at temperatures lower than 400°C. This would provide quantitative information about the parameters which controls HFSE and chalcophile behavior of Sb in Ti-bearing hydrothermal systems.

Acknowledgement

This work was funded by the BRGM, the region of Brittany, the OSUR and the doctoral school SDLM, with contributions from the Natural Sciences and Engineering Research Council of Canada, Agnico Eagle Mines and the Ministère de l'Énergie et des Ressouces naturelles of Québec. The author thanks Xavier Le Coz for thin sections, Jessica Langlade (UBO) and Marc Choquette (Laval) for EPMA analyses, and Dany Savard and Philippe Pagé (UQAC) for their assistance with LA-ICP-MS analyses. Constructive reviews by Pr. Dave Craw and an anonymous reviewer have greatly improved the manuscript.

References

Aïfa, T., Lefort, J.P., Guennoc, P., 1999. Anisotropy of magnetic susceptibility investigations of the St Malo dyke swarm (Brittany, France): emplacement mechanism of doleritic intrusions. Geophys. J. Int. 139, 573–582.

Ballouard, C., Boulvais, P., Poujol, M., Gapais, D., Yamato, P., Tartèse, R., Cuney, M., 2015. Tectonic record, magmatic history and hydrothermal alteration in the Hercynian Guérande leucogranite, Armorican Massif, France. Lithos 220–223, 1–22.

Barnes, S-.J., Maier, W.D., Ashwal, L.D., 2004. Platinum-group element distribution in the Main Zone and Upper Zone of the Bushveld Complex, South Africa. Chem. Geol. 208, 293–317.

Bouchot, V., Ledru, P., Lerouge, C., Lescuyer, J.L., Milesi, J.P., 2005. 5: Late Variscan mineralizing systems related to orogenic processes: The French Massif Central. Ore Geol. Rev. 27, 169–197.

Brenan, J.M., Shaw, H.F., Phinney, D.L., Ryerson, F.J., 1994. Rutile-aqueous fluid partitioning of Nb, Ta, Hf, Zr, U and Th: implications for high field strength element depletions in island-arc basalts. Earth Planet. Sc. Lett. 128, 327–339.

Bromiley, G.D., Hilairet, N., 2005. Hydrogen and minor element incorporation in synthetic rutile. Mineral. Mag. 69, 345–358.

Brown, N.E., Navrotsky, A., Nord, G.L., Banerjee, S.K., 1993. Hematite-ilmenite (Fe_2O_3-$FeTiO_3$) solid solutions: Determinations of Fe-Ti order from magnetic properties. Am. Mineral. 78, 941–951.

Buddington, A.F., Lindsley, D.H., 1964. Iron–titanium oxide minerals and synthetic equivalents. J. Petrol. 5, 310–357.

Carignan, J., Hild, P., Mevelle, G., Morel, J., Yeghicheyan, D., 2001. Routine Analyses of Trace Elements in Geological Samples using Flow Injection and Low Pressure On-Line Liquid Chromatography Coupled to ICP-MS: A Study of Geochemical Reference Materials BR, DR-N, UB-N, AN-G and GH. Geostandards Newslett 25, 187–198.

Carruzzo, S., Clarke, D.B., Pelrine, K.M., MacDonald, M.A., 2006. Texture, composition, and origin of rutile in the South Mountain Batholith, Nova Scotia. Can. Mineral. 44, 715–729.

Cave, B.J., Stepanov, A.S., Craw, D., Large, R.R., Halpin, J.A., Thompson, J., 2015. Release of Trace Elements Through the Sub-Greenschist Facies Breakdown of Detrital Rutile to Metamorphic Titanite in the Otago Schist, New Zealand. Can. Mineral. 53, 379–400.

Chauris, L., Houlgatte, E., Laforêt, C., Picot, P., 1985. Un district antimono-aurifère à gangue quartzo-carbonatée : Le Semnon (Ille-et-Vilaine, Massif Armoricain, France). Hercynica 1, 111–119.

Chauris, L., Marcoux, E., 1994. Metallogeny of the Armorican Massif. In: Chantraine, J., Rolet, J., Santallier, D.S., Piqué, A., Keppie, J.D. (Eds.), Pre-Mesozoic Geology in France and Related Areas. Springer, Berlin Heidelberg, pp 243–264.

Clark, J.R., Williams-Jones, A.E., 2004. Rutile as a potential indicator mineral for metamorphosed metallic ore deposits. Rapport Final de DIVEX, Sous-projet SC2, Montréal, Canada. 17 pp.

Dare, S.A.S., Barnes, S-.J., Beaudoin, G., Méric, J., Boutroy, E., Potvin-Doucet, C., 2014. Trace elements in magnetite as petrogenetic indicators. Miner. Deposita 49, 785–796.

Dare, S.A.S., Barnes, S-.J., Beaudoin, G., 2012. Variation in trace element content of magnetite crystallized from a fractionating sulfide liquid, Sudbury, Canada: Implications for provenance discrimination. Geochim. Cosmochim. Ac. 88, 27–50.

Deschamps, F., Godard, M., Guillot, S., Hattori, K., 2013. Geochemistry of subduction zone serpentinites: A review. Lithos 178, 96-127.

Droop, G., 1987. A general equation for estimating Fe 3+ concentrations in ferromagnesian silicates and oxides from microprobe analyses, using stoichiometric criteria. Mineral. Mag. 51, 431–5.

El-Hazek, N., Lasheen, T.A., El-Sheikh, R., Zaki, S.A., 2007. Hydrometallurgical criteria for TiO2 leaching from Rosetta ilmenite by hydrochloric acid. Hydrometallurgy 87, 45–50.

Foley, S.F., Barth, M.G., Jenner, G.A., 2000. Rutile/melt partition coefficients for trace elements and an assessment of the influence of rutile on the trace element characteristics of subduction zone magmas. Geochim. Cosmochim. Ac. 64, 933–938.

Gapais, D., Le Corre, C., 1980. Is the Hercynian belt of Brittany a major shear zone. Nature 288, 574–576.

Gapais, D., Lagarde, J.L., Le Corre, C., Audren, C., Jégouzo, P., Casas Sainz, A., Van Den Driessche, J., 1993. La zone de cisaillement de Quiberon : témoin d'extension de la chaine varisque en Bretagne méridionale au Carbonifère. Cr. Acad. Sci. II 316, 1123–1129.

Gloaguen, E., Branquet, Y., Boulvais, P., Moelo, Y., Chauvel, J.J., Chiappero, P.J., Marcoux, E., 2007. Palaeozoic oolitic ironstone of the French Armorican Massif: a chemical and structural trap for orogenic base metal–As–Sb–Au mineralisation during Hercynian strike-slip deformation. Miner. Deposita 42, 399–422.

Gloaguen, E., Tourlière, B., Angel, J.M. 2016. Revalorisation du potentiel minier français : le district antimonifère du Semnon (Ille-et-Vilaine, France). BRGM report. BRGM/RP-66200-FR 71 pp.

Grant, J.A., 1986. The isocon diagram; a simple solution to Gresens' equation for metasomatic alteration. Econ. Geol. 81, 1976–1982.

Grant, J.A., 2005. Isocon analysis: A brief review of the method and applications. Phys. Chem. Earth Pt A/B/C 30, 997–1004.

Gresens, R.L., 1967. Composition-volume relationships of metasomatism. Chem. Geol. 2, 47-65.

Grey, I.E., Li, C., 2003. Hydroxylian pseudorutile derived from picroilmenite in the Murray Basin, southeastern Australia. Mineral. Mag. 67, 733-747.

Grey, I.E., Reid, A.F., 1975. The structure of pseudorutile and its role in the natural alteration of ilmenite. Am. Mineral. 60, 898–906.

Gumiaux, C., Gapais, D., Brun, J.P., Chantraine, J., Ruffet, G., 2004. Tectonic history of the Hercynian Armorican Shear belt (Brittany, France). Geodinamica Acta 17, 289–307.

Ignatiev, V.D., 1999. Solid phase mechanism of the ilmenite leucoxenisation. Lithol. Miner. Resour. 34, 184-189.

Jamtveit B, CV, Malthe-Sørenssen A (2009) Reaction induced fracturing during replacement processes. Contrib Mineral Petr 157:127-133.

Janssen, A., Putnis, A., 2011. Processes of oxidation and HCl-leaching of Tellnes ilmenite. Hydrometallurgy 109, 194–201.

Janssen, A., Putnis, A., Geisler, T., Putnis, C.V., 2010. The experimental replacement of ilmenite by rutile in HCl solutions. Mineral. Mag. 74, 633–644.

Klemme, S., Günther, D., Hametner, K., Prowatke, S., Zack, T., 2006. The partitioning of trace elements between ilmenite, ulvospinel, armalcolite and silicate melts with implications for the early differentiation of the moon. Chem. Geol. 234, 251–263.

Klemme, S., Prowatke, S., Hametner, K., Günther, D., 2005. Partitioning of trace elements between rutile and silicate melts: Implications for subduction zones. Geochim. Cosmochim. Ac. 69, 2361-2371.

Lahaye, Y., Blais, S., Auvray, B., Ruffet, G., 1995. Le Volcanisme fissural paleozoique du domaine nord-armoricain. B. Soc. Geol. Fr. 166, 601-612.

Le Gall, J., 1999. Les dolérites et basaltes tholéiitiques varisques du domaine nord-est armoricain. Géologie de la France 4, 3-26.

Lucassen, F., Dulski, P., Abart, R., Franz, G., Rhede, D., Romer, R.L., 2010. Redistribution of HFSE elements during rutile replacement by titanite. Contrib. Mineral. Petr. 160, 279 – 295

Luvizotto, G.L., Zack, T., Triebold, S., von Eynatten, H., 2009. Rutile occurrence and trace element behavior in medium-grade metasedimentary rocks: example from the Erzgebirge, Germany. Miner. Petrol. 97, 233-249.

Malthe-Sørenssen, A., Jamtveit, B., Meakin, P., 2006. Fracture patterns generated by diffusion controlled volume changing reactions. Phys. Rev. Lett. 96, 245-501.

Meinhold, G., 2010. Rutile and its applications in earth sciences. Earth Sci. Rev. 102, 1-28.

Mücke, A., Bhadra Chaudhuri, J.N., 1991. The continuous alteration of ilmenite through pseudorutile to leucoxene. Ore Geol. Rev. 6, 25-44.

Morad, S., Aldahan, A.D., 1986. Alteration of detrital Fe-Ti oxides in sedimentary rocks. Geol. Soc. Am. Bull. 97, 567-578.

Noll, P.D., Newsom, H.E., Leeman, W.P., Ryan, J.G., 1996. The role of hydrothermal fluids in the production of subduction zone magmas: Evidence from siderophile and chalcophile trace elements and boron. Geochim. Cosmochim. Ac. 60, 587-611.

Pitcairn, I.K., Craw, D., Teagle, D.A.H., 2014. The gold conveyor belt: Large-scale gold mobility in an active orogeny. Ore Geol. Rev. 62, 129-142.

Pitcairn, I.K., Craw, D., Teagle, D.A.H., 2015. Metabasalts as sources of metals in orogenic gold deposits. Miner. Deposita 50, 373-390.

Pochon, A., Gapais, D., Gloaguen, E., Gumiaux, C., Branquet, Y., Cagnard, F., Martelet, G., 2016a. Antimony deposits in the Variscan Armorican belt, a link with mafic intrusives? Terra Nova 28, 138–145.

Pochon, A., Poujol, M., Gloaguen, E., Branquet, Y., Cagnard, F., Gumiaux, C., Gapais, D., 2016b. U-Pb LA-ICP-MS dating of apatite in mafic rocks: Evidence for a major magmatic event at the Devonian-Carboniferous boundary in the Armorican Massif (France). Am. Mineral. 101, 2430–2442.

Putnis, A., 2002. Mineral replacement reactions: from macroscopic observations to microscopic mechanisms. Mineral. Mag. 66, 689–708.

Putnis, A., 2009. Mineral Replacement Reactions. Reviews in Mineralogy and Geochemistry 70, 87–124.

Putnis, A., Austrheim H., 2010. Fluid-induced processes: metasomatism and metamorphism. Geofluids 10, 254–269.

Putnis, C.V., Fernandez-Diaz, L., 2010. Ion Partitioning and Element Mobilization During Mineral Replacement Reactions in Natural and Experimental Systems. EMU Notes in Mineralogy: Ion Partitioning in Ambient Temperature Aqueous Systems, 10, 189–226.

Rabbia, O.M., Hernández, L.B., French, D.H., King, R.W., Ayers, J.C., 2009. The El Teniente porphyry Cu–Mo deposit from a hydrothermal rutile perspective. Miner. Deposita 44, 849–866.

Rabbia, O.M., Hernández, L.B., 2012. Mineral chemistry and potential applications of natural-multi-doped hydrothermal rutile from porphyry copper deposits. In: It-Meng (Jim) Low (Ed.), Rutile: Properties, Synthesis and Application. Nova Science Publishers, Inc., pp 209-228.

Rice, C., Darke, K., Still, J., 1998. Tungsten-bearing rutile from the Kori Kollo gold mine Bolívia. Mineral. Mag. 62, 421–429.

Ruiz-Agudo, E., Putnis, C.V., Putnis, A., 2014. Coupled dissolution and precipitation at mineral–fluid interfaces. Chem. Geol. 383, 132–146.

Schroeder, P., Le Golvan, J., Roden, M., 2002. Weathering of ilmenite from granite and chlorite schist in the Georgia Piedmont. Am. Mineral. 87, 1616-1625.

Scott, K.M., 2005. Rutile geochemistry as a guide to porphyry Cu–Au mineralization, Northparkes, New South Wales, Australia. Geochem. Explor. Env. A 5, 247–253.

Scott, K.M., Radford, N.W., 2007. Rutile compositions at the Big Bell Au deposit as a guide for exploration. Geochem. Explor. Env. A 7, 353–361.

Smith, D.C., Perseil, E.A., 1997. Sb-rich rutile in the manganese concentrations at St. Marcel-Praborna, Aosta Valley, Italy; petrology and crystal-chemistry. Mineral. Mag. 61, 655–669.

Stalder, R., Foley, S.F., Brey, G.P., Horn, I., 1998. Mineral–aqueous fluid partitioning of trace elements at 900 °C–1200 °C and 3.0 GPa to 5.7 GPa: new experimental data set for garnet, clinopyroxene and rutile and implications for mantle metasomatism. Geochim. Cosmochim. Ac. 62, 1781–1801.

Tartèse, R., Boulvais, P., 2010. Differentiation of peraluminous leucogranites “en route” to the surface. Lithos 114, 353–368.

Tartèse, R., Poujol, M., Ruffet, G., Boulvais, P., Yamato, P., Košler, J., 2011a. New U-Pb zircon and 40Ar/39Ar muscovite age constraints on the emplacement of the Lizio syn-tectonic granite (Armorican Massif, France). C. R. Geosci. 343, 443–453.

Tartèse, R., Ruffet, G., Poujol, M., Boulvais, P., 2011b. Simultaneous resetting of the muscovite K-Ar and monazite U-Pb geochronometers: a story of fluids. Terra Nova 23, 390–398.

Tartèse, R., Poujol, M., Gloaguen, E., Boulvais, P., Drost, K., Košler, J., Ntaflos, T., 2015. Hydrothermal activity during tectonic building of the Variscan orogen recorded by U-Pb systematics of xenotime in the Grès Armoricain formation, Massif Armoricain, France. Miner. Petrol. 109, 485–500.

Tomkins, H.S., Powell, R., Ellis, D.J., 2007. The pressure dependence of the zirconium-in-rutile thermometer. J. Metamorph. Geol. 25, 703–713.

Triebold, S., von Eynatten, H., Luvizotto, G.L., Zack, T., 2007. Deducing source rock lithology from detrital rutile geochemistry: an example from the Erzgebirge, Germany. Chem. Geol. 244, 421–436.

Urban, A.J., Hoskins, B.F., Grey, I.E., 1992. Characterization of V–Sb–W-bearing rutile from the Hemlo gold deposit, Ontario. Can. Mineral. 30, 319–326.

van Dyk, J.P., Vegter, N.M., Pistorius, P.C., 2002. Kinetics of ilmenite dissolution in hydrochloric acid. Hydrometallurgy 65, 31–36.

Whitney, D.L., Evans, B.W., 2010. Abbreviations for names of rock-forming minerals. Am. Mineral. 95, 185-187.

Williams, S.A., Cesbron, F.P., 1977. Rutile and apatite: useful prospecting guides for porphyry copper deposits. Mineral. Mag. 41, 288-292.

Zack, T., John, T., 2007. An evaluation of reactive fluid flow and trace element mobility in subducting slabs. Chem. Geol. 239, 199-216.

Zack, T., Kronz, A., Foley, S.F., Rivers, T., 2002. Trace element abundances in rutiles from eclogites and associated garnet mica schists. Chem. Geol. 184, 97–122.

Zack, T., von Eynatten, H., Kronz, A., 2004. Rutile geochemistry and its potential use in quantitative provenance studies. Sediment. Geol. 171, 37-58.

Figure captions

Fig. 1 a Geological map of the Semnon Sb-Au district with the location of the old Semnon mine and other Sb occurrences (modified from Pochon et al. 2016a). See text for abbreviation. Photographs of outcrops showing at the Semnon deposit: (**b**) relation between Ordovician slates, gabbro dyke, and regional cleavage (S1), (**c**) the location and geometry of flat stibnite-bearing veins cutting the gabbro and (**d**) alteration zone of the vein wallrock (Ordovician slates) with disseminated arsenopyrite.

Fig. 2 Photomicrographs showing the initial magmatic texture of an unaltered gabbro from the dyke swarm (**a** and **b**) and the hydrothermally altered gabbro from the Le Semnon deposit (**c** and **d**). **a** Typical texture of gabbro dyke (BAN1) with laths of plagioclase intergrown with clinopyroxene. Areas delineated by white dashed lines correspond to Fe-Ti oxides. **b** Fe-Ti oxides in the groundmass of TOU1 sample. **c** Typical texture of altered gabbro (SEM12) with replaced phenocrysts of sericitized plagioclase (F. Pl), clinopyroxene (F. Cpx) and interstitial quartz. **d** Strong hydrothermal alteration of gabbro (SEM12) with illite, sericite, carbonates, quartz and rutile. Abbreviation from Whitney and Evans (2010).

Fig. 3 SEM photomicrographs showing the texture of Fe-Ti oxides in the unaltered gabbro BAN1 (**a-d**) and the hydrothermally altered gabbro SEM9 and SEM11 (**e-h**). **a** Crystal of titanohematite (Ti-Hem) with typical lamellar exsolutions. Insert in the upper right corner represents zoom of the lamellar exsolutions. **b** Crystal of titanohematite with the mosaic (M) and the "fish-bone" (F) textures. Insert in the upper right corner represents zoom of the "fish-bone" texture. **c** Mineral assemblage composed of a core of ilmenite and a rim of titanohematite. Insert in the upper left corner shows occurrences of mosaic and "fish-bone" textures in ilmenite. **d** Ilmenite crystal displaying altered areas with overgrowth of Ilm-Hem ss crystals. **e** Ghost of ilmenite-titanohematite assemblage of SEM9 sample, with its preserved external shape, replace by coarse grained rutile (CG rutile) crystals. These crystals exhibit a strong porosity and they are frequently cracked. Insert, in the lower left corner, shows very fine grain of rutile mainly located in micro-crack and defined as fine grained rutile (FG rutile). The insert in the upper right corner shows a Sb-sulphide inclusion within CG rutile and a micro-crack filled by Sb-sulphide. **f** Ghost of ilmenite-titanohematite assemblage of SEM11 sample replace by CG and FG rutile. Crystals are cracked and some of these cracks are partially sealed as shown in the insert in the upper right corner. **g** Ghost of ilmenite invades and includes inside arsenopyrite. **h** Overgrowth of pyrite and Sb-sulfides inside invagination of rutile. Abbreviation from Whitney and Evans (2010).

Fig. 4 Ternary system FeO-Fe_2O_3-TiO_2 showing the high-temperature solid solution series magnetite-ulvöspinel, hematite-ilmenite, pseudobrookite-ferropseudobrookite (modified from Buddington and Lindsley, 1964)

Fig. 5 X-ray chemical map of the distribution of the major elements of rutile grains displayed in the Fig. 3c. **a** Ti Kα, **b** V Kα, **c** Fe Kα, **d** Al Kα, **e** Si Kα and **f** Ca Kα

Fig. 6 Multi-element variation diagrams of trace elements composition of Fe-Ti oxides. **a** Trace element concentration of ilmenite, and **b** titanohematite from unaltered gabbro. **c** Trace element concentration of coarse grained rutile, and **d** fine grained rutile from the hydrothermally altered gabbro

Fig. 7 Bivariate diagrams of selected trace elements (Sb, V and Zn) versus HFSE concentration represented by Zr, Hf, Nb and Ta. **a** HFSE vs Zn concentration, **b** HFSE vs V concentration and **c** HFSE vs Sb concentration.

Fig. 8 Isocon diagram comparing the least altered with altered samples from the same gabbro dyke from the Semnon Sb-Au deposit. Major and trace elements values are scaled in order to compare the data to the best advantage but the scaling does not affect the results

Fig. 9 Trace element profile for the average composition of hydrothermal CG rutile normalized to CG rutile composition calculated after Gresens (1967) for the Le Semnon gabbro dyke. See text for methodology

Fig. 10 Model of alteration process for the early hydrothermal event. **a** Stage 1: initiation of mineral replacement with progressive infiltration of fluids. Magmatic texture is preserved and Sb concentration is low in the precursor mineral assemblage composed of ilmenite and titanohematite. **b** Stage 2: progression of the reaction with the increase of hydrothermal alteration of gabbro and rutile precipitation. The altered dyke is enriched in K, Ca, Rb, Sr, Ba, Cs, Sb and W, and depleted in Na. Volume reduction associated with the mineral replacement reaction generates porosity and fractures inside the parent crystal and, consequently, promote the reaction front propagation. During the cementation of fluid pathways, the reaction principally releases iron, retains Ti, and incorporates external Sb. **c** The final stage ends the reaction by filling of the porosity by illite, quartz, carbonates and sulfide precipitation.

Table 1
Representative electron microprobe analyses of Fe-Ti oxides from gabbro of Semnon Sb-Au district

		Ilmenite		Titanohematite			Coarse grained rutile		Fine grained rutile	
Wt. Oxides %	**[a]D.L.**	**Mean (n = 25)**	**Stdev**	**Mean (n = 26)**	**Stdev**	**[b]D.L.**	**Mean (n = 91)**	**Stdev**	**Mean (n = 15)**	**Stdev**
SiO2	0.012	0.024	0.017	0.135	0.197	0.036	0.131	0.060	7.595	3.149
Al2O3	0.011	0.059	0.057	0.360	0.380	0.035	0.167	0.218	4.535	2.177
TiO2	0.025	49.208	0.520	19.979	2.007	0.050	99.313	0.719	78.954	5.821
V2O3	0.274	bdl	0.178	0.553	0.188	0.008	0.677	0.144	0.490	0.139
Cr2O3	0.037	0.035	0.027	0.135	0.197	0.010	0.033	0.028	0.029	0.021
FeO	0.170	42.014	0.872	16.940	1.860	0.076			6.311	3.258
Fe2O3	0.128	6.034	0.986	61.366	4.407	0.075	0.300	0.430		
MnO	0.014	2.041	0.674	1.006	0.552	0.032			[c] 0.509	
MgO		0.058	0.024	0.030	0.040	0.024	[c] 0.056		1.865	0.987
CaO									0.281	0.256
Total		99.830	0.386	100.528	0.831		100.895	0.501	98.388	1.592
% Ilm		93.8		37.6						
% Hem		6.2		62.4						
apfu on the basis of a 6 oxygen equivalent							**apfu on the basis of a 4 oxygen equivalent**			
Si		0.001	0.001	0.007	0.005		0.004	0.001		
Al		0.003	0.003	0.020	0.011		0.005	0.007		
Ti		1.876	0.020	0.777	0.040		1.966	0.013		
V		0.013	0.007	0.023	0.004		0.014	0.003		
Cr		0.001	0.001	0.005	0.004		0.001	0.001		
Fe 3+		0.230	0.037	2.386	0.083		0.006	0.008		
Fe 2+		1.781	0.036	0.732	0.041					
Mn		0.088	0.029	0.044	0.012					
Mg		0.004	0.002	0.002	0.002		0.002			

[a] detection limit of analyses from electron microprobe at the Université Laval
[b] detection limit of analyses from electron microprobe at IFREMER
[c] only one value from all samples
Abbreviations: D.L., detection limit; Ave, average; Stdev, standard deviation

Table 2
Summary of LA-ICP-MS results for trace elements composition of Fe-Ti oxides from gabbro of Semnon Sb-Au district

		Least altered gabbro				Hydrothermally altered gabbro			
		Ilmenite		Titanohematite		CG rutile		FG rutile	
ppm	**D.L.**	**Ave (n = 20)**	**Stdev**	**Ave (n = 23)**	**Stdev**	**Ave (n = 15)**	**Stdev**	**Ave (n = 5)**	**Stdev**
^{24}Mg	0.061	2668	3390	4180	4674	864	1172	17446	813
^{27}Al	0.269	2986	3571	11521	15380	4854	12068	30976	1257
^{29}Si	191.91	12260	11627	15983	33406	5843	11259	41780	10303
^{43}Ca	70.91	6713	7103	7268	13298	44454	71209	20140	15160
^{45}Sc	0.048	37.9	11.6	7.24	5.01	107	25	106	37
^{51}V	0.034	1850	330	3609	575	3829	664	2702	652
^{52}Cr	0.499	141	60	1134	2682	354	182	344	67
^{55}Mn	0.523	14440	967	7690	4009	1145	1738	481	377
^{59}Co	0.002	19.1	3.3	31.6	6.3	0.17	0.21	4.97	0.68
^{60}Ni	0.076	8.54	5.78	64.0	13.3	0.34	0.58	14.6	3.7
^{65}Cu	0.031	4.04	2.04	34.5	16.0	3.85	0.41	6.29	3.77
^{66}Zn	0.120	312	357	1597	2177	4.97	3.31	133	9
^{75}As	0.372	0.20	0.17	4.89	4.73	0.95	0.90	6.88	2.20
^{89}Y	0.0003	12.5	10.5	10.6	13.3	12.6	7.7	118	19
^{91}Zr	0.003	977	375	370	518	864	452	1507	627
^{93}Nb	0.0002	91.4	46.8	91.1	38.7	165	75	198	68
^{95}Mo	0.004	0.93	0.59	3.31	2.16	0.50	0.37	2.02	0.91
^{118}Sn	0.030	1.85	0.89	5.05	1.73	1.17	0.70	33.8	13.4
^{121}Sb	0.022	0.51	0.65	3.01	2.72	111	154	214	33
^{178}Hf	0.0005	12.6	5.5	6.70	5.29	16.6	8.6	28.1	10.5
^{181}Ta	0.00002	5.50	2.14	3.06	2.01	9.89	3.30	9.39	1.78
^{182}W	0.001	0.29	0.37	0.15	0.13	7.32	4.90	33.9	7.3
^{208}Pb	0.004	0.57	0.60	13.2	13.3	1.88	1.19	5.91	6.54
^{232}Th	0.0001	0.45	0.95	0.11	0.23	0.45	0.36	2.70	1.19
^{238}U	0.0001	0.24	0.26	0.10	0.11	0.17	0.09	1.03	0.37

Abbreviations: D.L., detection limit; Ave, average; Stdev, standard deviation

Table 3
Whole-rock composition of selected samples of dolerite and country slate from the Semnon Sb-Au deposit

	Least altered composition	Most altered composition	Gain/loss relative to C_{SEM2}
	SEM2	**SEM12**	**Δ C_{SEM12}/C_{SEM2}**
SiO_2 (%)	46.74	43.00	0.021
Al_2O_3	14.13	13.00	0.021
Fe_2O_3	15.80	14.08	-0.011
MnO	0.18	0.18	0.064
MgO	5.48	5.40	0.094
CaO	3.38	8.02	1.632
Na_2O	2.45	1.20	-0.455
K_2O	0.04	0.27	5.684
TiO_2	3.53	2.96	-0.070
P_2O_5	0.68	0.64	0.044
LOI	7.29	11.48	0.748
Total	99.71	100.22	-
As (ppm)	3.28	19.53	5.616
Ba	72.02	101.30	0.561
Co	41.89	36.50	-0.033
Cr	80.74	81.19	0.116
Cs	1.07	3.14	2.268
Cu	25.71	21.77	-0.060
Hf	8.63	7.57	-0.027
Mo	1.39	1.59	0.265
Nb	26.43	23.36	-0.019
Ni	38.22	33.89	-0.016
Rb	2.44	17.58	7.002
Sc	34.93	31.27	-0.007
Sb	37.04	33.40	0.001
Sn	1.62	1.64	0.128
Sr	137.10	232.80	0.884
Ta	1.91	1.66	-0.038
Th	3.87	3.32	-0.048
U	0.71	0.62	-0.032
V	235.00	207.60	-0.020
W	2.67	2.21	-0.082
Y	50.67	45.85	0.004
Zn	166.00	150.70	0.007
Zr	338.10	298.40	-0.021
La	29.77	26.50	-0.012
Ce	64.35	57.93	-0.001
Nd	40.36	36.24	-0.004
Sm	9.93	8.80	-0.017
Yb	4.70	4.21	-0.005

$\Delta\ C_i^A/C_i^0 = (M^A/M^0)(C_i^A/C_i^0)-1$ where M^A/M^0 is the inverse of the slope of the isocon straight line. Slope $_{SEM2/SEM12}$ = 0.9011

Table 4
Calculated hydrothermal rutile trace elements concentrations using the average measured trace elements concentrations of precursor minerals

	Precursor minerals		**Hydrothermal CG rutile**	
ppm	Ilmenite (Ave)	Titanohematite (Ave)	Measured (Ave)	Calculated (Ave)
^{55}Mn	14440	7690	1145	30091
^{51}V	1850	3609	3829	4011
^{52}Cr	141	1134	354	357
^{59}Co	19	31.6	0.17	41.02
^{60}Ni	8.54	64.0	0.34	21.31
^{65}Cu	0.80	34.5	3.85	3.68
^{66}Zn	312	1597	4.97	734.27
^{75}As	0.20	4.89	0.95	0.71
^{45}Sc	38	7.24	107	78.12
^{118}Sn	1.85	5.05	1.17	4.09
^{95}Mo	0.93	3.31	0.50	2.10
^{121}Sb	0.51	3.01	111	1.22
^{182}W	0.29	0.15	7.32	0.61
^{91}Zr	895	370	864	1860
^{178}Hf	13	6.70	16.6	26.27
^{93}Nb	91	91	165	193
^{181}Ta	5.50	3.06	9.89	11.47
^{208}Pb	0.57	13.2	1.88	1.94
^{238}U	0.24	0.10	0.17	0.50

Abbreviations: Ave, average. See text for explanation and method

Table A.2 Operating conditions for the laser ablation ICP-MS analysis of Fe-Ti oxides and pyrite

Laser ablation system	RESOlution (ASI) 193nm excimer laser with a S155 ablation cell	
ICP-MS	Agilent 7900	
Laser frequency	17 Hz	
Fluence	3 J/cm² (Fe-Ti oxides) and 2 J/cm² (pyrite)	
Beam size	25-55 µm	
Dwell time	10ms/peak	
Sampling mode	Single spot	
Background collection	30 s	
Ablation duration	60 s	
Wash-out delay	15 s	
Gas flow	Helium (350 mL/min) Argon (0.9-1.1 mL/min) Nitrogen (2 mL/min)	
Calibration	**Fe-Ti oxides**	**Pyrite**
Internal Standard	Fe for ilmenite and titanohematite, and Ti for rutile (data from EPMA)	Fe (data from EPMA)
Reference material	GSE-1G (USGS-synthetic glass)	MASS-1 (USGS-sulfide pressed powder pellet) for Co, Ni, Cu, Zn, Ge, As, Se, Mo, Ag, Cd, In, Sn, Sb, Te, W, Tl, Pb, Bi po-727 (synthetic FeS) for PGE and Au
Monitoring	GSD-1G (USGS-synthetic glass) Gprob6 (USGS-matrix artificial basalt glass) natural magnetite BC28 (in-house monitor)	synthetic FeS JB-MSS5 (in-house monitor)
Monitor signal for inclusions	S, Si and Ca	Si, Ca and Ti
Data reduction	Iolite software (IGOR Pro 6.3)	

Table A.3 LA-ICP-MS analyses of reference material used for calibration and to monitor the data quality of ilmenite and titanohematite

Isotope	Calibration			Monitor (reference material)								In-house reference material for monitoring the data quality			
				GSD-1g (synthetic basalt glass)				Gprob6 (matrix artificial basalt glass)				BC28 (natural Ti-rich magnetite from the Bushveld Complex)			
	Reference Material	Certificate value		Certificate value		**This study**		Working value		**This study**		Working value		**This study**	
		Ave	Stdev	Ave	Stdev	Ave (n=20)	Stdev	Ave	Stdev	Ave (n=4)	Stdev	Ave		Ave (n=20)	Stdev
^{24}Mg	GSE-1g	21106	181	21709	241	**22280**	430.14	51318	6935	**47538**	923	11618	INAA	**12412**	2071
^{25}Mg	GSE-1g	21106	181	21709	241	**22350**	481.01	51318	6935	**48710**	1383	11618	INAA	**12176**	2243
^{27}Al	GSE-1g	68804	2117	70922	1588	**71915**	2185.93	92145	12438	**81198**	2810	20787	INAA	**22300**	4293
^{29}Si	GSE-1g	250994	7011	248657	3739	**254590**	6465.61	224259	9418	**213575**	5811	220	EPMA	**668**	952.71
^{31}P	GSD-1g	70	20	860	160	Used in calibration		611	131	**509**	11	N.A.	N.A.	**bdl**	
^{44}Ca	GSE-1g	52858	2143	51429	714	**51283**	1994.40	86787	4643	**78008**	2637	<24	EPMA	**bdl**	
^{43}Ca	GSE-1g	52858	2143	51429	714	**52337**	2163.76	86787	4643	**80080**	1743	<24	EPMA	**bdl**	
^{45}Sc	GSE-1g	52	2	52	2	**48**	1.89	36.75	2.59	**31.95**	1.40	31	INAA	**26**	3
^{47}Ti	GSE-1g	450	42	7432	360	**8990**	755.52	7012	1319	**7144**	720	87615	INAA	**96739**	5134
^{49}Ti	GSE-1g	450	42	7432	360	**8984**	751.67	7012	1319	**7043**	654	87615	INAA	**97055**	5559
^{51}V	GSE-1g	440	20	44	2	**40**	2.94	238	27.1	**222**	10	9603	INAA	**9651**	716
^{52}Cr	GSE-1g	400	80	42	3	**40**	2.78	300	21.5	**319**	5	1172	INAA	**1363**	50
^{53}Cr	GSE-1g	400	80	42	3	**45**	0.71	300	21.5	**322**	7	1172	INAA	**1338**	69
^{55}Mn	GSE-1g	590	20	220	20	**216**	6.66	1255	93	**1264**	41	2125	INAA	**2159**	178
^{59}Co	GSE-1g	380	20	40	2	**36**	2.33	47	3.51	**43**	2.9 2	241	INAA	**260**	22.42
^{60}Ni	GSE-1g	58	4	58	4	**58**	1.32	146	18.9	**152**	5.0 9	573	INAA	**529**	40.36
^{63}Cu	GSE-1g	380	40	42	2	**40**	2.24	90	20.31	**71**	4.6 4	33	INAA	**11**	13.56
^{65}Cu	GSE-1g	380	40	42	2	**42**	1.14	90	20.31	**76**	5.3 0	33	INAA	**13**	14.76
^{66}Zn	GSE-1g	460	10	54	2	**52**	1.17	71	16.6	**74**	5.5 2	588	INAA	**560**	116.69
^{71}Ga	GSE-1g	490	70	54	7	**47**	2.63	16	2	**13**	0.3 7	41.1	LA (MASS-1)	**38**	1.80
^{72}Ge	GSE-1g	320	80	32	8	**32**	0.78	1.26	0.41	**1.27**	0.0 7	0.86	LA (MASS-1)	**1.59**	0.28
^{74}Ge	GSE-1g	320	80	32	8	**32**	0.79	1.26	0.41	**1.10**	0.0 3	0.86	LA (MASS-1)	**1.08**	0.16
^{75}As	GSE-1g	260	90	27	8	**26**	1.58	N.A.		**1.83**	0.0 6	N.A.	N.A.	**0.25**	0.68
^{88}Sr	GSE-1g	447	5	69	1	**62**	3.24	167	26.1	**138**	4.8 4	N.A.	N.A.	**0.22**	0.28
^{89}Y	GSE-1g	42	2	42	2	**36**	1.09	19	1.78	**15**	0.3 5	0.08	LA (BCR2g)	**0.04**	0.08
^{90}Zr	GSE-1g	42	2	42	2	**37**	1.83	55	2.4	**42**	1.8 7	27.50	LA (BCR2g)	**19.87**	3.87
^{91}Zr	GSE-1g	42	2	42	2	**43**	1.40	55	2.4	**48**	2.0 0	27.50	LA (BCR2g)	**23.08**	3.20
^{93}Nb	GSE-1g	42	3	42	3	**37**	1.85	4.16	0.41	**3.02**	0.1 8	1.72	LA (BCR2g)	**1.40**	0.13
^{95}Mo	GSE-1g	390	30	39	3	**39**	1.07	N.A.		**0.36**	0.0 4	0.76	LA (NIST361)	**0.39**	0.04
^{118}Sn	GSE-1g	29	6	29	6	**27**	0.73	1.33	0.71	**0.99**	0.1 0	2.20	LA (MASS-1)	**1.27**	0.15
^{121}Sb	GSE-1g	450	110	43	7	**40**	2.31	0.13	0.01	**0.12**	0.0 1	0.02	INAA	**0.02**	0.01
^{178}Hf	GSE-1g	395	7	39	2	**34**	1.30	1.52	0.15	**1.15**	0.0 4	0.58	INAA	**0.76**	0.11
^{181}Ta	GSE-1g	390	40	40	4	**34**	0.49	0.28	0.03	**0.18**	0.0 0	0.07	INAA	**0.12**	0.01
^{182}W	GSE-1g	430	50	43	4	**38**	2.18	N.A.		**0.22**	0.0 2	0.51	LA (NIST361)	**0.01**	0.01
^{208}Pb	GSE-1g	378	12	50	2	**43**	2.91	3.28	0.78	**3.05**	0.1 7	1.98	LA (MASS-1)	**0.05**	0.06

Abbreviations: Ave, average; Stdev, standard deviation; bdl, below detection limit; N.A., not analyzed

The internal standard used is the ^{57}Fe with the following values : 9.8 wt.% (GSE-1g), 10.3 wt.% (GSD-1g), 7.3 wt.% (Gprob6) and 57.2 wt.% (BC28)

Working values for BC28 are taken from Dare et al. (2012). INAA data have been recalculated to 100 % magnetite with a factor of 1.07 from values of Barnes et al. (2004)

Table A.4 LA-ICP-MS analyses of reference material used for calibration and to monitor the data quality of rutile

Isotope	Calibration			Monitor (reference material)								In-house reference material for monitoring the dat		
				GSD-1g (synthetic basalt glass)				Gprob6 (matrix artificial basalt glass)				BC28 (natural Ti-rich magnetite from the Bushvel		
	Reference Material	Certificate value		Certificate value		This study		Working value		This study		Working value	This study	
		Ave	Stdev	Ave	Stdev	Ave (n=20)	Stdev	Ave	Stdev	Ave (n=4)	Stdev	Ave		Ave (n=20)
^{24}Mg	GSE-1g	21106	181	21709	241	**18477**	1532	51318	6935	**46843**	4089	11618	INAA	**11197**
^{25}Mg	GSE-1g	21106	181	21709	241	**18534**	1647	51318	6935	**48213**	6609	11618	INAA	**10988**
^{27}Al	GSE-1g	68804	2117	70922	1588	**59505**	3623	92145	12438	**79960**	5720	20787	INAA	**19519**
^{29}Si	GSE-1g	250994	7011	248657	3739	**211350**	17694	224259	9418	**211075**	18764	220	EPMA	**419**
^{44}Ca	GSE-1g	52858	2143	51429	714	**42385**	2315	86787	4643	**76903**	5804	<24	EPMA	**bdl**
^{43}Ca	GSE-1g	52858	2143	51429	714	**43262**	2691	86787	4643	**78928**	6768	<24	EPMA	**bdl**
^{45}Sc	GSE-1g	52	2	52	2	**40**	5	37	2.59	**32**	5	31	INAA	**23**
^{51}V	GSE-1g	440	20	44	2	**34**	5	238	27.1	**219**	32	9603	INAA	**8731**
^{52}Cr	GSE-1g	400	80	42	3	**34**	5	300	21.5	**314**	31	1172	INAA	**1235**
^{53}Cr	GSE-1g	400	80	42	3	**37**	3	300	21.5	**318**	32	1172	INAA	**1212**
^{55}Mn	GSE-1g	590	20	220	20	**179**	21	1255	93	**1250**	174	2125	INAA	**1956**
^{56}Fe	GSE-1g	98717	2332	103381	777	**85708**	7750	72598	13310	**71935**	7930	571806	INAA	**525165**
^{57}Fe	GSE-1g	98717	2332	103381	777	**85807**	7708	72598	13310	**71915**	8013	571806	INAA	**526305**
^{59}Co	GSE-1g	380	20	40	2	**30**	5	47	3.51	**42**	8	241	INAA	**235**
^{60}Ni	GSE-1g	58	4	58	4	**48**	4	146	18.9	**150**	12	573	INAA	**585**
^{63}Cu	GSE-1g	380	40	42	2	**33**	4	90	20.31	**70**	9	33	INAA	**10**
^{65}Cu	GSE-1g	380	40	42	2	**35**	3	90	20.31	**75**	6	33	INAA	**12**
^{66}Zn	GSE-1g	460	10	54	2	**43**	3	71	16.6	**73**	5	588	INAA	**506**
^{71}Ga	GSE-1g	490	70	54	7	**39**	6	16	2	**13**	2	41.088	LA (MASS-1)	**34**
^{72}Ge	GSE-1g	320	80	32	8	**26**	2	1.3	0.41	**1.3**	0	0.856	LA (MASS-1)	**1.45**
^{74}Ge	GSE-1g	320	80	32	8	**26**	2	1.3	0.41	**1.1**	0.11	0.856	LA (MASS-1)	**0.98**
^{75}As	GSE-1g	260	90	27	8	**22**	2	N.A.		**1.8**	0	N.A.	N.A.	**0.21**
^{88}Sr	GSE-1g	447	5	69	1	**52**	7	167	26.1	**136**	20	N.A.	N.A.	**0.21**
^{89}Y	GSE-1g	42	2	42	2	**30**	3	19	1.78	**14**	2	0.08	LA (BCR2g)	**0.07**
^{90}Zr	GSE-1g	42	2	42	2	**31**	4	55	2.4	**41**	6	27.50	LA (BCR2g)	**18**
^{91}Zr	GSE-1g	42	2	42	2	**35**	2	55	2.4	**47**	3	27.50	LA (BCR2g)	**20.9175**
^{93}Nb	GSE-1g	42	3	42	3	**31**	4	4.16	0.41	**3.01**	0.53	1.72	LA (BCR2g)	**1.76**
^{95}Mo	GSE-1g	390	30	39	3	**32**	3	N.A.		**0.36**	0.06	0.76	LA (NIST361)	**0.35**
^{118}Sn	GSE-1g	29	6	29	6	**22**	2	1.33	0.71	**0.99**	0.16	2.20	LA (MASS-1)	**1.52**
^{121}Sb	GSE-1g	450	110	43	7	**33**	5	0.13	0.01	**0.12**	0.02	0.02	INAA	**0.02**
^{178}Hf	GSE-1g	395	7	39	2	**29**	4	1.52	0.15	**1.14**	0.17	0.58	INAA	**0.69**
^{181}Ta	GSE-1g	390	40	40	4	**28**	2	0.28	0.03	**0.18**	0.02	0.07	INAA	**0.11**
^{182}W	GSE-1g	430	50	43	4	**32**	5	N.A.		**0.22**	0.03	0.51	LA (NIST361)	**0.01**
^{208}Pb	GSE-1g	378	12	50	2	**36**	6	3.28	0.78	**3.04**	0.50	1.98	LA (MASS-1)	**0.05**

Abbreviations: Ave, average; Stdev, standard deviation; bdl, below detection limit; N.A., not analyzed

The internal standard used is the 47 Ti with the following values : 450 ppm (GSE-1g), 0.7 wt.% (GSD-1g), 0.7 wt.% (Gprob6) and 8.8 wt.% (BC28)

Working values for BC28 are taken from Dare et al. (2012). INAA data have been recalculated to 100 % magnetite with a factor of 1.07 from values of Barnes et al. (2004)

Table A.5 LA-ICP-MS analyses of reference material used for calibration and to monitor the data quality of pyrite

Isotope	Calibration			Monitor (reference material)				In-house reference material			
				GSE-1g (synthetic basalt glass)				JB-MSS5 (synthetic FeS)			
	Reference Material	Certificate value		Certificate value		This study		Working value		This study	
		Ave	Stdev	Ave	Stdev	Ave (n=7)	Stdev	Ave	Stdev	Ave (n=7)	Stdev
^{34}S	po-727	390900	1600					404700		**394014**	18584
^{59}Co	MASS-1	60	10	380	20	**397**	28	0.28	0.02	**0.02**	0.002
^{60}Ni	MASS-1	440	30	440	30	**461**	21	10487	N.D.	**11768**	558
^{62}Ni	MASS-1	440	30	440	30	**422**	37	10487	N.D.	**12117**	354
^{63}Cu	MASS-1	134000	500	380	40	**421**	21	208	24	**190**	11
^{65}Cu	MASS-1	134000	500	380	40	**378**	17	208	24	**173**	8.11
^{66}Zn	MASS-1	210000	5000	460	10	**383**	13	N.A.		**2.47**	1.15
^{72}Ge	MASS-1	50	N.D.	320	80	**363**	21	N.A.		**0.63**	0.09
^{74}Ge	MASS-1	50	N.D.	320	80	**369**	16	N.A.		**0.55**	0.06
^{75}As	MASS-1	65	3	260	90	**315**	16	79	11	**55**	3.71
^{78}Se	MASS-1	51	4	20	16	**19**	11	47.27	13.39	**56**	6.02
^{95}Mo	MASS-1	59	9	390	30	**412**	26	0.23	0.02	**0.33**	0.02
^{100}Ru	po-727	36.5	0.3	N.A.		**361**	22	21.68	2.31	**22.08**	1.06
^{101}Ru	po-727	36.5	0.3	N.A.		**0**	0	21.68	2.31	**21.39**	1.09
^{103}Rh	po-727	41.6	0.3	N.A.		**70**	20	61.4	7.2	**72.86**	3.72
^{105}Pd	po-727	43.4	0.3	N.A.		**154**	22	65.2	5.1	**57.92**	5.31
^{106}Pd	po-727	43.4	0.3	N.A.		**163**	22	65.2	5.1	**58.35**	5.13

^{107}Ag	MASS-1	50	5	200	20	**220**	18	53	4.9	**46.73**	3.66
^{108}Pd	po-727	43.4	0.3	N.A.		**155**	18	65.2	5.1	**58.36**	4.92
^{111}Cd	MASS-1	60	7	160	50	**182**	20	0.13	0.04	**0.10**	0.03
^{113}Cd	MASS-1	60	7	160	50	**253**	22	0.13	0.04	**0.06**	0.01
^{115}In	MASS-1	50	N.D.	370	60	**377**	29	N.A.		**bdl**	
^{118}Sn	MASS-1	59	6	280	50	**404**	18	0.34	0.03	**0.05**	0.02
^{121}Sb	MASS-1	60	9	450	110	**403**	13	61.3	7.3	**49.47**	2.51
^{125}Te	MASS-1	15	N.D.	N.A.		**189**	9	44	3	**26.82**	1.70
^{182}W	MASS-1	20	2	430	50	**472**	23	N.A.		**0.02**	0.003
^{185}Re	GSE	120	N.D.	Used in calibration				20.7	N.D.	**30.62**	3.59
^{189}Os	po-727	46.7	2.6	N.A.		**bdl**		42.58	0.93	**53.62**	2.78
^{190}Os	po-727	46.7	2.6	N.A.		**bdl**		42.58	0.93	**53.76**	2.96
^{191}Ir	po-727	48	1.2	120		**52**	19	40.21	0.53	**40.27**	2.11
^{193}Ir	po-727	48	1.2	120		**51**	18	40.21	0.53	**40.72**	2.98
^{194}Pt	po-727	35.5	0.8	30		**33**	11	39.9	1	**40.58**	3.99
^{195}Pt	po-727	35.5	0.8	30		**33**	12	39.9	1	**40.56**	4.20
^{197}Au	po-727	45.8	2.4	7		**8**	1	35.9	4.8	**35.00**	3.54
^{205}Tl	MASS-1	50	N.D.	2		**1**	0	N.A.		**bdl**	
^{208}Pb	MASS-1	68	7	378	12	**407**	33	71.5	4.5	**62.41**	4.34
^{209}Bi	MASS-1	60	N.D.	320	30	**307**	16	76.1	2.9	**64.63**	3.38

Abbreviations: Ave, average; Stdev, standard deviation; bdl, below detection limit; N.A., not analyzed; N.D., not determined
The internal standard used is the ^{57} Fe with the following values : 9.8 wt.% (GSE-1g), 15.6 wt.% (MASS-1), 61 wt.% (LAF po-727) and 57 wt.% (JB-MSS5)

Table A.6 Electron microprobe analyses of Fe-Ti oxides from gabbros of the Semnon Sb-Au deposit

Wt. Oxides %	SiO2	Al2O3	TiO2	V2O3	Cr2O3	FeO	Fe2O3	MnO	MgO	CaO	Total	**A.p.f.u.**	Si	Al	Ti	V	Cr	Fe 3+	Fe 2+	Mn	Mg	C
Ilmenite																						
D.L.	0.01	0.01	0.02	0.27	0.04	0.17	0.13	0.01	0.01	-												
MF1 c4-1	0.04	0.02	49.54	0.15	0.02	42.80	4.91	1.61	0.05	-	99.22		0.00	0.00	1.90	0.01	0.00	0.19	1.82	0.07	0.00	-
MF1 c4-2	0.02	bdl	49.11	0.42	bdl	42.22	7.01	1.73	0.05	-	100.66		0.00	-	1.86	0.02	-	0.27	1.78	0.07	0.00	-
MF1 c4-3	0.02	0.05	49.68	0.40	0.02	42.59	4.85	2.01	0.02	-	99.66		0.00	0.00	1.90	0.02	0.00	0.19	1.81	0.09	0.00	-
MF1 c3-1	0.06	0.17	49.33	0.55	0.04	42.42	5.49	1.72	0.09	-	99.99		0.00	0.01	1.88	0.02	0.00	0.21	1.79	0.07	0.01	-
MF1 c3-2	0.02	0.16	50.13	0.15	0.09	43.07	4.84	1.80	0.07	-	100.40		0.00	0.01	1.90	0.01	0.00	0.18	1.81	0.08	0.01	-
MF1 c3-3	0.02	0.03	49.41	0.37	0.01	42.72	5.89	1.62	0.06	-	100.12		0.00	0.00	1.88	0.01	0.00	0.22	1.81	0.07	0.00	-
MF1 c3-4	0.01	0.03	49.12	0.35	0.06	42.08	6.03	2.03	0.03	-	99.78		0.00	0.00	1.87	0.01	0.00	0.23	1.79	0.09	0.00	-
MF1 c3-5	bdl	0.14	49.10	0.14	0.06	42.38	5.81	1.69	0.04	-	99.43		-	0.01	1.88	0.01	0.00	0.22	1.80	0.07	0.00	-
MF1 c3-6	0.00	bdl	49.44	0.35	0.03	42.59	5.07	1.74	0.03	-	99.37		0.00	0.00	1.89	0.01	0.00	0.19	1.81	0.08	0.00	-
MF1 c3-7	0.05	0.03	49.59	0.35	0.01	42.75	5.21	1.70	0.04	-	99.77		0.00	0.00	1.89	0.01	0.00	0.20	1.81	0.07	0.00	-
MF1 c2-1	0.05	0.01	48.13	0.79	0.05	41.38	7.89	1.74	0.05	-	100.15		0.00	0.00	1.83	0.03	0.00	0.30	1.75	0.07	0.00	-
MF1 c2-2	0.01	0.18	48.47	0.27	0.03	41.56	7.13	1.82	0.06	-	99.60		0.00	0.01	1.85	0.01	0.00	0.27	1.77	0.08	0.00	-
MF1 c2-3	0.02	0.04	49.55	0.50	0.01	42.37	5.47	1.78	0.05	-	99.90		0.00	0.00	1.89	0.02	0.00	0.21	1.79	0.08	0.00	-
MF1 c2-4	0.03	0.10	50.18	0.12	bdl	43.06	4.65	1.62	0.08	-	99.96		0.00	0.01	1.91	0.00	-	0.18	1.82	0.07	0.01	-
MF1 c2-5	0.03	0.10	48.66	0.42	bdl	41.43	6.97	2.05	0.05	-	99.76		0.00	0.01	1.86	0.02	-	0.27	1.76	0.09	0.00	-
MF1 c2-6	0.01	0.04	48.63	0.54	0.06	41.76	6.68	1.74	0.07	-	99.54		0.00	0.00	1.86	0.02	0.00	0.26	1.78	0.07	0.01	-
MF1 c1-1	0.06	bdl	49.13	0.16	0.01	42.23	7.01	1.80	0.05	-	100.58		0.00	-	1.86	0.01	0.00	0.27	1.78	0.08	0.00	-
MF1 c1-2	0.02	bdl	49.19	0.40	0.02	42.26	6.20	1.77	0.05	-	99.94		0.00	0.00	1.87	0.02	0.00	0.24	1.79	0.08	0.00	-
MF1 c1-3	0.00	0.04	49.01	0.24	bdl	42.13	6.20	1.84	0.04	-	99.53		0.00	0.00	1.88	0.01	-	0.24	1.79	0.08	0.00	-
MF1 c1-4	0.05	0.02	49.41	0.10	0.02	42.62	5.48	1.78	0.05	-	99.53		0.00	0.00	1.89	0.00	0.00	0.21	1.81	0.08	0.00	-
MF1 c1-5	0.01	0.09	49.01	0.40	0.10	42.22	6.76	1.67	0.08	-	100.35		0.00	0.01	1.86	0.02	0.00	0.26	1.78	0.07	0.01	-
BAN1 c1-3	0.01	0.00	50.11	0.06	bdl	41.08	4.34	3.83	0.05	-	99.50		0.00	0.00	1.92	0.00	-	0.17	1.75	0.16	0.00	-
BAN1 c2-7	0.02	0.06	48.92	0.14	0.03	40.68	6.32	3.01	0.11	-	99.31		0.00	0.00	1.87	0.01	0.00	0.24	1.73	0.13	0.01	-
BAN1 c2-8	bdl	bdl	48.54	0.23	bdl	40.54	7.52	2.76	0.09	-	99.84		-	0.00	1.85	0.01	-	0.29	1.72	0.12	0.01	-
BAN1 c3-5	0.01	0.01	48.81	0.11	0.01	39.40	7.13	4.15	0.12	-	99.87		0.00	0.00	1.86	0.00	0.00	0.27	1.67	0.18	0.01	-
Average	0.02	0.07	49.21	0.31	0.04	42.01	6.03	2.04	0.06	-	99.83		0.00	0.00	1.88	0.01	0.00	0.23	1.78	0.09	0.00	-
Stdev	0.02	0.06	0.52	0.18	0.03	0.87	0.99	0.67	0.02	-	0.39		0.00	0.00	0.02	0.01	0.00	0.04	0.04	0.03	0.00	-
Titanohematite																						
D.L.	0.01	0.01	0.02	0.27	0.04	0.17	0.13	0.01	0.01	-												
TOU1 c1-1	0.11	0.93	21.65	0.50	bdl	17.42	56.95	1.81	0.03	-	99.47		0.01	0.06	0.85	0.02	0.00	2.23	0.76	0.08	0.00	-
TOU1 c1-2	0.10	0.14	22.88	0.61	0.24	20.31	54.25	0.29	bdl	-	98.85		0.01	0.01	0.90	0.03	0.01	2.14	0.89	0.01	-	-
TOU1 c1-3	0.09	0.08	16.71	0.52	0.04	13.44	68.18	1.53	0.02	-	100.66		0.00	0.00	0.65	0.02	0.00	2.66	0.58	0.07	0.00	-
TOU1 c1-4	0.07	1.03	22.16	0.76	0.77	16.95	55.39	2.78	0.02	-	100.01		0.00	0.06	0.86	0.03	0.03	2.15	0.73	0.12	0.00	-
TOU1 c2-1	0.10	0.50	18.36	0.67	0.41	15.69	63.93	0.83	0.01	-	100.53		0.01	0.03	0.71	0.03	0.02	2.49	0.68	0.04	0.00	-
TOU1 c2-3	0.12	0.80	22.09	0.54	0.05	18.82	56.33	1.07	0.02	-	99.92		0.01	0.05	0.86	0.02	0.00	2.19	0.81	0.05	0.00	-
TOU1 c2-4	0.14	0.26	18.57	0.62	0.36	15.87	63.38	0.93	bdl	-	100.17		0.01	0.02	0.73	0.03	0.01	2.48	0.69	0.04	0.00	-
TOU1 c3-1	0.08	0.09	19.16	0.91	0.36	16.42	62.94	0.53	0.03	-	100.71		0.00	0.01	0.75	0.04	0.01	2.45	0.71	0.02	0.00	-
TOU1 c3-3	1.10	0.36	16.36	0.47	0.36	14.57	65.31	1.04	0.22	-	99.81		0.06	0.02	0.64	0.02	0.01	2.55	0.63	0.05	0.02	-
TOU1 c3-4	0.10	0.20	21.72	0.56	0.05	19.12	56.86	0.37	0.04	-	99.08		0.00	0.01	0.86	0.02	0.00	2.24	0.84	0.02	0.00	-
TOU1 c3-5	0.09	1.40	22.14	0.46	0.23	18.04	55.70	1.67	0.03	-	99.82		0.00	0.08	0.86	0.02	0.01	2.16	0.78	0.07	0.00	-
BAN1 c1-1	0.10	0.06	18.84	0.79	bdl	16.21	64.49	0.83	bdl	-	101.39		0.01	0.00	0.73	0.03	0.00	2.49	0.70	0.04	0.00	-
BAN1 c1-2	0.08	0.07	20.99	0.56	bdl	18.08	59.42	0.79	0.02	-	100.12		0.00	0.00	0.82	0.02	0.00	2.32	0.79	0.03	0.00	-
BAN1 c1-5	0.06	0.09	15.08	0.48	bdl	12.39	72.35	1.01	0.06	-	101.66		0.00	0.01	0.58	0.02	0.00	2.80	0.53	0.04	0.00	-
BAN1 c1-6	0.11	0.09	20.20	0.34	bdl	17.20	61.53	0.91	0.04	-	100.55		0.01	0.01	0.79	0.01	-	2.40	0.74	0.04	0.00	-
BAN1 c1-7	0.10	0.15	19.07	0.74	bdl	15.71	64.65	1.38	0.02	-	101.87		0.01	0.01	0.73	0.03	-	2.49	0.67	0.06	0.00	-
BAN1 c1-8	0.09	bdl	17.93	0.33	bdl	15.33	67.21	0.85	0.02	-	101.76		0.00	-	0.69	0.01	-	2.59	0.66	0.04	0.00	-
BAN1 c2-1	0.10	0.03	20.24	0.54	bdl	17.01	62.15	1.22	0.02	-	101.34		0.01	0.00	0.78	0.02	0.00	2.40	0.73	0.05	0.00	-
BAN1 c2-2	0.12	bdl	19.82	0.98	bdl	16.33	62.44	1.45	bdl	-	101.22		0.01	-	0.77	0.04	0.00	2.42	0.70	0.06	0.00	-
BAN1 c2-3	0.10	0.18	19.85	0.63	bdl	16.85	61.98	1.06	0.02	-	100.71		0.01	0.01	0.77	0.03	0.00	2.41	0.73	0.05	0.00	-
BAN1 c2-4	0.09	0.40	19.19	0.49	0.05	16.40	63.89	0.63	0.02	-	101.30		0.00	0.02	0.74	0.02	0.00	2.47	0.70	0.03	0.00	-
BAN1 c2-5	0.10	0.13	21.68	0.45	bdl	19.37	57.51	0.20	bdl	-	99.50		0.01	0.01	0.85	0.02	0.00	2.26	0.85	0.01	0.00	-
BAN1 c2-6	0.08	0.79	22.47	0.63	bdl	19.96	56.64	0.24	0.02	-	100.93		0.00	0.05	0.87	0.03	0.00	2.18	0.86	0.01	0.00	-
BAN1 c3-2	0.09	0.72	20.52	0.31	bdl	17.47	60.85	0.93	0.03	-	100.96		0.00	0.04	0.79	0.01	0.00	2.35	0.75	0.04	0.00	-
BAN1 c3-3	0.12	0.08	21.37	0.39	bdl	18.26	60.04	0.79	0.03	-	101.27		0.01	0.00	0.83	0.02	0.00	2.32	0.78	0.03	0.00	-
BAN1 c3-4	0.08	0.07	20.39	bdl	bdl	17.25	61.12	1.00	0.01	-	100.13		0.00	0.00	0.80	0.01	0.00	2.39	0.75	0.04	0.00	-
Average	0.13	0.36	19.98	0.57	0.27	16.94	61.37	1.01	0.03	-	100.53		0.01	0.02	0.78	0.02	0.01	2.39	0.73	0.04	0.00	-
Stdev	0.20	0.38	2.01	0.20	0.19	1.86	4.41	0.55	0.04	-	0.83		0.01	0.02	0.08	0.01	0.01	0.17	0.08	0.02	0.00	-
CG rutile																						
D.L.	0.04	0.04	0.05	0.01	0.01	0.08	0.08	0.03	0.03	0.02												
SEM9-c1-1	0.09	0.13	99.31	0.74	0.01	-	0.28	bdl	bdl	bdl	101.16		0.00	0.00	1.97	0.02	0.00	0.01	-	-	-	-
SEM9-c1-2	0.14	0.09	99.30	0.81	0.03	-	0.21	bdl	bdl	0.07	100.70		0.00	0.00	1.97	0.02	0.00	0.00	-	-	-	0
SEM9-c1-3	0.16	0.07	99.27	0.71	0.03	-	0.12	bdl	bdl	0.08	100.46		0.00	0.00	1.97	0.02	0.00	0.00	-	-	-	0
SEM9-c1-4	0.08	bdl	100.03	0.57	bdl	-	0.20	bdl	bdl	0.30	101.24		0.00	-	1.97	0.01	-	0.00	-	-	-	0
SEM9-c1-5	0.08	bdl	99.05	0.79	0.03	-	0.25	bdl	bdl	0.19	100.44		0.00	-	1.97	0.02	0.00	0.00	-	-	-	0
SEM9-c1-6	bdl	bdl	99.68	0.80	0.02	-	0.00	bdl	bdl	0.14	100.63		-	-	1.98	0.02	0.00	-	-	-	-	0
SEM9-c1-7	0.12	bdl	98.69	0.73	bdl	-	0.12	bdl	bdl	0.15	99.84		0.00	-	1.97	0.02	-	0.00	-	-	-	0
SEM9-c2-1	bdl	bdl	99.71	0.74	0.06	-	0.20	bdl	bdl	bdl	100.98		-	-	1.98	0.02	0.00	0.00	-	-	-	-

SEM9-c2-2	bdl	bdl	100.12	0.81	0.04	-	0.20	bdl	bdl	bdl	101.22	-	-	1.98	0.02	0.00	0.00	-	-	-	-
SEM9-c2-3	0.13	0.07	99.62	0.81	0.07	-	0.14	bdl	bdl	0.06	101.09	0.00	0.00	1.97	0.02	0.00	0.00	-	-	-	0
SEM9-c2-4	bdl	0.08	99.25	0.70	bdl	-	0.20	bdl	bdl	0.05	100.72	-	0.00	1.97	0.01	-	0.00	-	-	-	0
SEM9-c2-5	0.10	0.25	98.38	0.59	bdl	-	0.95	bdl	bdl	0.05	100.92	0.00	0.01	1.95	0.01	-	0.02	-	-	-	0
SEM9-c3-1	bdl	bdl	99.17	0.94	bdl	-	0.13	bdl	bdl	0.07	100.59	-	-	1.97	0.02	-	0.00	-	-	-	0
SEM9-c3-3	bdl	0.08	96.17	0.71	0.02	-	3.60	bdl	bdl	0.09	100.86	-	0.00	1.91	0.01	0.00	0.07	-	-	-	0
SEM9-c3-4	bdl	1.40	97.25	0.65	0.03	-	0.46	bdl	bdl	bdl	99.80	-	0.04	1.93	0.01	0.00	0.01	-	-	-	-
SEM9-c3-6	0.15	bdl	99.11	0.38	bdl	-	0.42	bdl	bdl	0.72	100.84	0.00	-	1.96	0.01	-	0.01	-	-	-	0
SEM9-c3-7	bdl	bdl	99.31	0.40	bdl	-	0.48	bdl	bdl	1.03	101.30	-	-	1.95	0.01	-	0.01	-	-	-	0
SEM9-c3-8	bdl	bdl	100.52	0.47	bdl	-	0.35	bdl	bdl	0.46	101.84	-	-	1.97	0.01	-	0.01	-	-	-	0
SEM9-c3-9	bdl	bdl	100.26	0.45	bdl	-	0.28	bdl	bdl	0.18	101.30	-	-	1.98	0.01	-	0.01	-	-	-	0
SEM9-c3-10	bdl	bdl	100.20	0.60	bdl	-	0.27	bdl	bdl	bdl	101.25	-	-	1.98	0.01	-	0.01	-	-	-	-
SEM9-c3-11	bdl	bdl	99.97	0.52	bdl	-	0.26	bdl	bdl	bdl	100.79	-	-	1.98	0.01	-	0.01	-	-	-	-
SEM9-c3-12	0.16	0.20	99.97	0.48	bdl	-	0.32	bdl	bdl	0.05	101.37	0.00	0.01	1.97	0.01	-	0.01	-	-	-	0
SEM9-c3-13	bdl	bdl	99.17	0.45	bdl	-	0.41	bdl	bdl	0.04	100.47	-	-	1.98	0.01	-	0.01	-	-	-	0
SEM9-c3-15	0.16	bdl	100.39	0.80	0.00	-	bdl	bdl	bdl	bdl	101.43	0.00	-	1.98	0.02	0.00	0.00	-	-	-	-
SEM9-c3-16	bdl	bdl	100.06	0.81	bdl	-	bdl	bdl	bdl	bdl	101.15	-	-	1.98	0.02	-	0.00	-	-	-	-
SEM9-c3-18	bdl	bdl	100.14	0.58	bdl	-	0.23	bdl	bdl	0.09	101.04	-	-	1.98	0.01	-	0.00	-	-	-	0
SEM9-c3-19	bdl	bdl	100.37	0.28	bdl	-	0.23	bdl	bdl	0.08	101.14	-	-	1.99	0.01	-	0.00	-	-	-	0
SEM9-c3-20	bdl	bdl	99.96	0.56	bdl	-	0.20	bdl	bdl	0.10	101.01	-	-	1.98	0.01	-	0.00	-	-	-	0
SEM9-c3-21	bdl	bdl	100.07	0.72	bdl	-	0.14	bdl	bdl	0.04	101.00	-	-	1.98	0.02	-	0.00	-	-	-	0
SEM9-c3-22	bdl	bdl	99.83	0.67	bdl	-	0.21	bdl	bdl	bdl	100.93	-	-	1.98	0.01	-	0.00	-	-	-	-
SEM9-c3-23	bdl	bdl	99.79	0.78	bdl	-	0.16	bdl	bdl	0.06	100.97	-	-	1.98	0.02	-	0.00	-	-	-	0
SEM9-c4-1	bdl	0.14	99.32	0.77	0.08	-	0.13	bdl	bdl	0.04	100.66	-	0.00	1.97	0.02	0.00	0.00	-	-	-	0
SEM9-c4-2	bdl	0.18	99.04	0.84	0.03	-	0.21	bdl	bdl	bdl	100.61	-	0.01	1.97	0.02	0.00	0.00	-	-	-	-
SEM9-c4-3	bdl	bdl	99.36	0.80	0.06	-	0.25	bdl	0.06	0.06	100.60	-	-	1.97	0.02	0.00	0.00	-	-	0.00	0
SEM9-c4-4	bdl	bdl	99.41	0.80	0.07	-	0.20	bdl	bdl	bdl	100.84	-	-	1.97	0.02	0.00	0.00	-	-	-	-
SEM9-c4-5	0.21	0.08	98.78	0.54	0.03	-	0.18	bdl	bdl	0.14	100.09	0.01	0.00	1.97	0.01	0.00	0.00	-	-	-	0
SEM9-c4-7	bdl	bdl	100.13	0.69	0.06	-	0.27	bdl	bdl	0.17	101.38	-	-	1.97	0.01	0.00	0.01	-	-	-	0
SEM9-c4-8	bdl	bdl	98.41	0.65	bdl	-	1.09	bdl	bdl	0.19	100.69	-	-	1.96	0.01	-	0.02	-	-	-	0
SEM9-c4-9	bdl	bdl	99.16	0.70	bdl	-	0.15	bdl	bdl	0.04	100.21	-	-	1.98	0.01	-	0.00	-	-	-	0
SEM9-c5-1	bdl	bdl	100.40	0.77	0.04	-	0.12	bdl	bdl	0.20	101.53	-	-	1.98	0.02	0.00	0.00	-	-	-	0
SEM9-c5-2	0.16	0.10	99.55	0.74	0.02	-	0.18	bdl	bdl	0.23	101.07	0.00	0.00	1.97	0.02	0.00	0.00	-	-	-	0
SEM9-c5-3	bdl	bdl	99.87	0.61	bdl	-	bdl	bdl	bdl	0.11	100.63	-	-	1.98	0.01	-	-	-	-	-	0
SEM9-c5-4	bdl	bdl	99.62	0.85	bdl	-	0.12	bdl	bdl	0.22	100.89	-	-	1.97	0.02	-	0.00	-	-	-	0
SEM9-c5-5	0.09	0.07	99.34	0.85	0.02	-	0.14	bdl	bdl	0.21	100.86	0.00	0.00	1.97	0.02	0.00	0.00	-	-	-	0
SEM9-c5-6	bdl	bdl	99.48	0.79	0.01	-	bdl	bdl	bdl	0.04	100.34	-	-	1.98	0.02	0.00	-	-	-	-	0
SEM9-c5-8	bdl	bdl	99.93	0.37	0.03	-	0.31	bdl	bdl	0.15	100.83	-	-	1.98	0.01	0.00	0.01	-	-	-	0
SEM9-c6-1	bdl	bdl	99.22	0.37	bdl	-	0.14	bdl	bdl	0.12	99.93	-	-	1.99	0.01	-	0.00	-	-	-	0
SEM9-c6-2	bdl	bdl	98.68	0.61	0.02	-	0.20	bdl	bdl	0.41	100.33	-	-	1.97	0.01	0.00	0.00	-	-	-	0
SEM9-c6-3	bdl	0.08	99.85	0.55	0.03	-	0.17	bdl	bdl	0.12	100.82	-	0.00	1.98	0.01	0.00	0.00	-	-	-	0
SEM9-c6-4	bdl	0.11	99.19	0.50	bdl	-	0.22	bdl	bdl	0.17	100.44	-	0.00	1.97	0.01	-	0.00	-	-	-	0
SEM9-c6-5	bdl	0.20	98.12	0.63	bdl	-	0.26	bdl	bdl	0.13	99.83	-	0.01	1.97	0.01	-	0.01	-	-	-	0
SEM9-c6-8	0.16	0.24	98.35	0.73	0.11	-	0.39	bdl	bdl	0.14	100.30	0.00	0.01	1.96	0.02	0.00	0.01	-	-	-	0
SEM9-c6-9	bdl	0.21	98.40	0.73	0.05	-	bdl	bdl	bdl	0.07	99.76	-	0.01	1.97	0.02	0.00	-	-	-	-	0
SEM9-c6-10	0.10	bdl	99.20	0.67	0.03	-	0.15	bdl	bdl	0.10	100.43	0.00	-	1.97	0.01	0.00	0.00	-	-	-	0
SEM11-c1-1	bdl	0.11	99.80	0.75	0.03	-	0.18	bdl	bdl	0.30	101.23	-	0.00	1.97	0.02	0.00	0.00	-	-	-	0
SEM11-c1-3	bdl	bdl	99.38	0.64	0.04	-	0.25	bdl	bdl	0.45	100.89	-	-	1.97	0.01	0.00	0.00	-	-	-	0
SEM11-c1-5	bdl	0.13	99.32	0.82	0.08	-	0.22	bdl	bdl	0.59	101.17	-	0.00	1.96	0.02	0.00	0.00	-	-	-	0
SEM11-c1-6	0.12	0.21	98.42	0.82	0.03	-	0.13	bdl	bdl	0.61	100.54	0.00	0.01	1.95	0.02	0.00	0.00	-	-	-	0
SEM11-c1-7	bdl	bdl	99.80	0.54	bdl	-	0.23	bdl	bdl	0.48	101.15	-	-	1.97	0.01	-	0.00	-	-	-	0
SEM11-c1-8	bdl	bdl	99.45	0.57	bdl	-	bdl	bdl	bdl	0.82	100.92	-	-	1.96	0.01	-	-	-	-	-	0
SEM11-c2-1	bdl	0.19	99.33	0.74	bdl	-	0.27	bdl	bdl	0.33	100.97	-	0.01	1.96	0.02	-	0.01	-	-	-	0
SEM11-c2-2	bdl	0.29	98.77	0.75	0.03	-	0.37	bdl	bdl	0.64	101.03	-	0.01	1.95	0.02	0.00	0.01	-	-	-	0
SEM11-c2-3	0.08	0.14	99.20	0.72	0.02	-	bdl	bdl	bdl	1.01	101.50	0.00	0.00	1.95	0.02	0.00	-	-	-	-	0
SEM11-c2-4	0.14	0.41	97.73	0.79	0.02	-	1.37	bdl	bdl	0.44	101.17	0.00	0.01	1.92	0.02	0.00	0.03	-	-	-	0
SEM11-c2-5	0.00	0.07	99.41	0.93	0.03	-	0.16	bdl	bdl	0.47	101.10	-	0.00	1.96	0.02	0.00	0.00	-	-	-	0
SEM11-c2-6	0.19	0.10	98.62	0.52	bdl	-	0.28	bdl	bdl	0.77	100.65	0.01	0.00	1.95	0.01	-	0.01	-	-	-	0
SEM11-c2-8	bdl	bdl	99.21	0.73	bdl	-	0.47	bdl	bdl	0.13	100.59	-	-	1.97	0.02	-	0.01	-	-	-	0
SEM11-c2-10	bdl	bdl	100.08	0.86	0.01	-	bdl	bdl	bdl	0.53	101.70	-	-	1.96	0.02	0.00	-	-	-	-	0
SEM11-c2-11	0.10	0.07	99.85	0.90	0.01	-	0.13	bdl	bdl	0.64	101.87	0.00	0.00	1.95	0.02	0.00	0.00	-	-	-	0
SEM11-c2-13	bdl	0.06	100.26	0.57	0.02	-	0.32	bdl	bdl	0.70	101.99	-	0.00	1.96	0.01	0.00	0.01	-	-	-	0
SEM11-c2-15	bdl	bdl	99.55	0.61	bdl	-	0.20	bdl	bdl	0.78	101.53	-	-	1.96	0.01	-	0.00	-	-	-	0
SEM11-c3-1	0.32	0.07	99.02	0.64	0.07	-	0.20	bdl	bdl	0.56	100.92	0.01	0.00	1.95	0.01	0.00	0.00	-	-	-	0
SEM11-c3-2	bdl	bdl	98.10	0.69	0.06	-	0.14	bdl	bdl	0.57	99.58	-	-	1.96	0.01	0.00	0.00	-	-	-	0
SEM11-c3-3	bdl	bdl	98.57	0.86	0.02	-	0.16	bdl	bdl	0.83	101.15	-	-	1.95	0.02	0.00	0.00	-	-	-	0
SEM11-c3-4	bdl	bdl	99.18	0.81	0.01	-	0.13	bdl	bdl	0.46	100.80	-	-	1.96	0.02	0.00	0.00	-	-	-	0
SEM11-c4-1	bdl	bdl	100.08	0.64	0.02	-	0.18	bdl	bdl	0.71	101.93	-	-	1.96	0.01	0.00	0.00	-	-	-	0
SEM11-c4-2	bdl	bdl	99.48	0.75	0.03	-	0.16	bdl	bdl	0.61	101.34	0.00	-	1.96	0.02	0.00	0.00	-	-	-	0
SEM11-c4-3	bdl	0.10	99.29	0.62	0.00	-	0.08	bdl	bdl	0.52	100.97	-	0.00	1.96	0.01	-	0.00	-	-	-	0
SEM11-c4-4	bdl	0.07	99.52	0.59	0.00	-	0.23	bdl	bdl	0.69	101.59	-	0.00	1.96	0.01	-	0.00	-	-	-	0
SEM11-c5-1	bdl	bdl	99.92	0.64	0.01	-	bdl	bdl	bdl	0.53	101.24	-	-	1.97	0.01	0.00	-	-	-	-	0
SEM11-c5-2	bdl	bdl	99.08	0.86	0.00	-	bdl	bdl	bdl	0.80	101.35	-	-	1.95	0.02	0.00	-	-	-	-	0
SEM11-c5-4	bdl	0.13	98.15	0.63	0.01	-	bdl	bdl	bdl	0.89	99.87	-	0.00	1.96	0.01	0.00	-	-	-	-	0
SEM11-c5-5	bdl	0.08	98.67	0.59	0.00	-	0.12	bdl	bdl	0.76	100.60	-	0.00	1.96	0.01	-	0.00	-	-	-	0

SEM11-c5-6	bdl	0.07	99.17	0.75	0.02	-	0.18	bdl	bdl	0.67	101.23	-	0.00	1.95	0.02	0.00	0.00	-	-	-	0
SEM11-c5-9	bdl	bdl	99.40	0.41	0.00	-	0.22	bdl	bdl	0.86	101.17	-	-	1.96	0.01	-	0.00	-	-	-	0
SEM11-c5-10	bdl	0.18	98.73	0.38	0.00	-	0.72	bdl	bdl	0.51	100.89	-	0.01	1.95	0.01	-	0.01	-	-	-	0
SEM11-c6-1	bdl	bdl	99.74	0.77	0.00	-	0.26	bdl	bdl	0.52	101.50	-	-	1.96	0.02	-	0.01	-	-	-	0
SEM11-c6-3	bdl	0.12	99.05	0.77	0.11	-	0.13	bdl	bdl	0.66	100.89	-	0.00	1.96	0.02	0.00	0.00	-	-	-	0
SEM11-c6-4	bdl	bdl	98.76	0.79	0.08	-	0.16	bdl	bdl	0.62	100.49	-	-	1.96	0.02	0.00	0.00	-	-	-	0
SEM11-c6-5	bdl	bdl	98.95	0.66	0.09	-	bdl	bdl	bdl	0.84	101.10	-	-	1.95	0.01	0.00	-	-	-	-	0
SEM11-c7-2	bdl	bdl	99.56	0.88	0.02	-	0.12	bdl	bdl	0.51	101.27	-	-	1.96	0.02	0.00	0.00	-	-	-	0
Average	0.13	0.17	99.31	0.68	0.03	-	0.30	-	0.06	0.37	100.89	0.00	0.01	1.97	0.01	0.00	0.01	-	-	-	0
Stdev	0.06	0.16	0.72	0.14	0.03	-	0.41	-	-	0.30	0.50	0.00	0.01	0.01	0.00	0.00	0.01	-	-	-	0
FG rutile																					
D.L.	0.04	0.04	0.05	0.01	0.01	0.08	0.08	0.03	0.03	0.02											
SEM11-c1-2	6.34	5.17	74.92	0.46	bdl	6.60	bdl	bdl	2.58	0.51	96.83	-	-	-	-	-	-	-	-	-	-
SEM11-c1-4	6.92	5.97	72.44	0.41	bdl	7.78	bdl	bdl	2.85	0.40	97.02	-	-	-	-	-	-	-	-	-	-
SEM11-c1-9	9.43	8.40	62.14	0.24	bdl	11.35	bdl	bdl	4.00	0.19	95.89	-	-	-	-	-	-	-	-	-	-
SEM11-c1-10	7.46	6.22	69.09	0.26	bdl	8.10	bdl	bdl	3.27	0.21	94.85	-	-	-	-	-	-	-	-	-	-
SEM11-c2-7	7.37	5.97	73.12	0.41	bdl	7.62	bdl	bdl	2.76	0.32	97.74	-	-	-	-	-	-	-	-	-	-
SEM11-c5-7	6.45	5.32	75.91	0.49	bdl	6.69	bdl	bdl	2.50	0.17	97.67	-	-	-	-	-	-	-	-	-	-
SEM11-c6-2	bdl	bdl	85.85	0.55	0.02	12.69	bdl	0.51	bdl	0.59	101.25	-	-	-	-	-	-	-	-	-	-
SEM11-c7-3	4.74	4.53	79.50	0.59	0.02	5.51	bdl	bdl	1.76	0.06	96.90	-	-	-	-	-	-	-	-	-	-
SEM11-c7-4	2.54	2.08	87.65	0.68	0.06	2.71	bdl	bdl	0.61	0.19	96.68	-	-	-	-	-	-	-	-	-	-
SEM9-c2-6	7.39	5.91	76.31	0.33	bdl	6.57	bdl	bdl	2.65	0.06	99.22	-	-	-	-	-	-	-	-	-	-
SEM9-c3-2	bdl	0.12	90.33	0.79	0.01	9.83	bdl	bdl	bdl	0.04	101.18	-	-	-	-	-	-	-	-	-	-
SEM9-c3-14	13.34	2.38	77.54	0.45	bdl	3.06	bdl	bdl	1.00	0.84	98.94	-	-	-	-	-	-	-	-	-	-
SEM9-c3-17	9.19	4.70	76.33	0.34	bdl	6.31	bdl	bdl	1.86	0.10	99.06	-	-	-	-	-	-	-	-	-	-
SEM9-c5-7	11.66	7.74	77.55	0.38	bdl	0.36	bdl	bdl	0.09	0.10	98.14	-	-	-	-	-	-	-	-	-	-
SEM9-c6-7	7.52	7.18	65.19	0.28	0.08	10.51	bdl	bdl	2.89	0.08	94.01	-	-	-	-	-	-	-	-	-	-
Average	7.72	5.12	76.26	0.44	0.04	7.05	-	0.51	2.22	0.26	97.69	-	-	-	-	-	-	-	-	-	-
Stdev	3.74	2.56	7.71	0.16	0.03	3.33	-	0.13	1.29	0.23	2.05	-	-	-	-	-	-	-	-	-	-

Abbreviations: D.L., detection limit; Stdev, standard deviation; bdl, below detection limit

Values below the detection limit are not taken into account for the calculation of average

Table A.7 Electron microprobe analyses of arsenopyrite and pyrite from gabbros of the Semnon Sb-Au deposit

Element	S	Fe	As	Sb	Au	Zn	Cu	Co	Ni	Total
	%	%	%	%	%	%	%	%	%	
Arsenopyrite										
D.L.	0.12	0.08	0.08	0.09	0.08	0.11	0.17	0.06	0.06	
SEM45-Pt-c2-37	21.75	34.85	42.86	bdl	bdl	bdl	bdl	bdl	bdl	99.77
SEM45-Pt-c2-38	21.28	33.60	43.54	0.27	bdl	bdl	bdl	0.65	bdl	99.99
SEM45-Pt-hc-40	21.60	34.74	43.27	0.30	bdl	bdl	bdl	bdl	bdl	100.05
SEM45-Pt-hc-41	21.16	34.66	43.55	0.31	bdl	bdl	bdl	bdl	bdl	99.91
SEM45-Pt-hc-44	21.39	34.95	42.97	1.01	bdl	bdl	bdl	bdl	bdl	100.38
SEM45-Pt-hc-45	21.13	34.98	43.30	0.33	bdl	bdl	bdl	bdl	bdl	99.94
SEM45-Pt-c6-47	21.30	34.80	42.01	1.26	bdl	bdl	bdl	bdl	bdl	99.60
SEM45-Pt-c6-48-1	20.92	34.21	43.08	0.16	bdl	bdl	bdl	bdl	bdl	98.44
SEM45-Pt-c6-48-2	21.58	34.92	43.39	bdl	bdl	bdl	bdl	bdl	0.08	100.11
SEM45-Pt-c6-48-3	21.24	35.10	43.38	0.20	bdl	bdl	bdl	bdl	bdl	100.05
SEM45-Pt-c6-48-4	21.58	34.78	43.38	0.10	bdl	bdl	bdl	bdl	bdl	99.93
SEM45-Pt-c6-48-5	21.91	34.89	42.98	bdl	bdl	bdl	bdl	bdl	bdl	99.99
SEM45-Pt-c6-48-6	21.43	34.89	43.20	0.19	bdl	bdl	bdl	bdl	bdl	99.84
SEM45-Pt-c6-48-7	21.43	35.13	43.26	bdl	bdl	bdl	bdl	bdl	bdl	100.12
SEM45-Pt-c6-48-8	21.29	34.99	43.60	0.24	bdl	bdl	bdl	bdl	bdl	100.25
SEM45-Pt-c6-48-9	20.99	34.51	44.31	0.35	bdl	bdl	bdl	bdl	bdl	100.30
SEM45-Pt-c6-48-10	21.41	34.73	43.48	0.29	bdl	bdl	bdl	bdl	bdl	100.03
SEM45-Pt-c6-48-11	20.79	34.57	43.97	0.40	bdl	bdl	bdl	bdl	bdl	99.81
SEM45-Pt-c6-48-12	21.13	34.43	43.79	0.18	bdl	bdl	bdl	bdl	bdl	99.64
SEM45-Pt-c6-48-13	21.29	34.58	43.84	bdl	bdl	bdl	bdl	bdl	bdl	99.86
SEM45-Pt-c6-48-14	21.06	35.05	43.65	0.38	bdl	bdl	bdl	bdl	bdl	100.15
SEM45-Pt-c6-48-15	21.21	34.88	43.60	0.33	bdl	bdl	bdl	bdl	bdl	100.09
SEM45-Pt-c6-48-16	20.89	34.78	43.91	0.32	bdl	bdl	bdl	bdl	bdl	100.04
SEM45-Pt-c6-48-17	21.36	35.11	43.83	0.26	bdl	bdl	bdl	bdl	bdl	100.71
SEM45-Pt-c6-48-18	20.99	34.72	43.67	0.32	bdl	bdl	bdl	bdl	bdl	99.90
SEM45-Pt-c6-48-19	21.11	34.93	43.76	0.31	bdl	bdl	bdl	bdl	bdl	100.21
SEM45-Pt-c6-48-20	21.40	34.93	43.49	0.28	bdl	bdl	bdl	bdl	bdl	100.15
SEM45-Pt-c6-48-21	21.08	34.64	44.00	0.19	bdl	bdl	bdl	bdl	bdl	99.94
SEM45-Pt-c6-48-22	21.72	35.22	43.09	0.46	bdl	bdl	bdl	bdl	bdl	100.60
SEM45-Pt-c6-48-23	21.60	34.86	43.46	bdl	bdl	bdl	bdl	bdl	bdl	100.19
SEM45-Pt-c6-48-24	21.18	35.04	43.59	0.39	bdl	bdl	bdl	bdl	bdl	100.28
SEM45-Pt-c6-48-25	21.31	34.72	43.55	0.44	bdl	bdl	bdl	bdl	bdl	100.17
SEM45-Pt-c6-48-26	21.54	34.65	43.67	0.41	bdl	bdl	bdl	bdl	bdl	100.35
SEM45-Pt-c6-48-27	20.80	34.94	43.92	0.36	bdl	bdl	bdl	bdl	bdl	100.27
SEM45-Pt-c6-48-28	20.97	34.69	43.89	0.34	bdl	bdl	bdl	bdl	bdl	100.08
SEM45-Pt-c6-48-29	20.83	34.78	44.04	0.27	bdl	bdl	bdl	bdl	bdl	100.02
SEM45-Pt-c6-48-30	21.22	34.71	43.74	0.27	bdl	bdl	bdl	bdl	bdl	100.06
SEM45-Pt-c6-48-31	21.16	35.08	43.40	0.19	bdl	bdl	bdl	bdl	bdl	99.94
SEM45-Pt-c6-48-32	21.51	35.33	43.41	0.11	bdl	bdl	bdl	bdl	bdl	100.55
SEM45-Pt-c6-48-33	21.42	35.27	43.11	bdl	bdl	bdl	bdl	bdl	bdl	100.01
SEM45-Pt-c6-48-34	22.32	35.65	42.14	bdl	bdl	bdl	bdl	bdl	bdl	100.23
SEM45-Pt-c6-48-35	21.67	35.15	42.33	0.62	bdl	bdl	bdl	bdl	bdl	99.82
SEM45-Pt-c6-48-36	20.76	34.74	42.67	1.31	bdl	bdl	bdl	bdl	bdl	99.49
SEM45-Pt-c6-48-37	21.46	35.37	43.36	0.30	bdl	bdl	bdl	bdl	bdl	100.70
SEM45-Pt-c6-48-38	21.73	35.01	43.35	0.09	bdl	bdl	bdl	bdl	bdl	100.29
SEM45-Pt-c6-48-39	21.35	35.05	43.23	0.09	bdl	bdl	bdl	bdl	bdl	99.74
SEM45-Pt-c6-48-40	21.94	35.32	43.51	bdl	bdl	bdl	bdl	bdl	bdl	101.00
SEM45-Pt-c6-48-41	22.95	35.50	41.17	0.11	bdl	bdl	bdl	bdl	bdl	99.83
SEM45-Pt-c6-48-42	21.74	35.19	42.34	0.66	bdl	bdl	bdl	bdl	bdl	100.04
SEM45-Pt-c6-48-43	21.73	34.86	42.81	0.27	bdl	bdl	bdl	bdl	bdl	99.84
SEM45-Pt-hc-49	21.85	35.03	42.05	0.59	bdl	bdl	bdl	bdl	bdl	99.59
SEM45-Pt-hc-50	21.47	35.54	43.10	bdl	bdl	bdl	bdl	bdl	bdl	100.28
SEM45-Pt-hc-51	21.69	35.48	43.07	0.18	bdl	bdl	bdl	bdl	bdl	100.50
SEM45-Tr-hc-52-1	20.98	34.78	43.30	1.10	bdl	bdl	bdl	bdl	bdl	100.32
SEM45-Tr-hc-52-2	21.29	34.87	43.68	0.23	bdl	bdl	bdl	bdl	bdl	100.17
SEM45-Tr-hc-52-3	21.42	34.98	43.81	0.17	bdl	bdl	bdl	bdl	bdl	100.49
SEM45-Tr-hc-52-4	21.32	34.88	43.52	bdl	bdl	bdl	bdl	bdl	bdl	99.90
SEM45-Tr-hc-52-5	20.97	34.54	42.98	0.82	bdl	bdl	bdl	bdl	bdl	99.40
SEM45-Tr-hc-52-6	21.43	34.83	42.79	0.82	bdl	bdl	bdl	bdl	0.16	100.18
SEM45-Tr-hc-52-7	22.52	35.30	42.04	bdl	bdl	bdl	bdl	bdl	bdl	99.97
SEM45-Tr-hc-52-8	21.69	34.96	43.23	bdl	bdl	bdl	bdl	bdl	0.13	100.16
SEM45-Tr-hc-52-9	20.39	34.85	43.54	0.90	bdl	bdl	bdl	bdl	bdl	99.90
SEM45-Tr-hc-52-10	20.68	34.75	43.66	0.87	bdl	bdl	bdl	bdl	bdl	99.97
SEM45-Tr-hc-52-11	20.62	34.89	43.94	0.24	bdl	bdl	bdl	bdl	bdl	99.74
SEM45-Tr-hc-52-12	21.10	34.90	42.92	0.97	bdl	bdl	bdl	bdl	bdl	100.03
SEM45-Tr-hc-52-13	20.86	35.17	43.77	0.27	bdl	bdl	bdl	bdl	bdl	100.12
SEM45-Tr-hc-52-14	20.93	34.91	43.81	0.30	bdl	bdl	bdl	bdl	bdl	100.08
SEM45-Tr-hc-52-15	20.60	35.09	43.98	0.31	bdl	bdl	bdl	bdl	bdl	100.19
SEM45-Tr-hc-52-16	20.75	34.39	43.86	0.31	bdl	bdl	bdl	bdl	bdl	99.42

SEM45-Tr-hc-52-17	21.71	34.84	42.23	0.09	bdl	bdl	bdl	bdl	bdl	98.99
SEM45-Tr-hc-52-18	20.89	35.09	43.83	bdl	bdl	bdl	bdl	bdl	bdl	99.97
SEM45-Tr-hc-52-19	20.61	34.75	44.26	0.44	bdl	bdl	bdl	bdl	bdl	100.14
SEM45-Tr-hc-52-20	21.13	34.96	43.81	0.23	bdl	bdl	bdl	bdl	bdl	100.29
SEM45-Tr-hc-52-21	20.97	34.72	43.76	0.52	bdl	bdl	bdl	bdl	bdl	100.07
SEM45-Tr-hc-52-22	20.99	34.97	43.76	0.19	bdl	bdl	bdl	bdl	bdl	100.08
SEM45-Tr-hc-52-23	21.04	34.79	43.95	0.34	bdl	bdl	bdl	bdl	bdl	100.29
SEM45-Tr-hc-52-24	21.28	34.84	43.68	0.40	bdl	bdl	bdl	bdl	bdl	100.27
SEM45-Tr-hc-52-25	20.94	35.04	43.94	bdl	bdl	bdl	bdl	bdl	bdl	100.03
SEM45-Tr-hc-52-26	21.13	34.13	43.65	0.09	bdl	bdl	bdl	0.62	0.11	99.79
SEM45-Tr-hc-52-27	21.22	35.17	43.48	0.53	bdl	bdl	bdl	bdl	bdl	100.52
SEM45-Tr-hc-52-28	20.73	35.04	44.06	0.23	bdl	bdl	bdl	bdl	bdl	100.19
SEM45-Tr-hc-52-29	21.11	34.93	43.61	0.21	bdl	bdl	bdl	bdl	bdl	100.09
SEM45-Tr-hc-52-30	21.54	34.92	43.43	0.25	bdl	bdl	bdl	bdl	bdl	100.19
SEM45-Tr-hc-52-31	21.46	34.83	43.30	0.26	bdl	bdl	bdl	bdl	bdl	99.93
SEM45-Tr-hc-52-32	21.21	35.13	43.26	0.27	bdl	bdl	bdl	bdl	bdl	99.98
SEM45-Tr-hc-52-33	20.93	34.45	43.14	0.27	bdl	bdl	bdl	bdl	bdl	98.85
SEM45-Tr-hc-52-34	20.99	35.05	43.71	0.17	bdl	bdl	bdl	bdl	bdl	99.94
SEM45-Tr-hc-52-35	20.93	35.21	43.64	0.25	bdl	bdl	bdl	bdl	bdl	100.08
SEM45-Tr-hc-52-36	22.17	35.29	42.43	bdl	bdl	bdl	bdl	bdl	bdl	100.11
SEM45-Tr-hc-52-37	21.20	34.93	43.40	bdl	bdl	bdl	bdl	bdl	bdl	99.61
SEM45-Tr-hc-52-38	21.42	35.06	43.53	bdl	bdl	bdl	bdl	bdl	bdl	100.21
SEM45-Tr-hc-52-39	20.09	34.27	46.28	0.21	bdl	bdl	bdl	bdl	bdl	101.00
SEM45-Tr-hc-52-40	21.68	35.33	43.05	0.09	bdl	bdl	bdl	bdl	bdl	100.18
SEM45-Tr-hc-52-41	21.02	34.88	43.61	0.14	bdl	bdl	bdl	bdl	bdl	99.73
SEM45-Tr-hc-52-42	21.40	34.78	43.54	0.12	bdl	bdl	bdl	bdl	bdl	99.89
SEM45-Tr-hc-52-43	21.35	35.06	43.96	bdl	bdl	bdl	bdl	bdl	bdl	100.53
SEM45-Tr-hc-52-44	21.38	34.72	43.69	0.15	bdl	bdl	bdl	bdl	bdl	99.95
SEM45-Tr-hc-52-45	21.75	34.97	42.83	0.20	bdl	bdl	bdl	bdl	bdl	99.84
SEM45-Tr-hc-52-46	20.29	34.07	46.91	0.14	bdl	bdl	bdl	bdl	bdl	101.64
SEM45-Tr-hc-52-47	21.17	35.09	43.57	bdl	bdl	bdl	bdl	bdl	bdl	100.05
SEM45-Tr-hc-52-48	21.31	34.90	43.32	bdl	bdl	bdl	bdl	bdl	bdl	99.57
SEM45-Tr-hc-53-1	22.21	35.46	42.17	bdl	bdl	bdl	bdl	bdl	bdl	100.14
SEM45-Tr-hc-53-2	21.27	34.92	43.49	0.13	bdl	bdl	bdl	bdl	bdl	99.87
SEM45-Tr-hc-53-3	21.68	35.09	43.12	bdl	bdl	bdl	bdl	bdl	bdl	99.98
SEM45-Tr-hc-53-4	21.74	35.40	42.75	bdl	bdl	bdl	bdl	bdl	bdl	99.93
SEM45-Tr-hc-53-5	22.00	35.24	42.84	0.12	bdl	bdl	bdl	bdl	bdl	100.30
SEM45-Tr-hc-53-6	21.95	35.16	43.10	bdl	bdl	bdl	bdl	bdl	bdl	100.42
SEM45-Tr-hc-53-7	21.15	35.34	43.62	0.17	bdl	bdl	bdl	bdl	bdl	100.49
SEM45-Tr-hc-53-8	21.50	35.03	43.09	0.11	bdl	bdl	bdl	bdl	bdl	99.77
SEM45-Tr-hc-53-9	21.58	34.93	43.38	bdl	bdl	bdl	bdl	bdl	bdl	100.00
SEM45-Tr-hc-53-10	22.06	35.55	42.62	bdl	bdl	bdl	bdl	bdl	bdl	100.38
SEM45-Tr-hc-53-11	21.68	35.00	43.34	0.26	bdl	bdl	bdl	bdl	bdl	100.31
SEM45-Tr-hc-53-12	21.14	35.05	43.50	0.35	bdl	bdl	bdl	bdl	bdl	100.26
SEM45-Tr-hc-53-13	20.95	34.93	43.82	0.25	bdl	bdl	bdl	bdl	bdl	100.12
SEM45-Tr-hc-53-14	21.34	34.80	43.53	0.42	bdl	bdl	bdl	bdl	bdl	100.15
SEM45-Tr-hc-53-15	20.94	34.50	43.63	0.43	bdl	bdl	bdl	bdl	bdl	99.53
SEM45-Tr-hc-53-16	21.01	35.01	43.66	0.32	bdl	bdl	bdl	bdl	bdl	100.02
SEM45-Tr-hc-53-17	20.86	34.96	43.67	0.22	bdl	bdl	bdl	bdl	bdl	99.80
SEM45-Tr-hc-53-18	21.15	35.05	43.56	0.25	bdl	bdl	bdl	bdl	bdl	100.16
SEM45-Tr-hc-53-19	20.99	34.66	43.50	0.27	bdl	bdl	bdl	bdl	bdl	99.58
SEM45-Tr-hc-53-20	20.18	34.36	45.26	0.30	bdl	bdl	bdl	bdl	bdl	100.16
SEM45-Tr-hc-53-21	21.44	35.17	43.69	0.24	bdl	bdl	bdl	bdl	bdl	100.55
SEM45-Tr-hc-53-22	20.93	34.88	43.55	0.31	bdl	bdl	bdl	bdl	bdl	99.72
SEM45-Tr-hc-53-23	20.89	34.74	43.94	0.30	bdl	bdl	bdl	bdl	bdl	100.00
SEM45-Tr-hc-53-24	21.15	34.63	43.82	0.34	bdl	bdl	bdl	bdl	bdl	99.98
SEM45-Tr-hc-53-25	21.18	34.90	43.59	0.46	bdl	bdl	bdl	bdl	bdl	100.25
SEM45-Tr-hc-53-26	20.32	34.71	44.33	0.32	bdl	bdl	bdl	bdl	bdl	99.92
SEM45-Tr-hc-53-27	20.60	34.66	44.04	0.47	bdl	bdl	bdl	bdl	bdl	99.93
SEM45-Tr-hc-53-28	20.72	34.75	44.01	0.38	bdl	bdl	bdl	bdl	bdl	99.99
SEM45-Tr-hc-53-29	21.07	35.07	43.64	0.49	bdl	bdl	bdl	bdl	bdl	100.38
SEM45-Tr-hc-53-30	20.99	34.88	43.06	1.01	bdl	bdl	bdl	bdl	bdl	100.01
SEM45-Tr-hc-53-31	20.70	35.03	43.58	0.51	bdl	bdl	bdl	bdl	bdl	99.82
SEM45-Tr-hc-53-32	21.20	35.06	43.67	0.30	bdl	bdl	bdl	bdl	bdl	100.49
SEM45-Tr-hc-53-33	21.02	35.08	43.78	0.20	bdl	bdl	bdl	bdl	bdl	100.16
SEM45-Tr-hc-53-34	21.91	35.10	42.62	bdl	bdl	bdl	bdl	bdl	bdl	99.98
SEM45-Tr-hc-53-35	20.70	34.90	44.01	0.24	bdl	bdl	bdl	bdl	bdl	99.87
SEM45-Tr-hc-53-36	21.06	34.91	43.76	0.21	bdl	bdl	bdl	bdl	bdl	100.03
SEM45-Tr-hc-53-37	20.65	34.60	43.88	0.40	bdl	bdl	bdl	bdl	bdl	99.74
SEM45-Tr-hc-53-38	20.68	34.58	43.74	0.39	bdl	bdl	bdl	bdl	0.09	99.68
SEM45-Tr-hc-53-39	20.52	34.65	43.80	0.40	bdl	bdl	bdl	bdl	0.09	99.56
SEM45-Tr-hc-53-40	20.99	34.96	43.66	0.48	bdl	bdl	bdl	bdl	bdl	100.14
SEM45-Tr-hc-53-41	20.82	35.01	43.82	0.36	bdl	bdl	bdl	bdl	bdl	100.07
SEM45-Tr-hc-53-42	20.79	34.88	43.84	0.43	bdl	bdl	bdl	bdl	bdl	99.95
SEM45-Tr-hc-53-43	20.64	35.03	43.85	0.22	bdl	bdl	bdl	bdl	bdl	99.84

SEM45-Tr-hc-53-44	21.78	35.02	42.91	bdl	bdl	bdl	bdl	bdl	bdl	99.81
SEM45-Tr-hc-53-45	21.11	34.85	43.33	0.33	bdl	bdl	bdl	bdl	bdl	99.75
SEM45-Tr-hc-53-46	21.43	34.94	43.41	0.16	bdl	bdl	bdl	bdl	bdl	100.04
SEM45-Tr-hc-53-47	21.67	34.98	43.18	0.17	bdl	bdl	bdl	bdl	bdl	100.26
SEM45-Tr-hc-53-48	21.41	35.02	43.21	0.17	bdl	bdl	bdl	bdl	bdl	99.83
Average	21.23	34.92	43.48	0.35	-	-	-	0.64	0.11	100.04
Stdev	0.45	0.29	0.64	0.25	-	-	-	0.07	0.02	0.36
Magmatic pyrite										
D.L.	0.09	0.10	0.01	0.05	0.03	0.12	0.05	0.03	0.05	
TOU1 c4-1	52.23	46.28	bdl	bdl	bdl	0.15	bdl	0.11	bdl	98.81
TOU1 c4-2	51.70	46.51	bdl	bdl	bdl	bdl	bdl	0.09	0.10	98.46
TOU1 c4-3	51.68	46.79	bdl	bdl	bdl	bdl	bdl	0.03	0.06	98.57
TOU1 c4-4	52.31	46.77	bdl	bdl	bdl	bdl	0.08	bdl	bdl	99.22
TOU1 c4-5	52.83	47.53	bdl	bdl	bdl	0.24	bdl	bdl	bdl	100.64
TOU1 c4-6	52.63	47.33	bdl	bdl	bdl	bdl	0.07	bdl	bdl	100.06
TOU1 c4-7	52.50	47.33	bdl	0.06	bdl	bdl	bdl	0.06	0.10	100.06
TOU1 c5-1	51.78	46.71	bdl	0.06	bdl	bdl	0.06	bdl	bdl	98.64
TOU1 c5-2	52.80	48.71	0.01	bdl	bdl	bdl	bdl	bdl	bdl	101.58
TOU1 c5-3	52.39	47.49	bdl	bdl	bdl	bdl	bdl	bdl	bdl	100.02
TOU1 c5-4	52.79	47.73	0.02	bdl	bdl	bdl	bdl	0.14	bdl	100.76
TOU1 c5-5	52.79	47.71	bdl	bdl	0.05	bdl	bdl	bdl	bdl	100.66
TOU1 c5-6	52.61	47.89	0.01	bdl	bdl	0.26	bdl	bdl	bdl	100.84
TOU1 c5-7	52.68	47.50	0.07	bdl	bdl	bdl	bdl	bdl	bdl	100.33
MF1 c6-1	53.17	47.71	bdl	bdl	bdl	bdl	bdl	0.05	bdl	101.07
MF1 c6-2	53.01	47.44	bdl	bdl	bdl	bdl	bdl	0.27	0.06	100.84
MF1 c6-3	53.02	46.20	0.03	bdl	bdl	bdl	bdl	0.80	bdl	100.05
MF1 c5-1	52.18	46.20	0.05	bdl	bdl	bdl	bdl	0.12	bdl	98.56
MF1 c5-2	52.85	47.94	0.06	bdl	bdl	0.13	bdl	bdl	bdl	101.05
MF1 c5-3	52.76	47.78	bdl	bdl	bdl	bdl	bdl	0.30	bdl	100.86
MF1 c5-4	52.91	47.40	bdl	bdl	bdl	bdl	bdl	bdl	bdl	100.44
Average	52.55	47.28	0.04	0.06	0.05	0.19	0.07	0.20	0.08	100.07
Stdev	0.43	0.66	0.02	0.02	0.01	0.08	0.03	0.18	0.03	0.97
Hydrothermal pyrite										
D.L.	0.16	0.08	0.04	0.08	0.07	0.11	0.20	0.06	0.06	
SEM45-Tr-hc-43-1	53.42	45.98	0.26	bdl	bdl	bdl	bdl	bdl	bdl	99.82
SEM45-Tr-hc-43-2	54.04	46.26	0.18	bdl	bdl	bdl	bdl	bdl	bdl	100.63
SEM45-Tr-hc-43-3	53.05	46.14	0.70	bdl	bdl	bdl	bdl	bdl	bdl	100.14
SEM45-Tr-hc-43-4	54.12	45.89	0.02	bdl	bdl	bdl	bdl	bdl	bdl	100.18
SEM45-Tr-hc-43-5	53.43	46.10	0.05	bdl	bdl	bdl	bdl	bdl	bdl	99.71
SEM45-Tr-hc-43-6	53.53	46.10	0.14	bdl	bdl	bdl	bdl	bdl	bdl	99.91
SEM45-Tr-hc-43-7	53.71	46.05	0.04	bdl	bdl	bdl	bdl	bdl	bdl	100.04
SEM45-Tr-hc-43-8	54.72	45.88	0.11	bdl	bdl	bdl	bdl	0.10	bdl	100.92
SEM45-Tr-hc-43-9	53.74	46.20	0.52	bdl	bdl	bdl	bdl	bdl	bdl	100.60
SEM45-Tr-hc-43-10	52.40	46.48	0.55	bdl	bdl	bdl	bdl	bdl	bdl	99.64
SEM45-Tr-hc-43-11	53.34	46.43	0.22	bdl	bdl	bdl	bdl	bdl	bdl	100.08
SEM45-Tr-hc-43-12	53.40	46.39	0.32	bdl	bdl	bdl	bdl	bdl	bdl	100.17
SEM45-Tr-hc-43-13	53.63	46.15	0.65	bdl	bdl	bdl	bdl	bdl	bdl	100.49
SEM45-Tr-hc-43-14	53.25	46.26	0.61	bdl	bdl	bdl	bdl	bdl	bdl	100.31
SEM45-Tr-hc-43-15	53.36	46.02	0.76	bdl	bdl	bdl	bdl	bdl	0.07	100.28
SEM45-Tr-hc-43-16	52.99	46.34	0.89	bdl	bdl	bdl	bdl	bdl	bdl	100.45
SEM45-Tr-hc-43-17	52.94	46.26	0.60	bdl	bdl	bdl	bdl	bdl	bdl	99.86
SEM45-Tr-hc-43-18	52.43	46.09	0.81	bdl	bdl	bdl	bdl	bdl	bdl	99.45
SEM45-Tr-hc-43-19	52.85	46.06	0.49	bdl	bdl	bdl	bdl	bdl	bdl	99.46
SEM45-Tr-hc-43-20	52.13	45.91	1.10	bdl	bdl	bdl	bdl	bdl	bdl	99.41
SEM45 c3-1	52.77	47.63	0.75	bdl	bdl	bdl	bdl	bdl	bdl	101.30
SEM45 c3-2	53.85	47.88	0.02	bdl	bdl	bdl	bdl	bdl	bdl	101.79
SEM45 c3-3	53.11	47.23	0.79	bdl	bdl	0.14	bdl	bdl	bdl	101.29
SEM45 c3-4	52.98	46.64	1.01	bdl	bdl	bdl	bdl	bdl	0.08	100.81
SEM45 c3-5	53.49	47.78	0.02	bdl	bdl	bdl	bdl	bdl	bdl	101.33
SEM45 c2-1	53.52	47.11	0.00	bdl	bdl	bdl	bdl	bdl	bdl	100.74
SEM45 c2-2	53.40	47.69	0.01	bdl	bdl	bdl	bdl	bdl	bdl	101.17
SEM45 c2-3	53.57	47.34	0.33	bdl	bdl	bdl	bdl	bdl	bdl	101.31
SEM45 c1-1	52.60	46.30	0.00	bdl	bdl	bdl	bdl	0.18	bdl	99.22
SEM45 c1-2	53.10	47.43	0.75	bdl	bdl	bdl	bdl	bdl	bdl	101.30
SEM45 c1-3	52.66	47.67	0.90	bdl	bdl	bdl	bdl	bdl	bdl	101.26
SEM45 c1-4	53.13	47.62	1.16	bdl	bdl	bdl	bdl	bdl	bdl	101.94
SEM45 c1-5	53.78	47.22	0.01	bdl	bdl	bdl	bdl	bdl	bdl	101.09
SEM45 c1-6	53.34	47.16	0.01	bdl	bdl	bdl	bdl	bdl	bdl	100.61
SEM45 c1-7	53.47	47.14	0.38	bdl	bdl	bdl	bdl	bdl	bdl	101.07
LS4A c1-2	52.79	47.43	1.08	bdl	bdl	0.17	bdl	bdl	bdl	101.51
LS4A c1-3	52.67	47.44	0.48	bdl	bdl	bdl	bdl	bdl	bdl	100.71
LS4A c1-4	53.06	47.41	0.52	bdl	bdl	bdl	bdl	bdl	bdl	101.03

LS4A c1-6	53.15	47.46	0.53	bdl	bdl	bdl	bdl	bdl	bdl	101.20
LS4A c1-7	53.21	47.23	0.56	bdl	bdl	bdl	bdl	bdl	bdl	101.06
LS4A c2-1	52.64	47.40	1.04	bdl	bdl	bdl	bdl	bdl	bdl	101.17
LS4A c2-2	52.66	47.48	0.76	bdl	bdl	0.12	bdl	bdl	bdl	101.05
LS4A c2-5	53.45	47.62	0.08	bdl	bdl	bdl	bdl	bdl	bdl	101.22
LS4A c2-6	51.80	46.65	1.26	bdl	bdl	bdl	bdl	bdl	bdl	99.78
Average	53.20	46.79	0.49			0.14		0.14	0.08	100.60
Stdev	0.54	0.67	0.38			0.04		0.03	0.02	0.70

Abbreviations: D.L., detection limit; Stdev, standard deviation; bdl, below detection limit

Values below the detection limit are not taken into account for the calculation of average

Table A.8 LA-ICP-MS results for trace elements composition of pyrite from the altered gabbro of Semnon Sb-Au deposit

Isotope	^{34}S	^{59}Co	^{60}Ni	^{62}Ni	^{63}Cu	^{65}Cu	^{66}Zn	^{72}Ge	^{74}Ge	^{75}As	^{78}Se	^{95}Mo	^{100}Ru	^{101}Ru	^{103}Rh	^{105}Pd	^{106}Pd	^{107}Ag	^{108}Pd	^{111}Cd	^{113}Cd	^{115}
	ppm																					
D.L.	148.3457	0.0004	0.0147	0.0530	0.0043	0.0054	0.0186	0.0265	0.0117	0.0972	0.4245	0.0003	0.0004	0.0001	0.0001	0.0005	0.0005	0.0019	0.0004	0.0052	0.0038	0.0
LS4A-C1-PY1-1	532000	21.1	23	26.7	14	1.77	0.49	0.7	0.069	7590	bdl	0.369	0.357	bdl	bdl	bdl	bdl	0.0182	0.0007	0.0059	0.0043	0.0
LS4A-C1-PY1-3	545000	9.9	6.5	5.9	0.92	0.84	0.076	0.387	0.012	10370	bdl	0.066	0.062	bdl	bdl	bdl	bdl	0.0061	0.0008	bdl	bdl	0.0
LS4A-C1-PY1-5	556000	11.8	25.3	23.7	0.483	0.55	0.16	0.385	0.0101	12200	bdl	0.0027	0.003	bdl	bdl	0.0013	bdl	bdl	bdl	bdl	bdl	0.0
LS4A-C1-PY1-8	563000	1.4	1.23	1.6	0.48	0.47	0.106	0.434	0.0132	15780	bdl	0.017	0.015	bdl	bdl	0.0006	bdl	0.0027	bdl	bdl	0.0008	0.0
LS4A-C1-PY1-10	528000	5.09	2.42	2.51	1.17	1.3	0.068	0.546	0.073	1790	bdl	0.157	0.145	bdl	bdl	0.001	bdl	0.0089	0.0013	bdl	0.0007	0.0
LS4A-C1-PY1-12	580000	21.3	16.1	18.7	1.2	1.26	0.228	0.49	0.037	10140	bdl	0.036	0.025	bdl	bdl	0.004	0.107	0.035	0.044	0.035		0.0
LS4A-C1-PY1-13	600000	40	58	69	2.1	2	2.14	0.412	0.045	10520	bdl	0.129	0.106	bdl	0.00025	0.0049	0.228	0.066	0.09	0.06	0.0054	0.0
LS4A-C2-PY2-1	561000	5.96	5.1	5.44	3.49	3.73	0.6	0.416	0.036	6390	bdl	0.0026	0.0008	bdl	0.00058	0.0014	0.0018	0.0271	0.0015	0.0119	0.0132	0.0
LS4A-C2-PY2-4	554000	93	82.2	86	12.2	12.3	1.9	0.541	0.101	12470	bdl	0.7	0.59	bdl	0.00053	0.0034	0.0094	0.057	0.0025	0.0201	0.0138	0.0
LS4A-C2-PY2-3	606000	7.1	10.4	10.4	3.26	3.66	8.5	0.504	0.12	6150	bdl	0.0027	0.0076	bdl	0.00053	0.0036	0.0009	0.0265	0.0007	0.0094	0.0092	0.0
LS4A-C2-PY2-7	604000	37	24.8	27.1	2.36	2.25	4	0.551	0.092	7320	bdl	0.001	0.0052	bdl	0.0044	0.0039	0.012	0.0101	0.0011	0.0052	0.0085	0.0
D.L.	120.29480	0.00049	0.01844	0.06897	0.00668	0.00894	0.02300	0.03293	0.01567	0.12621	0.48376	0.00066	0.00048	0.00014	0.00005	0.00043	0.00041	0.00233	0.00050	0.00704	0.00483	0.0
SEM45-C1-PY1-1	505000	0.86	10.99	13.8	7.97	9.4	0.49	0.51	0.062	8230	bdl	0.0067	0.0077	bdl	0.00025	bdl	0.0121	0.0263	0.0027	bdl	bdl	0.0
SEM45-C1-PY1-2	476000	35.9	79	89	5.7	5.59	2.79	0.55	0.068	9440	bdl	0.06	0.072	bdl	0.0005	0.0027	0.0155	0.032	0.0037	bdl	bdl	0.0
SEM45-C1-PY-3	528000	680	111	109	6.09	5.23	1.54	5.9	1.27	6430	1	0.038	0.038	bdl	0.00021	0.067	0.084	0.04	0.0047	0.053	0.015	0.0
SEM45-C1-PY2-1	521000	5.7	7.8	9.3	20.4	21.6	0.163	0.356	bdl	12280	bdl	0.0072	0.0013	bdl	0.00034	0.0009	bdl	bdl	bdl	bdl	bdl	0.0
SEM45-C1-PY2-2	483000	204	40	43.7	5.03	5.47	4.4	0.448	0.055	1210	2.3	0.34	0.332	bdl	0.00016	0.0029	0.019	0.063	0.0118	0.015	0.0058	0.0
SEM45-C1-PY2-3	493000	417	114	110	7.87	8.2	9	0.58	0.249	296	8.9	0.026	0.025	bdl	0.00073	0.0007	0.0017	0.137	0.0023	0.038	0.024	0.0
SEM45-C1-PY2-4	525000	363	154	165	10.6	10.4	18.1	0.467	0.07	4510	bdl	0.473	0.423	bdl	0.0006	0.0008	0.019	0.098	0.0062	0.027	0.0116	0.0
SEM45-C2-PY3-1	449000	1200	204	175	11.72	11.32	5.05	0.471	0.182	123.6	17.7	0.196	0.195	bdl	0.00166	0.0012	0.0035	0.251	0.0017	0.038	0.0227	0.0
SEM45-C2-PY3-2	456000	469	374	313	13.2	13.05	7.04	0.489	0.214	114	17.3	0.55	0.45	bdl	0.00164	0.001	0.0006	0.243	0.0013	0.0126	0.0114	0.0
SEM45-C2-PY3-3	533000	1320	137	140	6.25	6.9	3.09	0.55	0.127	2230	5.6	0.0017	0.014	bdl	0.0016	0.001	0.0009	0.103	bdl	bdl	0.008	0.0
SEM45-C3-PY4-1	566000	10.3	41.1	44.3	2.01	2.27	0.31	0.396	bdl	10120	bdl	0.0039	bdl	bdl	bdl	0.0019	0.0046	0.0066	bdl	bdl	bdl	0.0
SEM45-C3-PY4-2	465000	840	103	89	5.6	5.8	5.5	0.422	0.133	330	14.1	0.54	0.63	bdl	0.0008	0.0018	0.0044	0.079	0.002	0.0085	0.0123	0.0
SEM45-C3-PY4-3	539000	790	80	86.9	4.62	4.56	1.32	0.422	0.067	7400	9.3	bdl	0.0044	bdl	0.00083	bdl	0.002	0.09	bdl	bdl	0.0058	0.0
SEM45-C3-PY4-4	546000	11.3	11.1	13.5	5.8	5.7	6.9	0.45	0.018	9000	bdl	0.66	0.76	bdl	0.00047	bdl	bdl	0.0108	bdl	bdl	bdl	0.0
SEM45-C3-PY4-5	449000	632	109	112.4	10.5	10.5	6.8	0.53	0.283	1020	16.7	0.346	0.293	bdl	0.00093	0.0006	0.0039	0.124	0.0007	0.0094	0.013	0.0
Average	529346	278	70.4	68.9	6.35	6.00	3.49	0.69	0.13	6671	10.3	0.189	0.182		0.001	0.005	0.028	0.060	0.009	0.017	0.01	0.0
Stdev	46420	397	82.8	72.4	5.04	5.00	4.14	1.07	0.24	4584.64	6.20	0.232	0.229		0.001	0.013	0.049	0.068	0.019	0.02	0.01	0.0

Abbreviations: D.L., detection limit; Stdev, standard deviation; bdl, below detection limit

Values below the detection limit are not taken into account for the calculation of average

Table A.8 (suite)

Isotope	^{121}Sb	^{125}Te	^{182}W	^{185}Re	^{194}Pt	^{195}Pt	^{197}Au	^{205}Tl	^{208}Pb	^{209}Bi
D.L.	0.0026	0.0113	0.0002	0.0006	0.0002	0.0004	0.0004	0.0006	0.0007	0.0003
LS4A-C1-PY1-1	2.99	0.033	0.02	0.007	bdl	bdl	0.74	0.015	2.37	0.0249
LS4A-C1-PY1-3	0.83	0.029	0.0008	bdl	bdl	bdl	0.184	0.0043	1.38	0.0179
LS4A-C1-PY1-5	1.2	0.02	0.0027	bdl	bdl	bdl	0.94	0.0035	0.354	0.0013
LS4A-C1-PY1-8	3.81	0.018	0.008	bdl	bdl	bdl	0.66	0.009	1.13	0.0057
LS4A-C1-PY1-10	4.96	0.04	0.0094	bdl	bdl	bdl	0.159	0.0106	1.75	0.0219
LS4A-C1-PY1-12	13.3	0.024	0.137	bdl	0.0088	0.0035	0.666	0.0146	1.32	0.0039
LS4A-C1-PY1-13	13.2	0.03	0.51	bdl	0.0149	0.0119	1.26	0.0052	1.51	0.0159
LS4A-C2-PY2-1	57.4	0.039	0.78	bdl	bdl	bdl	1.01	0.0182	14.1	0.0159
LS4A-C2-PY2-4	217	0.026	31.1	bdl	0.0016	0.0015	2.77	0.0079	10.6	0.0366
LS4A-C2-PY2-3	74	0.055	0.12	bdl	bdl	bdl	1.11	0.0228	11.7	0.0154
LS4A-C2-PY2-7	38	0.041	0.078	bdl	0.0005	bdl	0.699	0.0431	4.13	0.0073
D.L.	0.00396	0.01119	0.00024	0.00089	0.00021	0.00007	0.00040	0.00072	0.00094	0.00037
SEM45-C1-PY1-1	124.1	0.014	18.7	bdl	0.0016	0.001	3.39	0.0041	0.545	0.0044
SEM45-C1-PY1-2	390	bdl	8.4	bdl	bdl	bdl	4.02	0.0052	2.71	0.0259
SEM45-C1-PY-3	191	0.085	5	0.001	0.0019	0.002	2.36	0.0026	8	0.094
SEM45-C1-PY2-1	8.7	bdl	0.11	bdl	bdl	bdl	22.5	bdl	0.165	bdl
SEM45-C1-PY2-2	515	0.089	0.59	bdl	0.0005	0.0022	0.598	0.0029	10.4	0.15
SEM45-C1-PY2-3	37	0.145	0.051	bdl	bdl	bdl	0.321	0.0052	54.7	1.158
SEM45-C1-PY2-4	606	0.159	2.88	bdl	0.0007	0.0011	1.27	0.0169	33.9	0.573
SEM45-C2-PY3-1	91	0.347	0.0279	bdl	bdl	bdl	0.0419	0.0153	167	2.58
SEM45-C2-PY3-2	134	0.167	0.037	bdl	bdl	bdl	0.06	0.02	168.8	1.365
SEM45-C2-PY3-3	9.4	0.093	0.0073	bdl	bdl	bdl	1.18	0.0097	75	0.78
SEM45-C3-PY4-1	14.5	bdl	0.85	bdl	bdl	bdl	2.45	0.0075	0.46	0.0168
SEM45-C3-PY4-2	310	0.15	0.115	bdl	0.0004	bdl	0.18	0.008	20.7	0.598
SEM45-C3-PY4-3	27.2	0.123	0.0127	bdl	bdl	bdl	1.27	0.0084	40.8	0.709
SEM45-C3-PY4-4	350	0.025	0.015	bdl	bdl	bdl	4.8	0.0062	0.84	0.028
SEM45-C3-PY4-5	414	0.267	0.18	bdl	0.0006	bdl	0.087	0.0136	66.9	1.111
Average	140.33	0.08	2.68	0.004	0.003	0.003	2.10	0.011	26.972	0.360
Stdev	178.98	0.09	7.03	0.001	0.003	0.002	4.3	0.01	46.68	0.62

Abbreviations: D.L., detection limit; Stdev, standard deviation; bdl, below detection limit

Values below the detection limit are not taken into account for the calculation of average

Table A.9 LA-ICP-MS results for trace elements composition of Fe-Ti oxides from the gabbro dyke of Semnon Sb-Au deposit

Isotope	^{24}Mg	^{25}Mg	^{27}Al	^{29}Si	^{31}P	^{44}Ca	^{43}Ca	^{45}Sc	^{47}Ti	^{49}Ti	^{51}V	^{52}Cr	^{53}Cr	^{55}Mn	^{56}Fe	^{57}Fe	^{59}Co	^{60}Ni	^{63}Cu	^{65}Cu	^{66}Zn
	ppm	ppm	ppm	ppm	ppm	ppm	ppm	ppm	ppm	ppm	ppm	ppm	ppm	ppm	ppm	ppm	ppm	ppm	ppm	ppm	ppm
Ilmenite																					
D.L.	0.0400	0.0988	0.1552	182	3.1	42	7.9	0.0265	0.0872	0.1288	0.0203	0.2990	0.2856	0.3193			0.0011	0.0559	0.0215	0.0337	0.0837
MF1-C1-IL1	2570	2370	2220	7000	12	3000	2700	40	350000	346100	1765	85	111	13660			18.18	7.1	0.9	3.96	255
MF1-C1-IL3-2	4700	4400	6600	36300	64	22200	22700	25.01	381400	381500	1355	55.3	63.3	15580			17.73	14.7	0.96	3.58	75.6
MF1-C1-IL3-3	15400	15200	15600	46100	63	24700	24400	50.6	369000	365000	1515	118.1	131.9	15200			25.2	30.3	1.35	4.33	108
MF1-C1-IL4	870	750	1660	2400	14	2700	2200	25.7	340000	342000	1560	111.5	136	14460			21.74	7.7	1.2	4.02	1660
MF1-C1-IL2	3300	3100	3000	9300	bdl	3500	3060	62.8	354000	350300	2263	195	222	14820			16.97	8.8	0.76	3.49	147.3
MF1-C1-IL3-4	2990	2410	3700	20000	45	17300	15400	35	369000	375000	1900	160	195	16720			12.91	9.6	0.72	3.59	88.2
MF1-C2-IL5-1	1500	1310	2750	13900	8.8	2290	1950	54	367300	366700	2105	214.4	219.8	14340			22.25	6.05	1.8	4.9	279
MF1-C2-IL5-2	1510	1212	1120	12900	52	4940	4190	49.6	364500	368500	2124	235.4	231.3	14380			18.43	4.88	0.751	12	252
MF1-C2-IL5-3	1980	1670	1640	14800	bdl	4340	3680	35.6	364800	367200	2533	207.8	212.2	13310			20.21	5.46	0.504	3.32	375
MF1-C2-IL6	1370	1050	2000	5500	27	4000	3480	31.7	364000	359000	1304	115	130	13590			22.61	6.09	0.513	3.14	155
MF1-C2-IL8	673	545	559	1370	bdl	290	277	26.35	356000	354900	2096	108.6	119.6	13570			22.95	7.8	0.541	3.1	561
MF1-C2-IL7	387	336	339	416	8	106	96	35	346500	348500	2260	158.1	175.4	13350			20.59	6.4	2	3.09	557
MF1-C3-IL9	1640	1340	2470	12100	21	14500	13800	41.6	367000	360000	1598	167	196	14610			15.16	7.5	0.556	3.19	98.6
MF1-C3-IL10	1890	1550	2100	9700	18.8	5900	5200	36.2	365000	365000	1878	278	271	13840			19.1	7.1	0.449	3.05	153.2
MF1-C3-IL11	2500	2300	4000	13400	9	5200	4600	12.91	378000	373000	1690	120.1	142.9	13810			20.5	8	0.421	3.17	107
MF1-C3-IL13	6900	6600	7700	17400	37	4430	3720	40.8	345400	343800	1976	153	173.1	13150			21.89	13.4	0.513	6.4	521
MF1-C3-IL14-1	500	425	325	2240	19	1160	960	46.7	354300	363000	1754	85.2	104.2	14950			14.75	4.6	0.468	2.99	121.8
MF1-C3-IL14-2	701	519	927	4090	9.4	3910	3250	28.5	358000	364000	2128	98.3	124	14840			13.42	5.77	0.496	3.15	426
MF1-C4-IL15-1	485	389	304	980	bdl	2870	2400	43	372700	372100	1647	97.3	113.8	16200			18.15	4.41	0.53	3.12	206
MF1-C4-IL15-2	1500	1118	696	15300	bdl	6930	5930	36	373000	376000	1556	64	77.8	14420			18.8	5.09	0.54	3.3	88.9
Average	2668	2430	2986	12260	27	6713	6200	38	361995	362080	1850	141	158	14440			19.1	8.5	0.80	4.0	312
Stdev	3390	3374	3571	11627	21	7103	7081	12	11157	11353	330	60	56	967			3.3	5.8	0.46	2.0	357
Titanohematite																					
D.L.	0.0336	0.0884	0.1103	113	2.3	32	6.0	0.0183	0.0655	0.1171	0.0151	0.2190	0.2212	0.2355			0.0008	0.0417	0.0124	0.0194	0.0625
BAN1-C1-IL1-1	5600	5000	5700	26800	33	46300	45800	28.42	863000	863000	2939	9.04	9.48	21400			36.9	38.2	82	91	165
BAN1-C1-IL2-1	1850	1528	8450	6450	3.9	7560	6420	7.81	159900	159800	4067	6.04	7.9	5477			32.1	80.8	45.4	47.6	811
BAN1-C1-IL3-1	4310	4220	5210	6380	bdl	1530	1250	6.96	151500	151600	4230	5.7	6.67	10280			27.81	59.2	24.8	26.8	248.2
BAN1-C1-IL3-2	692	559	13840	2080	bdl	930	730	6.07	137700	137300	3620	6.75	7.92	4920			31.62	68.3	42.4	44.7	661
BAN1-C1-IL6	726	578	8930	560	bdl	354	299	6.59	152600	151300	3428	3.69	4.48	6560			22.82	61.3	25.4	27.5	252.8
BAN1-C1-IL7-1	2350	2060	5810	5650	12	4650	4220	6.12	139400	139700	2768	13.03	15.3	6250			30	60.1	26	27.6	482
BAN1-C1-IL7-2	10810	10490	12100	23700	3.7	6240	5430	9.17	168700	170400	3580	3.96	4.6	6840			37	80	16.4	17.8	128.9
BAN1-C1-IL5	1746	1393	11430	3460	32.7	1100	920	4.24	141300	140300	3647	3.83	3.69	6070			30.34	71	20	21.6	701
BAN1-C2-IL8	3210	3100	5240	6720	22.8	2440	2050	6.64	146100	146900	4440	5.16	5.34	5960			23.67	62.8	41.1	43.9	366
BAN1-C2-IL9	1860	1710	10920	4200	249	910	790	7.18	146500	146600	3328	5.03	5.53	7010			31.74	65.5	30.1	32.2	305
BAN1-C2-IL10	7660	7570	12120	10900	bdl	3000	2490	8.6	152400	151800	3965	8.12	9.24	10680			31.9	87.2	31.6	32.8	393
BAN1-C2-IL11-2	566	463	13210	bdl	bdl	1830	1520	7.43	145500	144600	3990	4.44	6.15	5050			33	48.6	33.2	33.7	686
BAN1-C2-IL11-1	3600	3410	4370	7750	bdl	3630	3140	7.17	138800	138200	2922	2.05	3.24	7480			35.4	51.1	15.9	15.71	173.3
BAN1-C2-IL12	2710	2330	5450	3520	bdl	760	700	7.39	142900	144600	3220	4.7	5.3	7150			35.4	66.2	34.1	34.9	464
Average	3406	3172	8770	8321	51	5802	5411	9	199021	199007	3582	6	7	7938			31	64	33	36	417
Stdev	2914	2886	3434	7986	65	11856	11776	6	191301	191320	514	3	3	4232			4	13	17	19	224
D.L.	0.0618	0.1719	0.2645	254	11	78	13	0.0465	0.1302	0.1899	0.0321	0.5176	0.4948	0.5392			0.0034	0.0852	0.0257	0.0345	0.1520
TOU1-C1-IL2	14100	13600	18300	30100	1090	16800	14800	8.6	186200	184500	3330	1297	1375	7970			45.3	62.1	45	45.4	2480
TOU1-C1-IL3	384	352	4780	1690	bdl	460	362	4.48	164500	164200	2500	7560	8800	14700			32	52.6	20.4	22.7	7330
TOU1-C1-IL6	1340	1070	9070	10450	27	3680	3210	3.33	191000	185200	3900	630	570	1580			23.4	58.3	34	35.8	3160
TOU1-C2-IL18	205	195	5440	1410	bdl	930	800	3.58	172000	168300	3380	11020	12750	10170			34.4	49.6	28.2	29.3	6880
TOU1-C2-IL21	18800	18200	80000	164000	3800	49400	47600	9.8	188000	192000	4340	1469	1476	5130			47	97.3	17.2	18.9	430
TOU1-C2-IL20	1180	1070	4060	4480	bdl	3820	3110	3.15	179200	178500	3680	438	441	6250			25.5	70.8	40.7	43.2	3210
TOU1-C3-IL29-2	5300	5000	6700	9500	bdl	2950	2510	4.47	172700	177000	3410	930	940	9730			29.9	60.3	17.4	18.5	1210
TOU1-C3-IL27-1	4050	3560	7260	15600	40	6680	5700	5.88	187300	192400	4930	1804	1744	5870			24.92	66.2	48.3	50.9	5500
TOU1-C3-IL31-2	3100	2590	6600	22200	37	1200	1110	3.52	182000	181000	3390	841	836	4350			25.27	55.5	28.4	30.7	700
Average	5384	5071	15801	28826	999	9547	8800	5	180322	180344	3651	2888	3215	7306			32.0	64	31	33	3433
Stdev	6603	6438	24444	51580	1268	15757	15201	2	8930	9636	689	3755	4419	3851			8.8	14	12	12	2593
CG rutile																					
D.L.	0.0743	0.2295	0.3332	214	2.4	91	17	0.0661			0.0419	0.6743	0.5334	0.6413	1.0942	1.3569	0.0015	0.0876	0.0249	0.0276	0.1469
SEM9-C1-RU1-1	279	220	2700	2690	17	308	243	92			3537	253	256	14.4	1260	1089	0.024	0.142	0.8	4.12	3.16
SEM9-C1-RU1-2	320	238	370	1700	6	210	220	49.7			3780	320	299	16.3	2940	2540	0.022	0.07	0.627	3.84	14.3
SEM9-C2-RU5-1	820	830	47000	39000	13	1400	1330	86.7			3940	246	252	52	1340	1130	0.014	0.23	1.13	4.9	3.02
SEM9-C3-RU7-4	388	340	12600	9900	15	760	900	75.3			3881	621	544	15.1	920	810	0.019	0.08	0.98	4.23	6.1
SEM9-C4-RU10	3890	3490	1690	22000	bdl	9500	9900	127			3508	223.5	216.4	267	8000	6800	0.319	0.89	0.46	3.4	8.1
Average	1139	1024	12872	15058	12.8	2436	2519	86			3729	333	313	73	2892	2474	0.08	0.28	0.80	4.10	6.94
Stdev	1553	1401	19682	15648	7.0	3977	4153	28			197	165	132	110	2960	2511	0.13	0.35	0.27	0.55	4.63
D.L.	0.0714	0.2382	0.3214	192	2.0	84	17	0.0564			0.0405	0.5744	0.5156	0.6591	0.9408	1.3405	0.0033	0.0850	0.0228	0.0270	0.1347
SEM11-C1-RU1-1	590	488	800	450	10	29400	32500	92.8			4120	389	348.2	980	4590	4050	0.216	bdl	0.53	3.69	5.1
SEM11-C1-RU1-2	226	172	270	380	8	13400	14400	124			4289	477	423	410	1600	1400	0.151	0.13	0.451	3.45	2.39
SEM11-C1-RU1-3	188.4	124.4	372	287	12.7	170	159	116.8			4063	298	276.8	48.2	1250	1090	0.153	0.086	0.552	3.72	2.26
SEM11-C2-RU2-1	185.7	125.3	1144	330	bdl	61	54.1	152.4			3930	219	215.4	172	4060	3480	0.126	bdl	0.451	3.77	3.91
SEM11-C2-RU2-2	820	790	1090	440	15	135000	151000	115.7			4080	324	307	3600	4280	3690	0.179	0.25	0.6	3.59	3.05
SEM11-C2-RU2-3	610	600	245	380	bdl	127000	144000	102.2			4700	370	352	3360	2690	2440	0.054	0.3	0.45	3.9	3.76
SEM11-C5-RU8-2	636	624	316		bdl	88000	99000	125.9			2936	145.6	146.7	1950	2730	2440	0.195	0.124	0.512	3.54	4.9
SEM11-C6-RU9-1	299	250	410	510	bdl	14600	15200	111.2			4890	824	714	344	890	810	0.21	0.35	0.82	3.9	3.03
SEM11-C8-RU11	212	150	610	340	12.6	8000	7800	106			3637	444	390	249	1030	920	0.062	bdl	0.528	3.39	2.31
SEM11-C9-RU12	3500	3100	3200	3400	102	239000	265000	129			2149	157.1	151	5700	11200	9800	0.87	2.3	1.51	4.37	9.1
Average	727	642	846	724	27	65463	72911	118			3879	365	332	1681	3432	3012	0.22	0.51	0.64	3.73	3.98
Stdev	1001	897	890	1006	31	80060	89417	17			812	197	164	1933	3058	2667	0.23	0.70	0.32	0.28	2.07
FG rutile																					
D.L.	0.0878	0.2421	0.4239	218	2.7	105	20	0.0766	0.1839	0.2220	0.0543	0.7538	0.6160	0.7637			0.0042	0.1048	0.0277	0.0370	0.1604
SEM11-C1-LC1	18170	19520	29900	38900	16	14100	13200	102	522000	543000	2690	344	344	326			4.52	13.9	0.78	3.91	126.2
SEM11-C2-LC6	16720	18290	31570	49500	23	4700	4600	69.6	482000	480000	2490	238	239	138			4.04	14.18	0.59	3.22	126.1
SEM11-C6-LC8	16780	18380	30440	33200	36	40000	44000	92.8	495000	512000	2590	410	401	1050			5.71	20.67	3.2	5.6	142
SEM11-C9-LC10	17100	18660	32900	31900	45	32100	33900	169	502000	497000	1980	340	340	670			5.45	13.4	2.91	6.01	144
SEM11-C9-LC11	18460	20210	30070	55400	21	9800	9600	96.6	580000	580000	3760	390	386	223			5.11	10.7	10.7	12.7	127.6
Average	17446	19012	30976	41780	28	20140	21060	106	516200	522400	2702	344	342	481			5.0	14.6	3.6	6.3	133.2
Stdev	813	827	1257	10303	12	15160	16994	37	38486	39665	652	67	63	377			0.7	3.7	4.1	3.8	9.0

Abbreviations: D.L., detection limit; Int. Standard, internal standard; Stdev, standard deviation; bdl, below detection limit
Values below the detection limit are not taken into account for the calculation of average

Table A.9 (suite)

Isotope	^{71}Ga	^{72}Ge	^{74}Ge	^{75}As	^{88}Sr	^{89}Y	^{90}Zr	^{91}Zr	^{93}Nb	^{95}Mo	^{118}Sn	^{121}Sb	^{178}Hf	^{181}Ta	^{182}W	^{208}Pb
	ppm	ppm	ppm	ppm	ppm	ppm	ppm	ppm	ppm	ppm	ppm	ppm	ppm	ppm	ppm	ppm
Ilmenite																
D.L.	0.0017	0.0809	0.0402	0.3052	0.0005	0.0004	0.0004	0.0061	0.0000	0.0022	0.0240	0.0082	0.0001	0.0000	0.0008	0.0030
MF1-C1-IL1	1.24	0.66	0.358	bdl	6.3	11.5	835	919	103.6	1.04	1.58	0.216	12	6.16	0.13	0.32
MF1-C1-IL3-2	3.5	3.45	2.27	0.56	56.1	28	1379	1595	220	1.62	2.93	2.41	20.3	12.48	1.5	2.21
MF1-C1-IL3-3	6.1	1.77	1.24	0.53	34.6	48.2	1670	1940	197	3.05	4.73	1.24	30.9	9.24	0.67	1.33
MF1-C1-IL4	1.47	1	0.56	bdl	2.77	4.1	853	856	122.5	1.2	1.47	0.3	11.81	4.56	0.05	0.9
MF1-C1-IL2	2.22	0.84	0.51	bdl	8.5	10.6	696	701	48.6	0.466	1.14	0.275	8.04	3.85	0.13	0.31
MF1-C1-IL3-4	2.4	2.45	1.74	0.55	39.9	22.8	1006	1020	75	0.89	2.95	1.88	15	4.7	0.85	1.74
MF1-C2-IL5-1	1.28	0.73	0.359	bdl	7.7	14.7	1053	1226	73	0.88	1.53	0.188	15.5	4.67	0.2	0.292
MF1-C2-IL5-2	0.78	0.88	0.409	0.34	9.2	11.1	943	1099	62.2	0.606	1.48	0.346	12.06	4.47	0.16	0.411
MF1-C2-IL5-3	0.99	0.524	0.239	bdl	6.71	4.03	407	406	99	0.657	1.75	0.117	7.54	6.2	0.11	0.263
MF1-C2-IL6	0.83	0.8	0.51	bdl	7.7	6.51	757	768	53.6	0.55	1.43	0.291	10.45	3.34	0.13	0.39
MF1-C2-IL8	0.51	0.513	0.171	bdl	0.52	4.29	730	723	62.7	0.585	1.03	0.015	8.91	4.68	0.04	0.02
MF1-C2-IL7	0.41	0.528	0.16	bdl	0.29	7.81	677	671	49.7	0.426	0.837	0.016	7.57	3.91	0.02	0.019
MF1-C3-IL9	1.24	1.83	1.21	bdl	33.1	17.6	1060	1260	63.2	0.64	1.74	1.102	13.4	4.46	0.73	1.188
MF1-C3-IL10	0.78	0.77	0.4	bdl	3.86	12.6	1008	1160	62	0.53	2	0.179	12.38	4.22	0.24	0.279
MF1-C3-IL11	1.06	0.52	0.38	bdl	23	6.1	666	666	94	1.45	2.21	0.194	12.57	5.05	0.13	0.28
MF1-C3-IL13	2.91	0.78	0.417	bdl	17	8.38	470	464	47.3	0.7	1.4	0.345	6.11	3.59	0.12	0.383
MF1-C3-IL14-1	0.288	0.59	0.301	bdl	3.17	7.73	976	1051	90.6	0.85	1.26	0.154	11.56	5.97	0.11	0.145
MF1-C3-IL14-2	0.624	0.76	0.37	bdl	8.7	8.05	675	691	70.1	0.591	1.095	0.356	8.2	5.22	0.16	0.313
MF1-C4-IL15-1	0.349	0.503	0.69	bdl	12.6	6.7	940	1030	115	0.98	2.41	0.156	13.5	6.25	0.11	0.111
MF1-C4-IL15-2	0.58	0.83	0.49	bdl	10.2	8.46	1107	1298	119.2	0.889	1.95	0.362	14.33	6.98	0.27	0.439
Average	1.48	1.04	0.64	0.50	14.6	12.5	895	977	91	0.93	1.85	0.51	13	5.5	0.29	0.57
Stdev	1.40	0.77	0.55	0.21	15.1	10.5	293	375	47	0.59	0.89	0.65	5	2.1	0.37	0.60
Titanohematite																
D.L.	0.0008	0.0643	0.0304	0.1892	0.0004	0.0001	0.0000	0.0000	0.0000	0.0011	0.0161	0.0059	0.0002	0.0000	0.0004	0.0022
BAN1-C1-IL1-1	4.1	4.02	3.4	17.2	62.9	57.1	2306	2726	178	5.24	4.55	2.9	30.39	11.05	0.53	5.79
BAN1-C1-IL2-1	5.21	2.13	1.63	4.66	5.21	12.3	283	290	70.6	3.25	5.78	1.67	6.46	3.4	0.27	13.1
BAN1-C1-IL3-1	5.5	1.71	1.242	2.41	12.4	11.03	265.2	266	54.5	0.948	3.36	1	4.74	1.626	0.08	8.5
BAN1-C1-IL3-2	5.93	1.49	1.207	3.26	1.25	1.06	182.8	186.1	32.28	0.74	3.29	0.87	3.54	1.244	0.03	9.08
BAN1-C1-IL6	4.62	1.54	1.225	0.3	3.55	3.75	265	268	113.1	2.8	4.51	0.217	6.33	3.53	0.03	1.96
BAN1-C1-IL7-1	4.6	1.56	1.27	3.73	8.3	6.96	205	205	54	2.96	5.5	1.19	4.98	2.839	0.33	12.86
BAN1-C1-IL7-2	8.58	2.55	1.99	16.37	18.1	10.22	238	238	152.5	6.9	6.26	5.84	6.56	4.51	0.25	49.2
BAN1-C1-IL5	4.99	1.37	1.03	5.86	4.9	2.59	209.8	207.4	40.24	0.995	3.75	1.63	3.95	1.648	0.09	21
BAN1-C2-IL8	5.36	2.08	1.429	2.35	11.3	10.56	251	252	80.4	1.35	4.1	0.879	5.48	1.891	0.15	4.39
BAN1-C2-IL9	5.62	1.5	1.128	1.67	1.8	2.29	218	222	93	2.01	3.84	0.56	4.99	2.39	0.3	6.3
BAN1-C2-IL10	6.79	1.7	1.291	11.95	11.9	7.36	222	219.8	40.5	0.57	4.69	4.02	3.98	1.294	0.18	41.5
BAN1-C2-IL11-2	5.66	1.54	1.192	1.65	3.28	1.1	247	247	100.7	1.155	3.72	0.56	5.07	1.953	0.01	7.1
BAN1-C2-IL11-1	4.59	1.94	1.5	8.67	7.72	6.28	220	224	137.8	4.12	5.78	2.84	5.55	3.93	0.16	34.8
BAN1-C2-IL12	5.47	1.89	1.45	1.13	5.18	6.9	285	297	156.6	4.89	7.37	0.406	6.59	4.51	0.08	3.84
Average	5.5	1.9	1.5	5.8	11	10	386	418	93	2.7	4.8	1.8	7.0	3.3	0.18	16
Stdev	1.1	0.7	0.6	5.6	16	14	554	665	48	2.0	1.2	1.6	6.8	2.5	0.15	15
D.L.	0.0035	0.1360	0.0702	0.5317	0.0004	0.0003	0.0004	0.0026	0.0002	0.0050	0.0351	0.0193	0.0000	0.0000	0.0010	0.0054
TOU1-C1-IL2	9.66	3.77	3.04	4.75	20.5	28.3	425	484	79.4	1.96	4.78	10.24	8.95	2.03	0.1	31
TOU1-C1-IL3	7.38	2.87	2.35	1.43	6.76	4.84	177.5	218	105.5	5.67	9.6	2.92	5.55	3.33	0.03	5.69
TOU1-C1-IL6	6.57	2.36	1.98	2.36	23.2	4.98	196	241	98.4	5.55	5.63	2.7	6.2	3.31	0.09	3.36
TOU1-C2-IL18	7.75	1.7	1.23	0.6	9.4	2.03	203	227	75.8	2.62	2.9	5.94	5.57	1.99	0.05	2.85
TOU1-C2-IL21	21.3	3.7	2.58	8.02	237	38	325	373	75.2	3.2	4.67	5.14	6.04	2.91	0.33	16.9
TOU1-C2-IL20	6.05	3.08	2.51	6.58	16.8	6.27	222	272	92.8	4.58	6.7	7.05	6.35	3.05	0.05	8.4
TOU1-C3-IL29-2	6.6	2.09	1.75	3.03	7.64	4.5	183	216	99.6	8.3	8.5	2.21	5.59	3.63	0.26	7.05
TOU1-C3-IL27-1	7.47	2.75	2.31	3.69	16.1	10.81	229	272	54.5	1.21	3.36	7.44	4.71	1.22	0.08	5.2
TOU1-C3-IL31-2	4.7	1.91	1.63	0.82	6.2	3.71	340	360	110	5.05	3.58	0.94	6.6	3.02	0.05	3.3
Average	8.6	2.7	2.2	3.5	38	11	256	296	88	4.2	5.5	5.0	6.2	2.7	0.12	9.3
Stdev	4.9	0.7	0.6	2.6	75	13	87	91	18	2.2	2.3	3.0	1.2	0.8	0.10	9.2
CG rutile																
D.L.	0.0045	0.1421	0.0687	0.4206	0.0006	0.0000	0.0000	0.0080	0.0000	0.0017	0.0368	0.0425	0.0016	0.0000	0.0030	0.0052
SEM9-C1-RU1-1	1.05	0.67	0.79	3.54	35.9	8.6	520	450	172	0.26	0.706	541	11.3	10.38	7.85	1.18
SEM9-C1-RU1-2	0.45	0.4	0.48	1.71	12.6	4.13	791	666	196	0.85	1.77	226	13.11	10.83	10.8	1.037
SEM9-C2-RU5-1	11.9	0.97	0.78	1.65	34.9	12.01	681	618	146.7	0.53	1.33	252	10.06	9.66	17.7	1.83
SEM9-C3-RU7-4	3.2	0.41	0.4	0.76	15.4	3.51	384	347	104.2	0.239	1.16	261	8.3	5.91	12.8	1
SEM9-C4-RU10	0.9	0.51	0.48	0.7	40	9.1	880	770	180.4	1.36	1.6	135	16.6	9.5	10.9	0.99
Average	3.50	0.59	0.59	1.67	28	7.5	651	570	160	0.65	1.31	283	11.9	9.3	12.0	1.21
Stdev	4.81	0.24	0.18	1.15	13	3.6	201	170	36	0.47	0.41	153	3.2	1.9	3.6	0.36
D.L.	0.0030	0.1399	0.0679	0.3882	0.0011	0.0000	0.0020	0.0019	0.0009	0.0049	0.0333	0.0311	0.0004	0.0001	0.0008	0.0049
SEM11-C1-RU1-1	0.93	0.44	0.405	0.49	135	13.7	820	710	136.8	0.119	0.668	7.7	13.6	9.73	12.5	1.52
SEM11-C1-RU1-2	0.473	0.35	0.323	0.48	69	14.4	1240	1130	144	0.176	0.587	5.6	16.8	8.92	4.1	1.89
SEM11-C1-RU1-3	0.474	0.39	0.46	0.61	12.8	6.21	1620	1480	221	0.197	1.33	4.88	33.3	11.68	4.2	1.11
SEM11-C2-RU2-1	1.37	0.25	0.278	0.2	9.6	1.95	1262	1067	346	0.124	1.52	2.02	31.2	17.55	0.09	0.736
SEM11-C2-RU2-2	1.3	0.41	0.279	0.18	590	21.6	640	564	102.5	0.64	0.75	3.17	10.5	7.68	3.6	3.3
SEM11-C2-RU2-3	0.89	0.87	0.69	1.11	430	23	469	426	86.4	0.46	0.69	112	7.98	6.76	7.4	1.89
SEM11-C5-RU8-2	0.476	0.47	0.42	0.19	600	15.1	1980	1790	250	0.91	0.948	7.2	22.5	14.6	6.9	3.05
SEM11-C6-RU9-1	0.5	0.39	0.41	0.66	61.2	12.81	435	397	51.8	0.19	0.369	7.6	6.21	5	3.73	2.96
SEM11-C8-RU11	0.399	0.3	0.237	0.26	35.7	12.7	1670	1500	107.4	0.51	0.95	1.99	26.7	7.65	0.46	0.79
SEM11-C9-RU12	3.6	1.15	0.84	1.7	930	29.7	1150	1040	227	0.9	3.2	91	20.7	12.44	6.8	4.9
Average	1.04	0.50	0.43	0.59	287	15.1	1129	1010	167	0.42	1.10	24	19	10.2	5.0	2.2
Stdev	0.97	0.28	0.19	0.49	327	8.1	531	482	91	0.31	0.81	41	10	3.9	3.6	1.3
FG rutile																
D.L.	0.0035	0.1823	0.0758	0.4587	0.0016	0.0007	0.0000	0.0000	0.0000	0.0066	0.0378	0.0330	0.0010	0.0000	0.0010	0.0049
SEM11-C1-LC1	13.45	3.22	2.55	5.74	102	145	1800	1580	278	3.3	56.1	227	29.7	12.1	34.9	3.02
SEM11-C2-LC6	11.34	2.27	1.96	3.81	44	92.6	1550	1340	201	1.2	23.4	184	24.1	10.25	30.3	2.74
SEM11-C6-LC8	12.7	3.32	2.57	7.34	156	113	1240	1060	131.3	1.44	28.5	173.6	24.6	7.7	38.1	3.57
SEM11-C9-LC10	11.9	2.52	2.15	7.9	132	125	2750	2550	251	2.64	25.1	246	45.1	8.55	42.5	2.64
SEM11-C9-LC11	14.39	3.12	2.71	9.6	77	116	1152	1003	127.2	1.5	35.9	238	17.2	8.37	23.6	17.6
Average	12.8	2.9	2.4	6.9	102	118	1698	1507	198	2.0	34	214	28	9.4	33.9	5.9
Stdev	1.2	0.5	0.3	2.2	44	19	642	627	68	0.9	13	33	10	1.8	7.3	6.5

Abbreviations: D.L., detection limit; Int. Standard, internal standard; Stdev, standard deviation; bdl, below detection limit

Values below the detection limit are not taken into account for the calculation of average

Research Highlights

- Hydrothermal breakdown of ilmenite-titanohematite to rutile records early Sb mineralization in the Sb-Au district.

- EPMA and LA-ICP-MS data show metal mobility during mineral replacement.

- Metal mobility is characterized by a large release of Fe, Mn, Zn, Co, Ni, Sn, Mo and U into fluid, and by an incorporation of Sb and W into hydrothermal rutile.

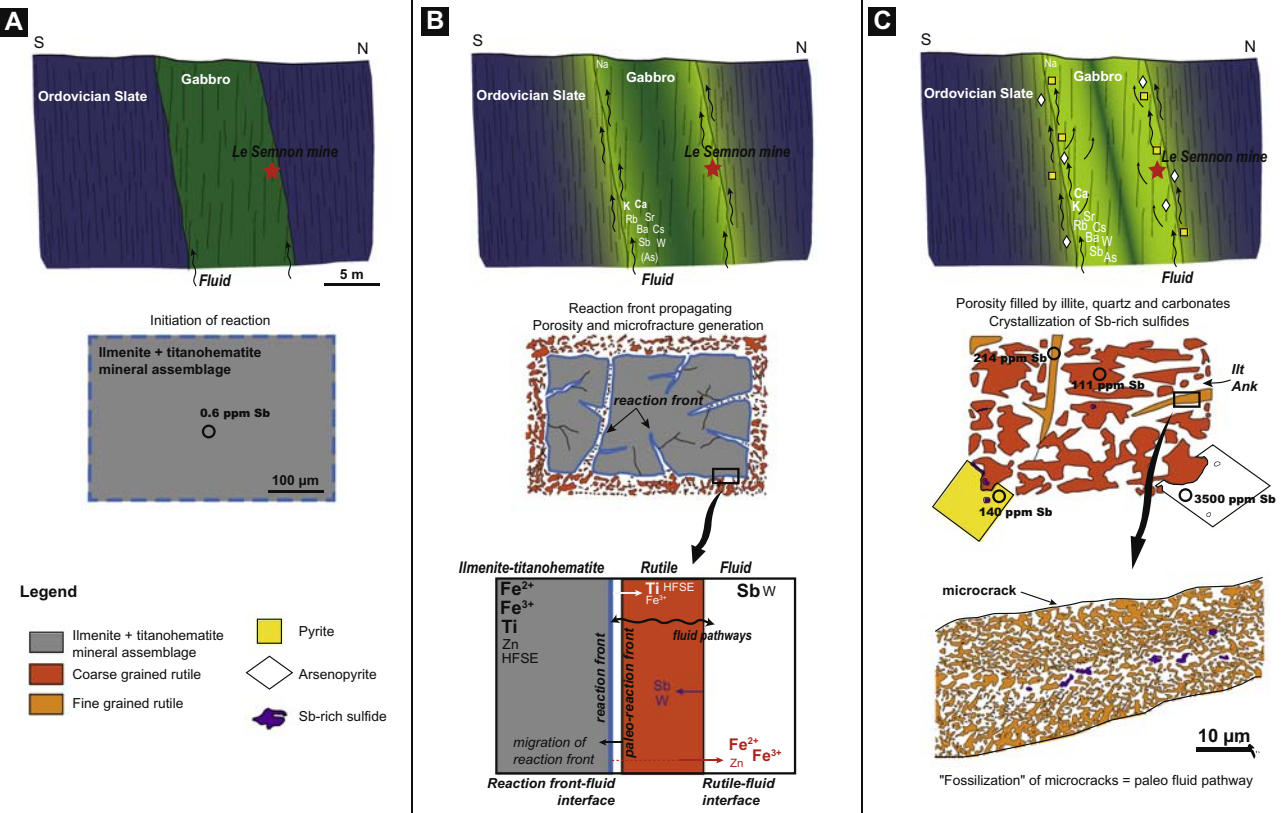
A
S
N
Ordovician Slate
Gabbro
Le Semnon mine
Fluid
5 m
Initiation of reaction
Ilmenite + titanohematite
mineral assemblage
0.6 ppm Sb
100 µm
Legend
Ilmenite + titanohematite mineral assemblage
Coarse grained rutile
Fine grained rutile
Pyrite
Arsenopyrite
Sb-rich sulfide
B
S
N
Ordovician Slate
Gabbro
Le Semnon mine
Na
K Ca
Rb Sr
Ba Cs
Sb W
(As)
Fluid
Reaction front propagating
Porosity and microfracture generation
reaction front
Ilmenite-titanohematite
Rutile
Fluid
Fe2+
Fe3+
Ti
Zn
HFSE
Ti HFSE
Fe3+
Sb W
fluid pathways
reaction front
paleo-reaction front
Sb
W
migration of
reaction front
Fe2+
Fe3+
Zn
Reaction front-fluid
interface
Rutile-fluid
interface
C
S
N
Ordovician Slate
Gabbro
Le Semnon mine
Na
Ca
K
Rb
Sr
Cs
Ba
W
Sb
As
Fluid
Porosity filled by illite, quartz and carbonates
Crystallization of Sb-rich sulfides
214 ppm Sb
111 ppm Sb
Ilt
Ank
140 ppm Sb
3500 ppm Sb
microcrack
10 µm
"Fossilization" of microcracks = paleo fluid pathway

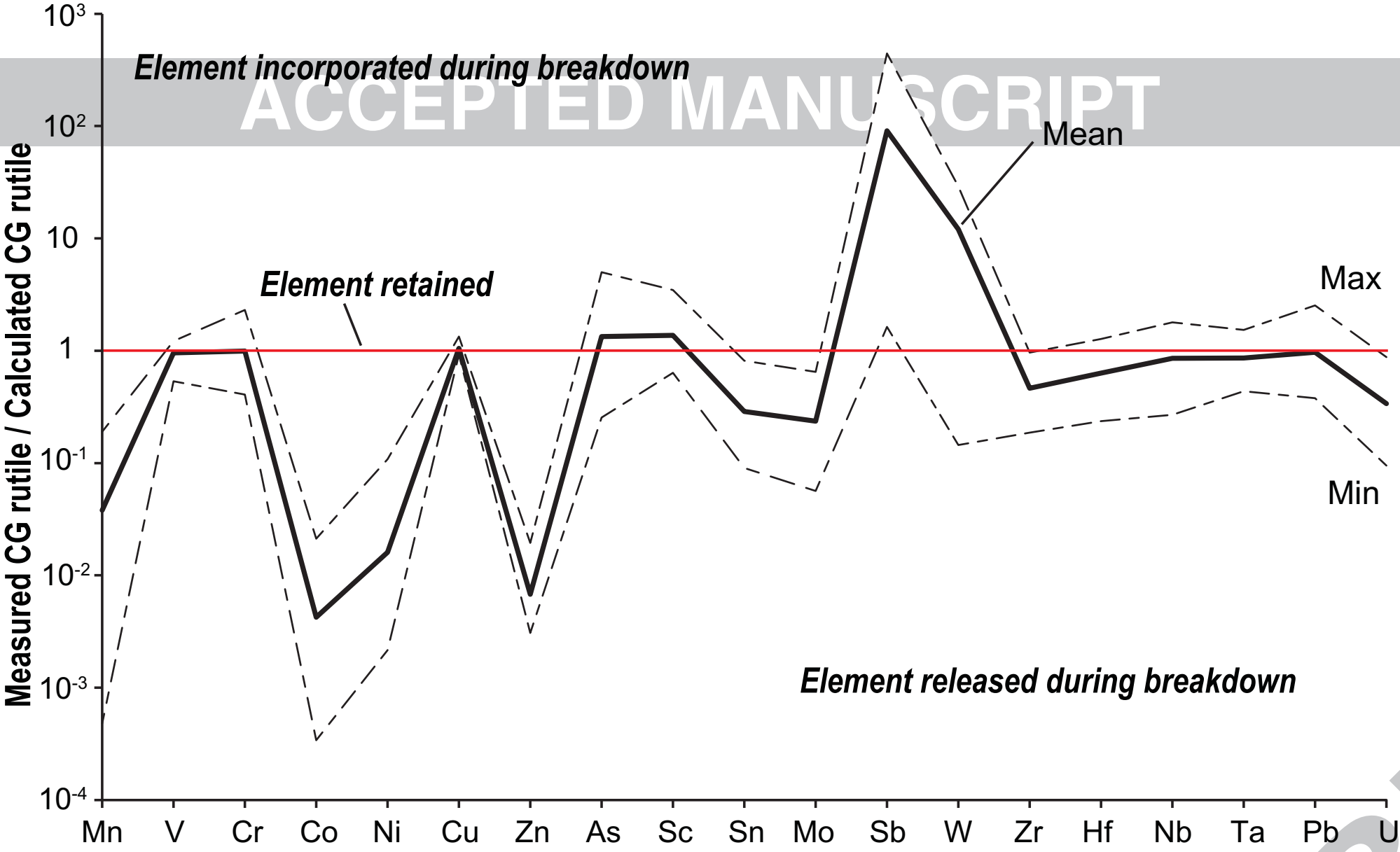

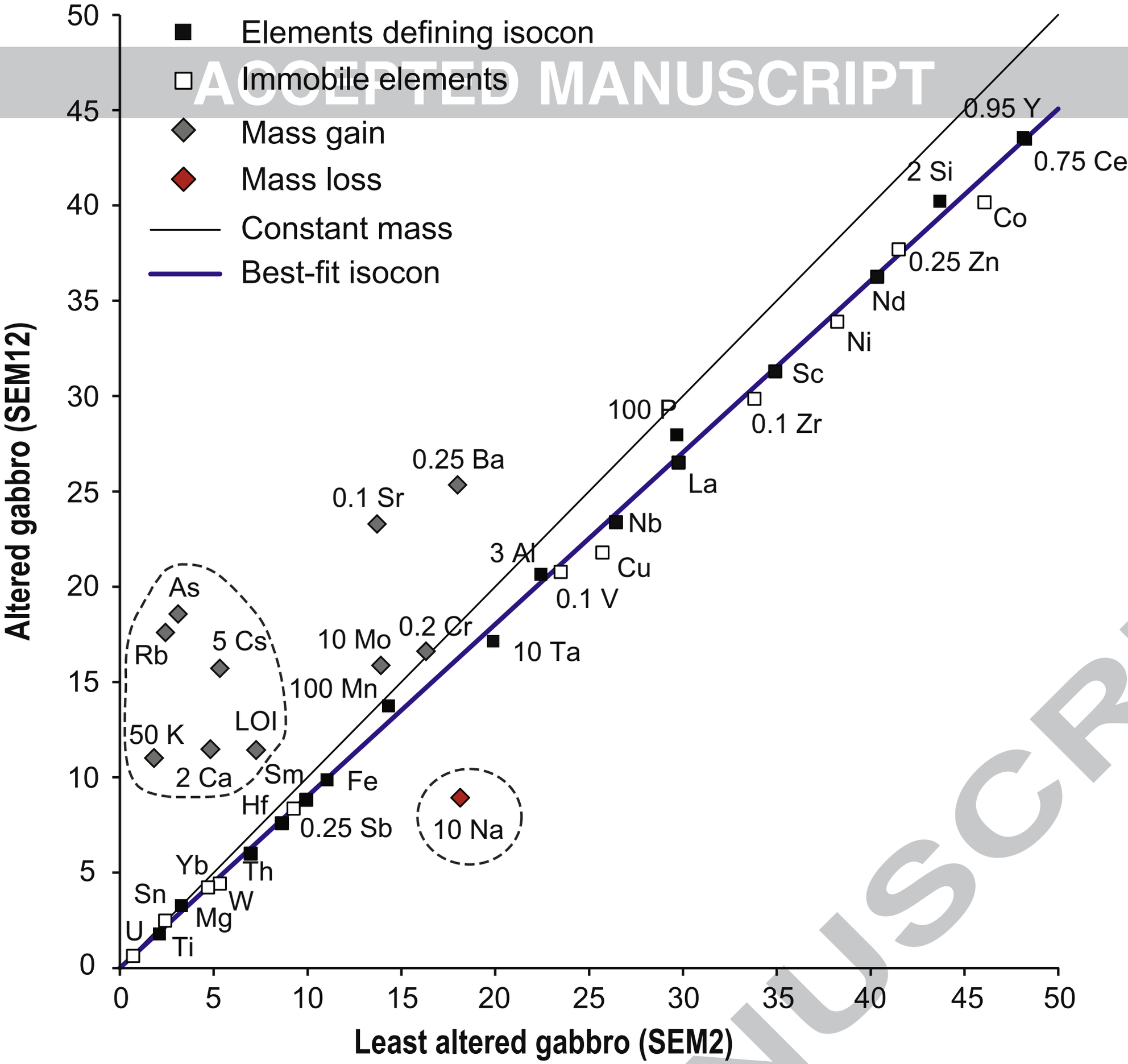

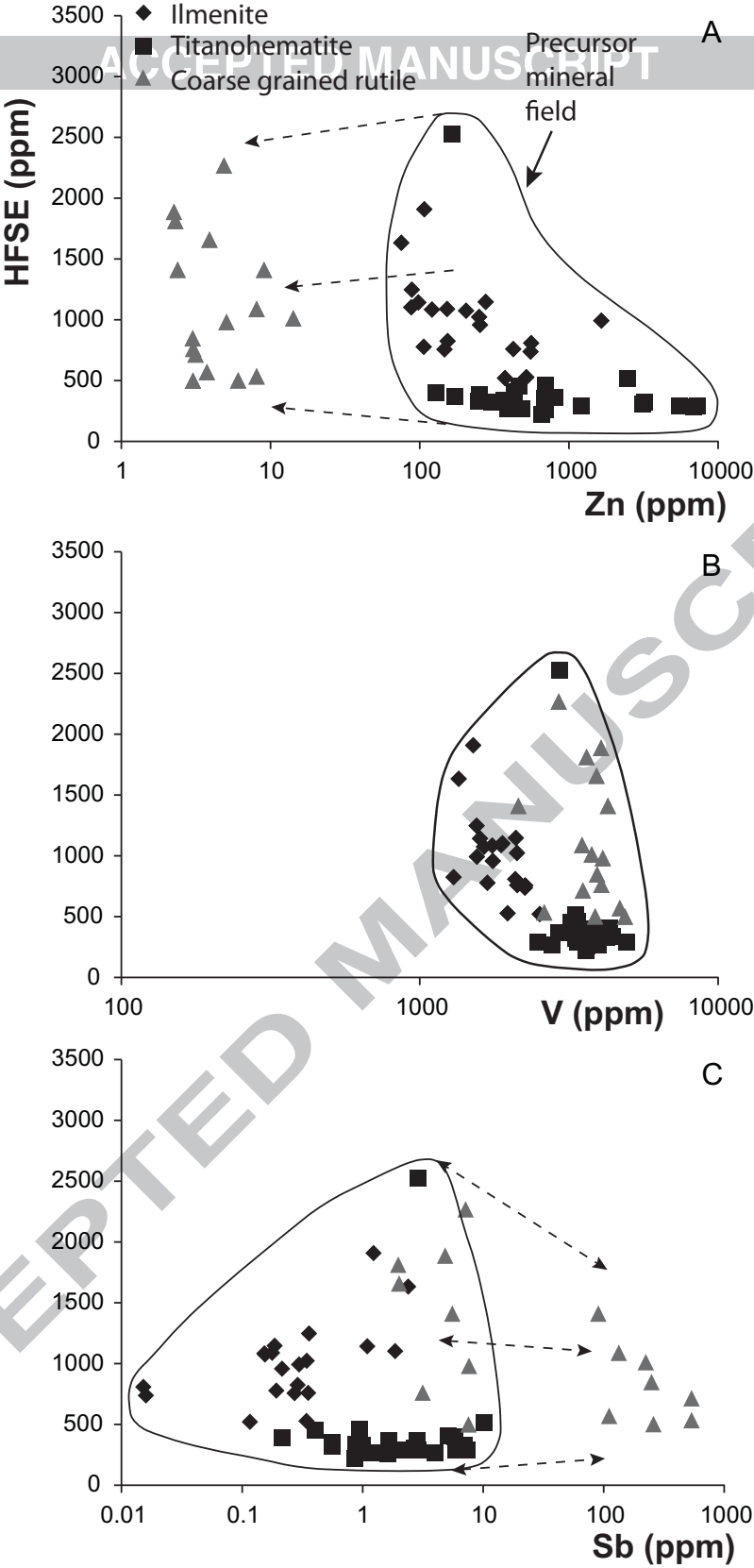

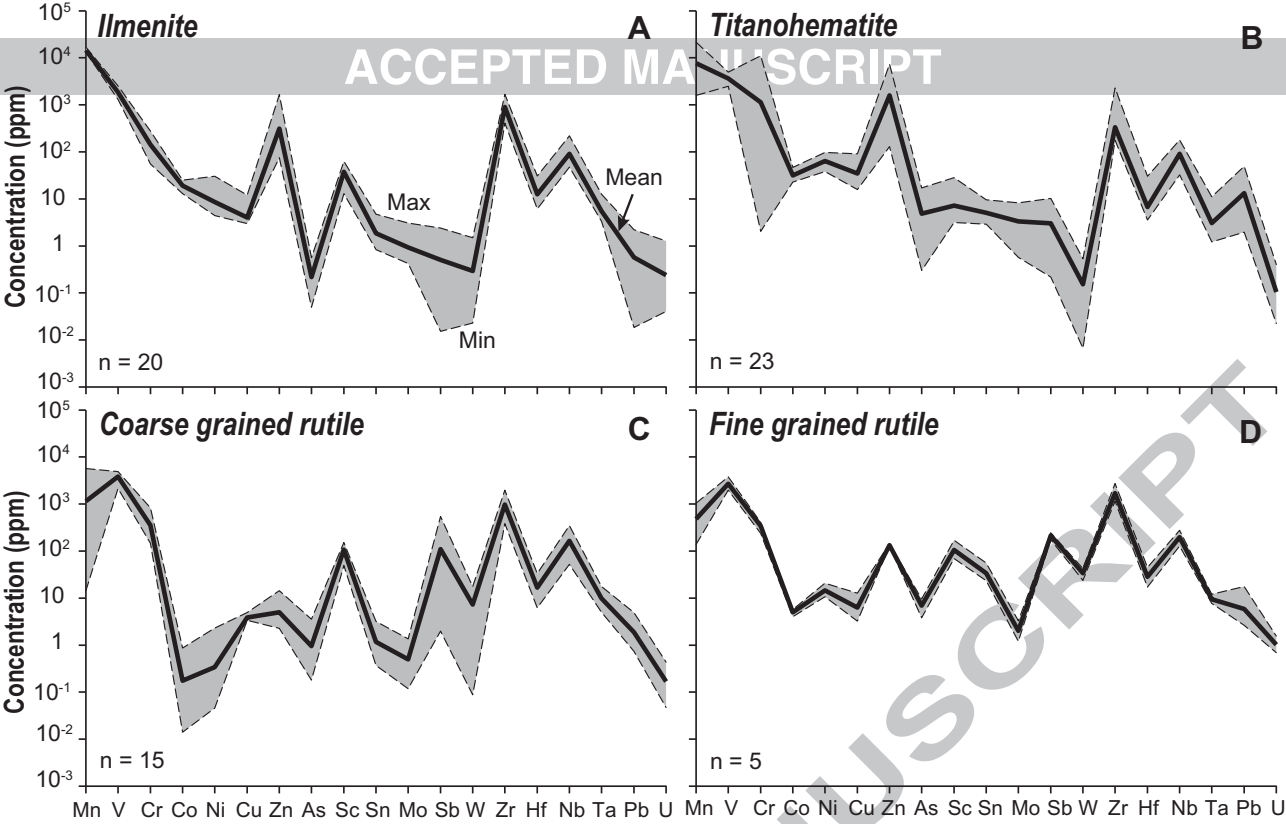

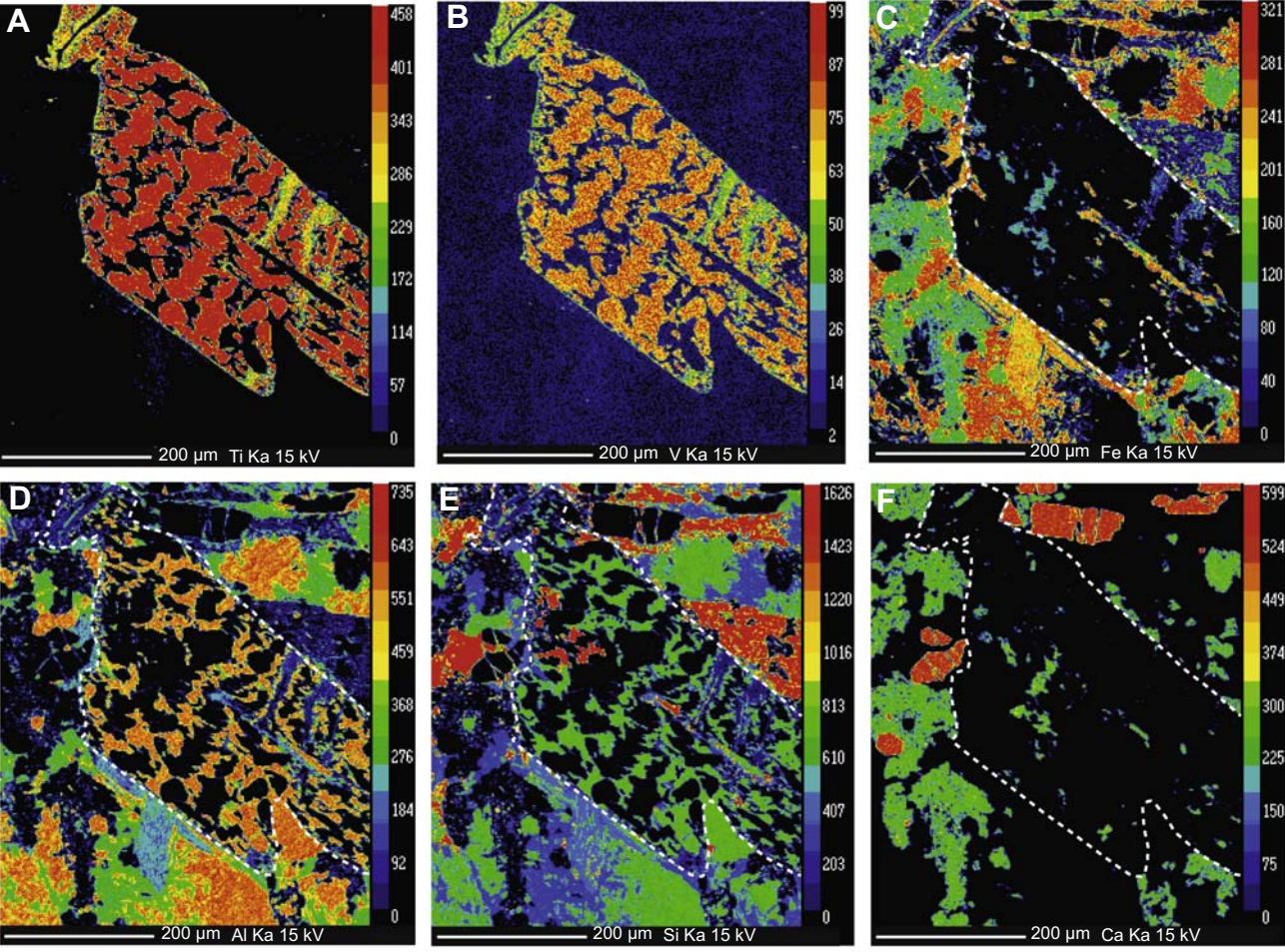
A
458
401
343
286
229
172
114
57
0
200 µm Ti Ka 15 kV
B
99
87
75
63
50
38
26
14
2
200 µm V Ka 15 kV
C
321
281
241
201
160
120
80
40
0
200 µm Fe Ka 15 kV
D
735
643
551
459
368
276
184
92
0
200 µm Al Ka 15 kV
E
1626
1423
1220
1016
813
610
407
203
0
200 µm Si Ka 15 kV
F
599
524
449
374
300
225
150
75
0
200 µm Ca Ka 15 kV

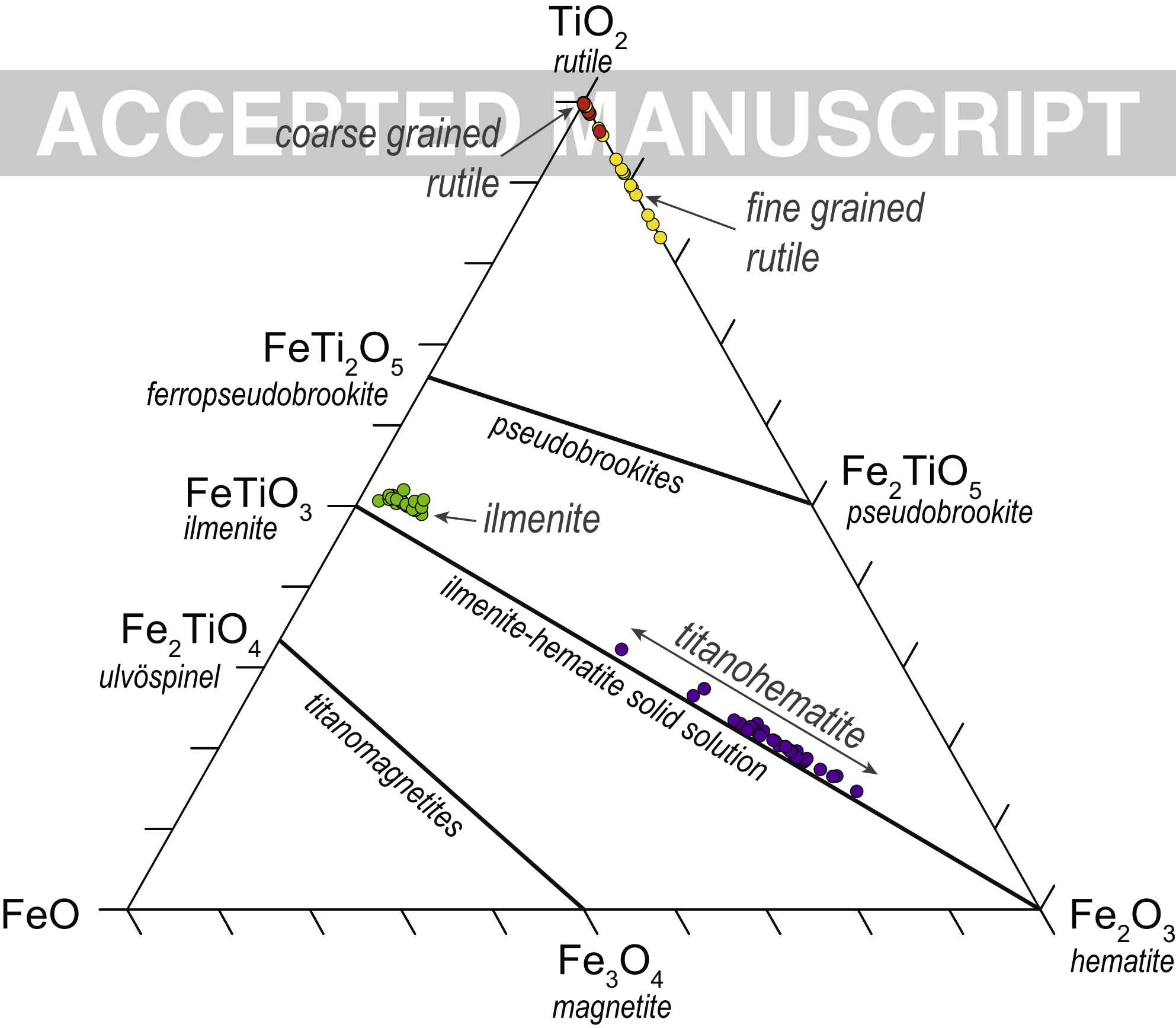

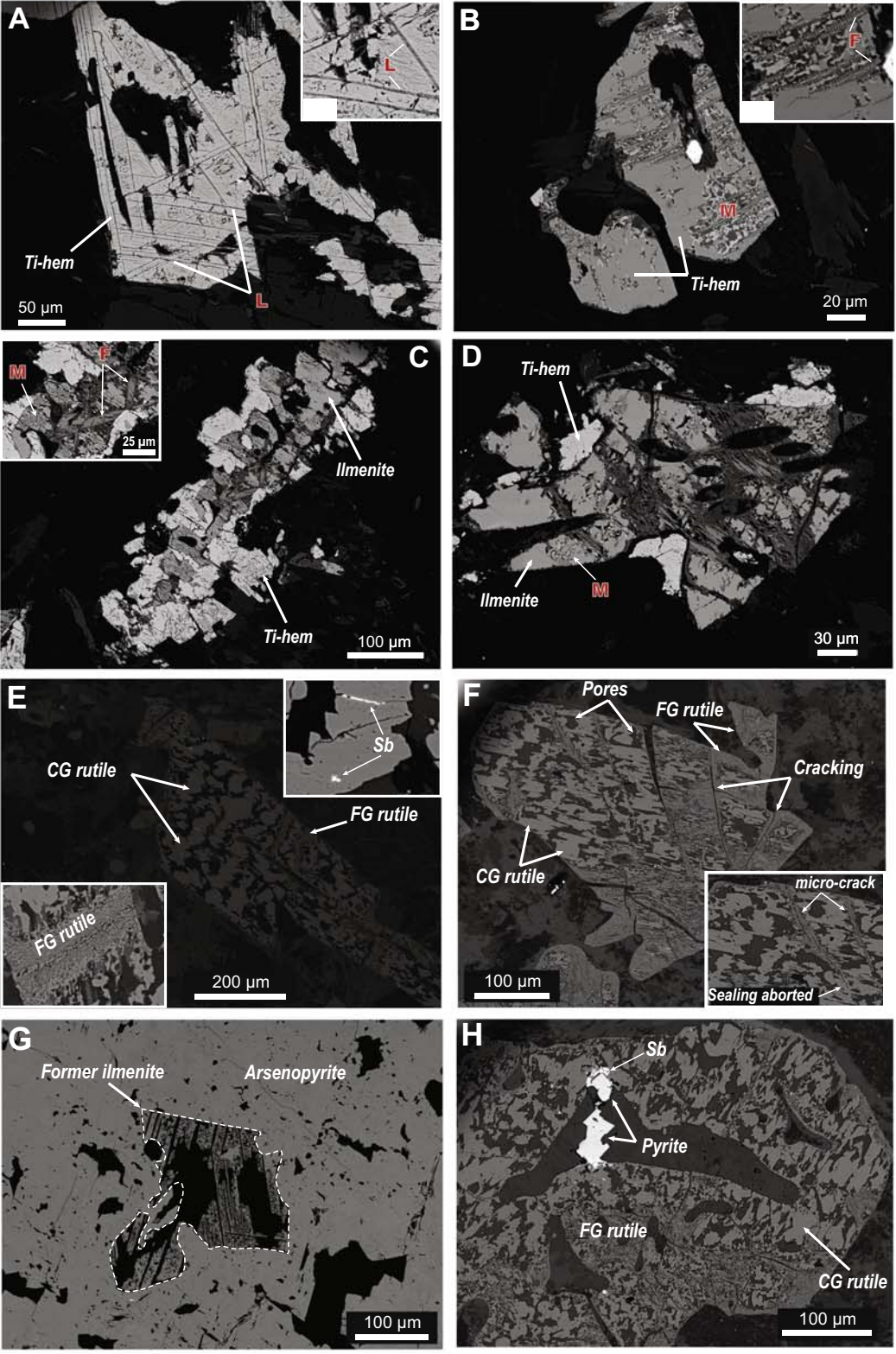
A
L
Ti-hem
L
50 µm
B
F
M
Ti-hem
20 µm
M
F
25 µm
C
Ilmenite
Ti-hem
100 µm
D
Ti-hem
Ilmenite
M
30 µm
E
Sb
CG rutile
FG rutile
FG rutile
200 µm
F
Pores
FG rutile
Cracking
CG rutile
micro-crack
Sealing aborted
100 µm
G
Former ilmenite
Arsenopyrite
100 µm
H
Sb
Pyrite
FG rutile
CG rutile
100 µm

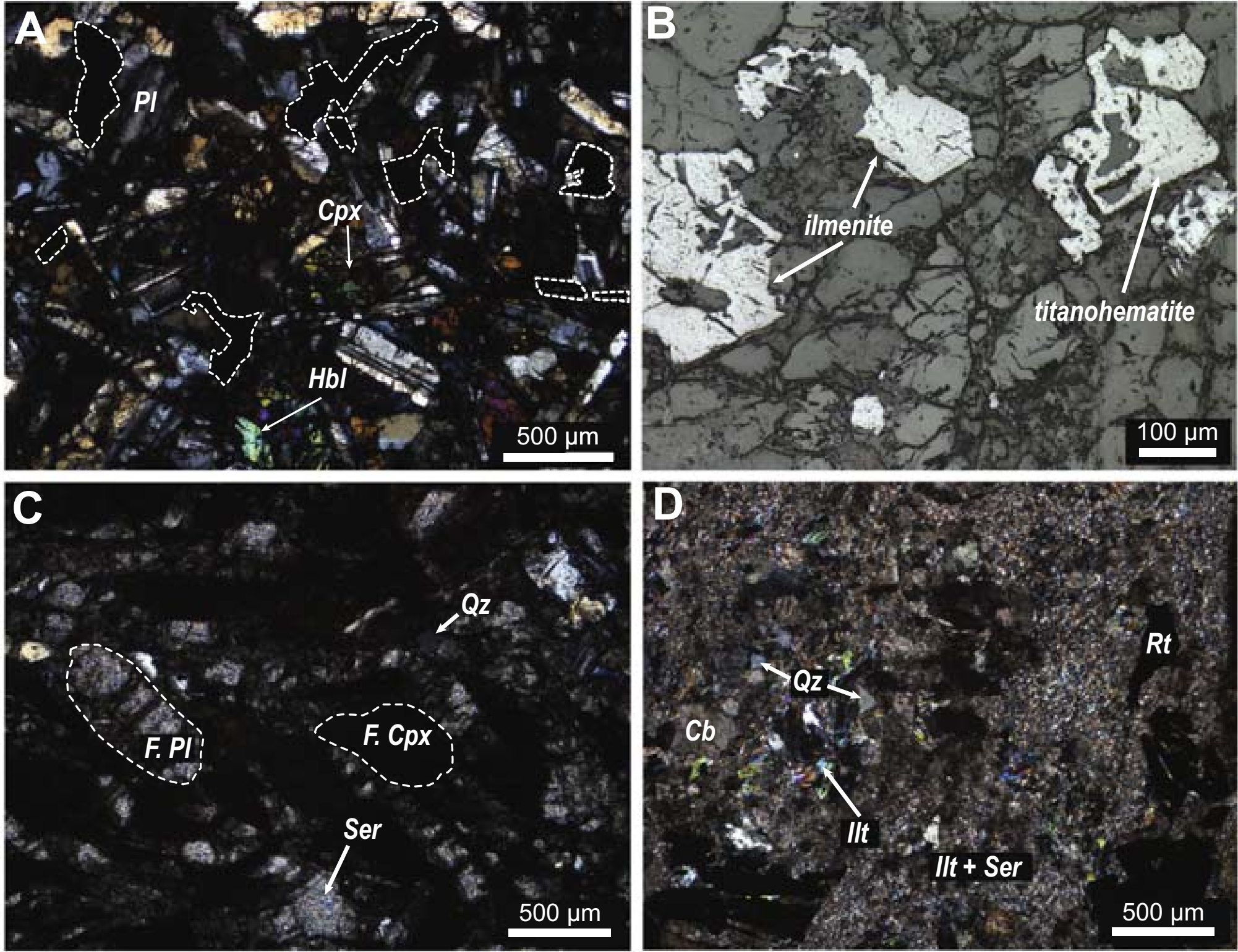
A
Pl
Cpx
Hbl
500 µm
B
ilmenite
titanohematite
100 µm
C
Qz
F. Pl
F. Cpx
Ser
500 µm
D
Rt
Qz
Cb
Ilt
Ilt + Ser
500 µm

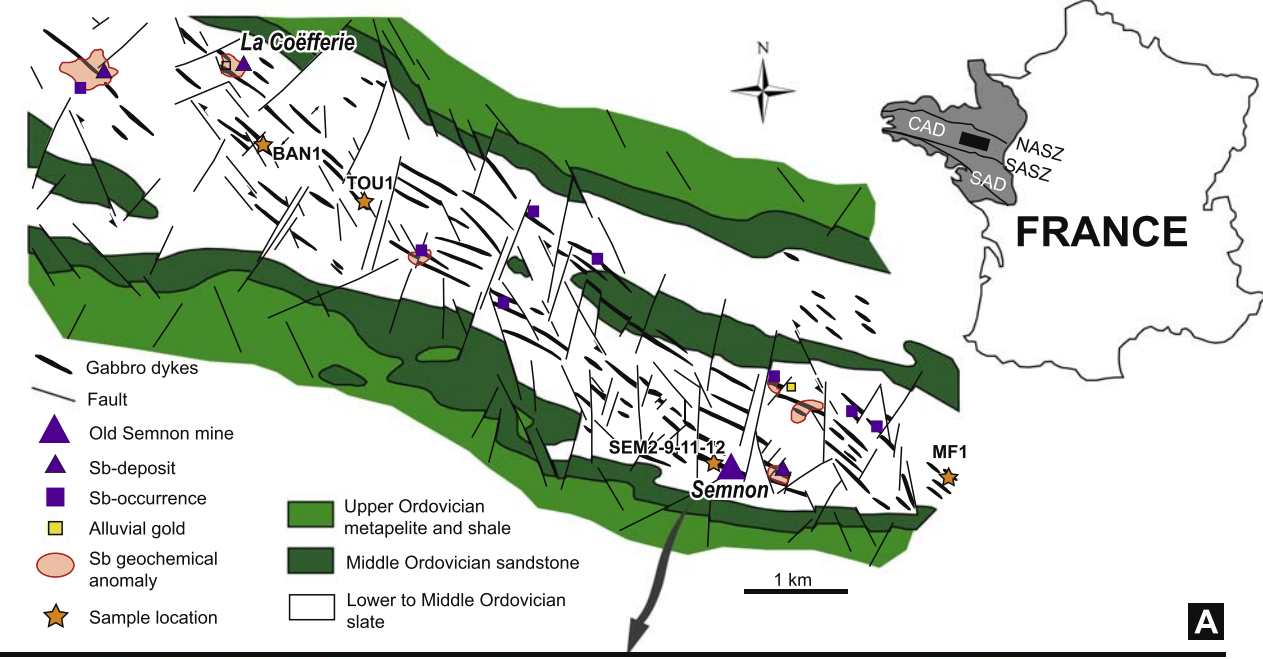
La Coëfferie
BAN1
TOU1
SEM2-9-11-12
Semnon
MF1
N
CAD
NASZ
SASZ
SAD
FRANCE
Gabbro dykes
Fault
Old Semnon mine
Sb-deposit
Sb-occurrence
Alluvial gold
Sb geochemical anomaly
Sample location
Upper Ordovician metapelite and shale
Middle Ordovician sandstone
Lower to Middle Ordovician slate
1 km
A

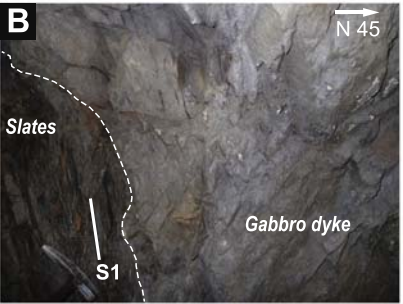
B
N 45
Slates
Gabbro dyke
S1

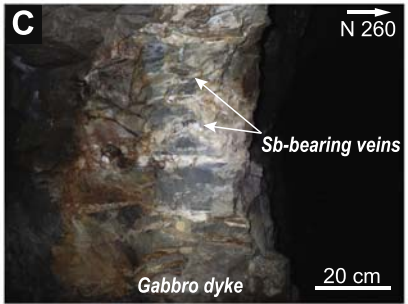
C
N 260
Sb-bearing veins
Gabbro dyke
20 cm


D
Arsenopyrite
N 250